A General Methodology for Generating Representative Load Cycles for Monohull Surface Vessels

by

William Anthony Lawrence Truelove
B.Eng. (Mechanical Engineering), Royal Military College of Canada, 2011
B.Sc. (Applied Mathematics), Athabasca University, 2016

A Thesis Submitted in Partial Fulfillment of the
Requirements for the Degree of

MASTER OF APPLIED SCIENCE

in the Department of Mechanical Engineering

A General Methodology for Generating Representative Load Cycles for Monohull Surface Vessels

by

William Anthony Lawrence Truelove
B.Eng. (Mechanical Engineering), Royal Military College of Canada, 2011
B.Sc. (Applied Mathematics), Athabasca University, 2016

Supervisory Committee

Dr. Zuomin Dong, Supervisor
Department of Mechanical Engineering

Dr. Peter Oshkai, Departmental Member
Department of Mechanical Engineering

Dr. Andrew Rowe, Departmental Member
Department of Mechanical Engineering

Abstract

In this thesis, a general methodology for generating representative load cycles for arbitrary monohull surface vessels is developed. The proposed methodology takes a hull geometry and propeller placement, vessel loading condition, vessel mission, and weather data (wind, waves, currents) and, from that, generates the propeller states (torque, speed, power) and steering gear states (torque, speed, power) necessary to accomplish the given mission. The propeller states, together with the steering gear states, thus define the load cycle corresponding to the given inputs (vessel, mission, weather). Some key aspects of the proposed methodology include the use of a surge-sway-yaw model for vessel dynamics as well as the use of surrogate geometries for both the hull and propeller(s). What results is a methodology that is lean (that is, it requires only sparse input), fast, easy to generalize, and reasonably accurate.

The proposed methodology is validated by way of two separate case studies, case A and case B (both involving distinct car-deck ferries), with case A being a more ideal case, and case B being a less ideal case given the methodology proposed. In both cases, the load cycle generation process completed in greater than real time, achieving time ratios (simulated time to execution time) of 3.3:1 and 12.8:1 for cases A and B respectively. The generated propeller and steering gear states were then compared to data collected either at sea or from the vessels' documentation. For case A, the propeller speed, torque, and power values generated were all accurate to within $\pm 3\%$, $\pm 7\%$, and $\pm 10\%$ of the true values, respectively, while cruising, and accurate to within $\pm 14\%$, $\pm 36\%$, and $\pm 42\%$ of the true values, respectively, while maneuvering. In addition, the steering gear powers generated in case A were consistent with the capabilities of the equipment actually installed on board. For case B, the propeller speed, torque, and power values generated were all accurate to within $\pm 2\%$, $\pm 8\%$, and $\pm 9\%$ of the true values, respectively, while cruising, and accurate to within $\pm 28\%$, $\pm 45\%$, and $\pm 66\%$ of the true values, respectively, while maneuvering. In case B, however, the steering gear powers generated were questionable. Considering the results of the validation, together with the rapid process runtimes achieved and sparse inputs given, one may conclude that the methodology proposed in this thesis shows promise in terms of being able to generate representative load cycles for arbitrary monohull surface vessels.

Table of Contents

List of Tables

List of Figures

Nomenclature

A_{abeam}	abeam projected area (of the wetted hull)
A_b	propeller blade face area
a_i	amplitude of i^{th} wave component
A_{ij}	ij^{th} element of $\mathbf{M}_A$ (added mass-inertia)
A_s	propeller swept area
A_{wetted}	wetted surface area
$A_{x_b}(\ )$	transverse cut area
A_{xz_w}	abeam projected area (or sail area) of vessel superstructure
A_{yz_w}	lengthwise projected area (or sail area) of vessel superstructure
$A_{z_b}(\ )$	waterplane cut area
B	vessel beam
B_{11V}	linear damping (surge-surge)
B_{22V}	linear damping (sway-sway)
B_{66V}	linear damping (yaw-yaw)
$\{b\}$	body-fixed frame
b_{steer}	steering gear angular damping
$\mathbf{C}_A(\ )$	hydrodynamic Coriolis-centripetal matrix
C_b	block coefficient
$C_d^{2D}(\ )$	2D drag coefficient
C_f	friction drag coefficient

$C_{\text{foul,hull}}$	hull fouling coefficient
C_{inertia}	inertia scalar
$C_{K_Q,\text{fouling}}(\ )$	propeller fouling scalar on K_Q
$C_{K_Q,\text{nozzle}}(\ )$	propeller nozzle scalar on K_Q
$C_{K_Q,\theta}(\ )$	inflow angle scalar on K_Q
$C_{K_T,\text{fouling}}(\ )$	propeller fouling scalar on K_T
$C_{K_T,\text{nozzle}}(\ )$	propeller nozzle scalar on K_T
$C_{K_T,\theta}(\ )$	inflow angle scalar on K_T
C_m	midship section coefficient
C_p	prismatic coefficient
$\mathbf{C}_{RB}(\ )$	rigid-body Coriolis-centripetal matrix
C_V	viscous drag coefficient
C_w	wave-making drag coefficient
C_{wp}	waterplane coefficient
C_X	wind drag coefficient (surge)
C_Y	wind drag coefficient (sway)
D	propeller diameter
$\mathbf{D}$	linear damping matrix
$\mathbf{D}_n(\ )$	non-linear damping matrix
$\mathbf{D}(\ )$	total damping matrix
$D(\ )$	wave spreading function
$\{e\}$	earth-centered, earth-fixed frame
η	vessel position / orientation state vector -OR- sea surface elevation -OR- Rayleigh damping coefficient

$\mathrm{E}[\overline{u}_S]$	expected Stokes drift over vessel draft (relative to earth)
f_i	frequency of i^{th} wave component
F_{ix}	x_b component of propeller i thrust
F_{iy}	y_b component of propeller i thrust
f_p	peak wave frequency
Fr	Froude number
$\vec{F}_{\text{thrust}}$	solution to linear thrust problem
F_{un}	total non-linear drag force (surge)
F_{unV}	non-linear drag force (surge), viscous component
F_{unW}	non-linear drag force (surge), wave-making component
F_{vn}	total non-linear drag force (sway)
g	acceleration due to gravity
H	wave height
H_s	significant wave height
$\mathbf{I}_{3\times3}$	3×3 identity matrix
$\mathbf{I}_g$	vessel inertia tensor about the centre of gravity
I_{ij}	ij^{th} element of $\mathbf{I}_g$ (inertia tensor)
$I_{\text{propshaft}}$	propeller shaft moment of inertia
I_{steer}	steering gear moment of inertia
$I_{xx}^{O_b}$	roll inertia (about O_b)
$I_{yy}^{O_b}$	pitch inertia (about O_b)
$I_{zz}^{O_b}$	yaw inertia (about O_b)
J	propeller advance ratio

J^*	critical propeller advance ratio
k	wave number
K	form factor
K_Q	propeller torque coefficient
K_T	propeller thrust coefficient
l	longitude
L	vessel length
m	vessel mass (displacement)
$\mathbf{M}_A$	added mass-inertia matrix
$\mathbf{M}_{RB}$	rigid-body mass-inertia matrix
M_{rn}	total non-linear drag moment (yaw)
μ	latitude -OR- dynamic viscosity
$N_1(\ )$	latitudinal (or vertical) radius of curvature of the earth
n_{blades}	number of blades (propeller)
$\{n\}$	north-east-down frame
ν	body-fixed velocities vector (relative to earth)
ν_r	body-fixed velocities vector (relative to water)
$\nu_{\text{thruster,fluid}}$	velocity vector (thruster relative to fluid)
N_v	linear damping (yaw-sway)
O_b	origin of $\{b\}$
O_e	origin of $\{e\}$
ω	wave angular frequency
ω_{design}	propeller design speed

ω_{prop}	propeller turning rate
ω_{steer}	steering gear turning rate
O_n	origin of $\{n\}$
p	roll rate (relative to earth)
P	propeller pitch
p_c	roll rate of water (relative to earth)
ϕ	Euler angle 1
ϕ_i	phase shift of i^{th} wave component
ψ	vessel heading -OR- Euler angle 3
q	pitch rate (relative to earth)
q_c	pitch rate of water (relative to earth)
Q_{prop}	propeller torque
Q_{steer}	steering gear torque
r	yaw rate (relative to earth)
r_c	yaw rate of water (relative to earth)
r_e	equatorial radius of the earth
Re	Reynolds number
r_g^b	vector (in $\{b\}$) from the vessel's centre of gravity to O_b
ρ	density
r_p	polar radius of the earth
rps	propeller speed [rev/s]
r_r	yaw rate (relative to water)
r_{rw}	yaw rate (relative to wind)
$\mathbf{S}(\ )$	cross-product operator (or skew operator)

σ_η^2	wave height variance
s_x	x position (in $\{b\}$) of the centroid of A_{xz_w}
s_y	y position (in $\{b\}$) of the centroid of A_{yz_w}
t	time
T	vessel draft -OR- period
τ_{control}	control forces and moments vector
τ_{nldrag}	non-linear drag forces and moments vector
τ_{wind}	wind forces and moments vector
θ	Euler angle 2 -OR- wave heading
θ_c	current heading
$\theta_{\text{flow},i}$	propeller i inflow angle
θ_p	dominant wave heading
$\theta_{\text{steer},i}$	angle (in $\{b\}$) of propeller i thrust
θ_w	wind heading
T_{mission}	mission duration
T_p	peak wave period
T_{prop}	characteristic period (propeller dynamics)
$T_{\text{prop},i}$	magnitude of propeller i thrust
T_{steer}	characteristic period (steering gear dynamics)
T_{surge}	characteristic period (surge dynamics)
T_{sway}	characteristic period (sway dynamics)
T_{yaw}	characteristic period (yaw dynamics)
u	surge velocity (relative to earth)
u_c	surge velocity of water (relative to earth)

U_c	current speed (relative to earth)
u_r	surge velocity (relative to water)
u_{rw}	surge velocity (relative to wind)
$\overline{u}_S$	Stokes drift (relative to earth)
U_w	wind speed (relative to earth)
v	sway velocity (relative to earth)
v_c	sway velocity of water (relative to earth)
V_{disp}	displaced volume
V_{flow}	fluid speed (relative to propeller)
v_r	sway velocity (relative to water)
v_{rw}	sway velocity (relative to wind)
w	heave velocity (relative to earth) -OR- wake ratio
w_c	heave velocity of water (relative to earth)
x_b	surge
x_e	basis vector 1 of $\{e\}$
x_g	x position (in $\{b\}$) of the vessel's centre of gravity
x_n	north
y_b	sway
y_e	basis vector 2 of $\{e\}$
y_g	y position (in $\{b\}$) of the vessel's centre of gravity
y_n	east
$y_+(\ )$	half-beam measure
Y_r	linear damping (sway-yaw)

z_b heave

z_g z position (in $\{b\}$) of the vessel's centre of gravity

z_n down

Acknowledgements

I would like to acknowledge the kind support of my supervisory committee: Dr. Zuomin Dong, Dr. Peter Oshkai, and Dr. Andrew Rowe. Their guiding questions, individual expertise, and encouraging feedback were key in ensuring the successful completion of this work. I would also like to extend my gratitude to Dr. Brad Buckham, whose input was most helpful in assembling the vessel dynamics theory presented in this work. I wish also to acknowledge the support of my fellow research mates: Haijia "Alex" Zhu, Michael Grant, Mostafa Rahimpour, and Duncan McIntyre. Alex and Mike were the ones who collected and processed the operational data which I then subsequently used in the validation portion of this work. Without their efforts, no such validation would have been possible. Mostafa and Duncan were the ones who generated the computational fluid dynamics results which I then subsequently used to develop the method of propeller dynamics modelling presented in this work. In addition, they provided computational hull drag results against which I was able to validate the hull drag equations as implemented in this work. Without their efforts, this thesis would be not nearly as detailed, nor as validated, as it presently is. Finally, I would like to thank Dr. Kevin McTaggart of Defence Research and Development Canada for graciously offering to act as external examiner during the defence of this thesis.

This thesis was drafted using LaTeX 2_ε

Introduction

Motivation and Intent

According to the United Nations 2017 Review of Maritime Transport [Hoffmann and Sirimanne, 2017], the vast majority of global trade (more than 80% by volume and 70% by value) is still seaborne. In addition, the most recent International Maritime Organization (IMO) marine pollution (MARPOL) regulations [IMO, 2011] have imposed more stringent restrictions on vessel emissions, thus placing further pressure on the sector to achieve more efficient means of propulsion and power generation. For example, the Tier III emissions regulations of MARPOL Annex VI came into effect on 1 January 2016. These regulations restrict, among other things, nitrogen oxide (NOx) emissions for installed diesel engines (with rated power greater than 130 kW) to between 3.4 and 2.0 g/kWh, depending on engine rated speed [IMO, 2018b]. Even more stringent restrictions apply in areas defined as an emission control area [IMO, 2018a]. This is a significant reduction from both the Tier I regulations of 1 January 2000, which limited NOx emissions to between 17.0 and 9.8 g/kWh, and the Tier II regulations of 1 January 2011, which limited NOx emissions to between 14.4 and 7.7 g/kwh. With respect to enforcement, failure to comply with Annex VI can result in denial of an engine international air pollution prevention certificate (which, in turn, can affect a vessel's eligibility for certification under organizations such as Lloyds Register, the American Bureau of Shipping, and Det Norske Veritas - Germanischer Lloyd) as well as fines [DNV-GL, 2015]. For this reason, design of efficient propulsion and power generation systems for seagoing vessels is a problem of practical concern.

Unfortunately, the magnitude of the reductions in emissions limits from Tier II to Tier III means that, in order to be compliant, engine tuning alone will no longer suffice; new technologies must be embraced. Fortunately, several options exist, such as [DNV-GL, 2015]

- dual fuel technology
- selective catalytic reduction technology
- exhaust gas recirculation technology
- hybrid electric technology
- hybrid fuel cell technology

One such option, hybrid electric, is of particular note since advances in this technology (driven largely by advances in the automotive sector; see, for instance, [Paykani and Shervani-Tabar, 2011, Alvarez et al., 2010, Sioshansi and Denholm, 2009, Fontaras et al., 2008]) have led to an increase in its adoption in the marine sector [Peters, 2017]. In addition, since hybrid electric technology in the automotive sector continues to exhibit both decreasing cost and increasing performance trends [German, 2015], it stands to reason that the same trends should emerge in the marine sector as adoption of the technology becomes more widespread. Indeed, it has already been shown in [Geertsma et al., 2017, Dedes et al., 2012] that hybridization of marine propulsion can lead to significant reductions in both fuel consumption and emissions. For this reason, an investigation of the applicability of hybrid electric technology to arbitrary seagoing vessels is immediately relevant.

Of note in the research cited above is a general structure; that is, "given a load cycle, an optimization of the plant/controls was performed", etc. Some examples of current Canadian research having this general structure are [Chen et al., 2018, Chen and Dong, 2018, Manouchehrinia et al., 2018a, Manouchehrinia et al.,

2018b]. Given this general structure, it follows that the ability to generate representative load cycles for arbitrary seagoing vessels would be valuable to researchers as well as industry. Therefore, the intent of this thesis is to develop a general methodology for generating representative load cycles for arbitrary monohull surface vessels.

Definitions

Before proceeding further, a number of terms important to this thesis should be clearly defined

1) surface vessel;
2) monohull vessel;
3) mission cycle;
4) drive cycle; and,
5) load cycle

A **surface vessel**, for the purpose of this thesis, is taken to mean a marine vessel that rides on the surface of the water by means of buoyancy (i.e., a displacement vessel). This is different from a planing vessel, which rides by way of hydrodynamic lift. More specifically, a **monohull** surface vessel is, as the name suggests, a surface vessel whose submerged geometry is a single hull (that is, the submerged geometry is simply connected). This differs from examples like a catamaran or a trimaran, as these designs have submerged geometries consisting of two and three distinct hulls respectively (that is, the submerged geometries are not simply connected). For illustration, see the following

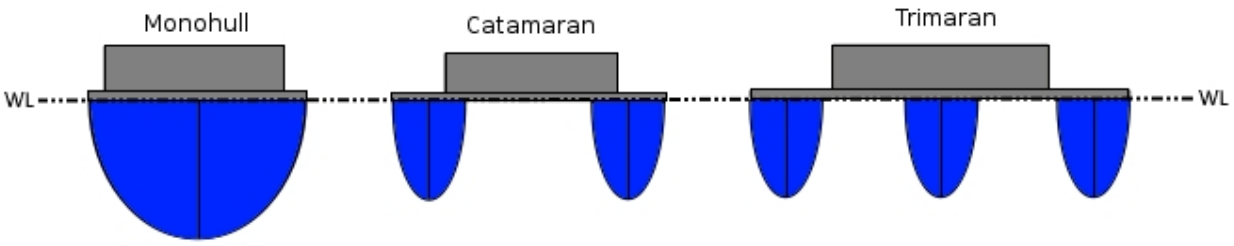

Figure 1: Transverse views of a monohull, catamaran, and trimaran design (adapted from [Aveek, 2009])

A **mission cycle** defines a vessel's mission; that is, where it needs to be and when it needs to be there. Since the position and orientation of a vessel can be fully defined by latitude, μ, longitude, l, and heading, ψ, it follows that a vessel's mission cycle can be described in two ways

1) by a set of three functions, $\mu(t)$, $l(t)$, and $\psi(t)$; or,
2) by a sequence of n waypoints and headings, $\{(t_i, \mu_i, l_i, \psi_i)\}$

where, in practice, description 2 is most common.

A **drive cycle** defines how a vessel must be driven in order to accomplish a given mission cycle. As such, the drive cycle of a vessel is a set of velocities which define how the vessel must move through space. Since the mission cycle involves latitude, longitude, and heading, it suffices for the drive cycle to include velocities in surge (sailing ahead/forward), u, sway (sailing side-to-side), v, and yaw (turning in place), r; see figure 1.1 for illustration. Therefore, a vessel's drive cycle can be described in two ways

1) by a set of three functions, $u(t)$, $v(t)$, and $r(t)$; or,
2) by a sequence of n vectors, $\left\{\begin{bmatrix} u_i & v_i & r_i \end{bmatrix}^{\mathrm{T}}\right\}$, corresponding to discrete times t_i

A **load cycle** defines the rate at which a vessel must do work in order to achieve a given drive cycle. This rate of work, or power, can be broken down into two main components

1) propulsion; and,
2) steering

Propulsion power can be described any number of ways, for example at the main engine(s) or after a particular gearbox or at the propeller(s). This thesis, however, will focus specifically on the later; that is, describing propulsion power by way of torque, Q_{prop}, and turning rate, ω_{prop}, at the propeller(s). Steering power is described in a similar fashion; by way of torque, Q_{steer}, and turning rate, ω_{steer} , at the steering gear. Thus, a vessel's load cycle can be described in two ways

1) by a set of two functions, $Q_{\text{prop}}(t)$, $\omega_{\text{prop}}(t)$, for each propeller, and a set of two functions, $Q_{\text{steer}}(t)$, and $\omega_{\text{steer}}(t)$, for each steering gear; or,
2) by a collection of sequences of n states, $\{(t_i, Q_{\text{prop},i}, \omega_{\text{prop},i})\}$, with one sequence per propeller, and a collection of sequences of n states, $\{(t_i, Q_{\text{steer},i}, \omega_{\text{steer},i})\}$, with one sequence per steering gear

General Methodology

Given the definitions of mission cycle, drive cycle, and load cycle presented above, the following general methodology for mapping from mission cycle to load cycle is here proposed

1) kinematics; that is, generating an appropriate drive cycle from a given mission cycle; then,
2) kinetics; that is, generating appropriate control forces and moments so as to achieve the given drive cycle; then,
3) propeller dynamics; that is, generating appropriate propeller states so as to produce the required control forces and moments; then,
4) steering dynamics; that is, generating appropriate steering gear states from the propeller states

This process can be illustrated, in flowchart form, as per figure 2. In the chapters that follow, the foundational theory upon which this general methodology is constructed will be presented, the specifics of implementation will be handled, and then a few case studies, including results, will be summarized.

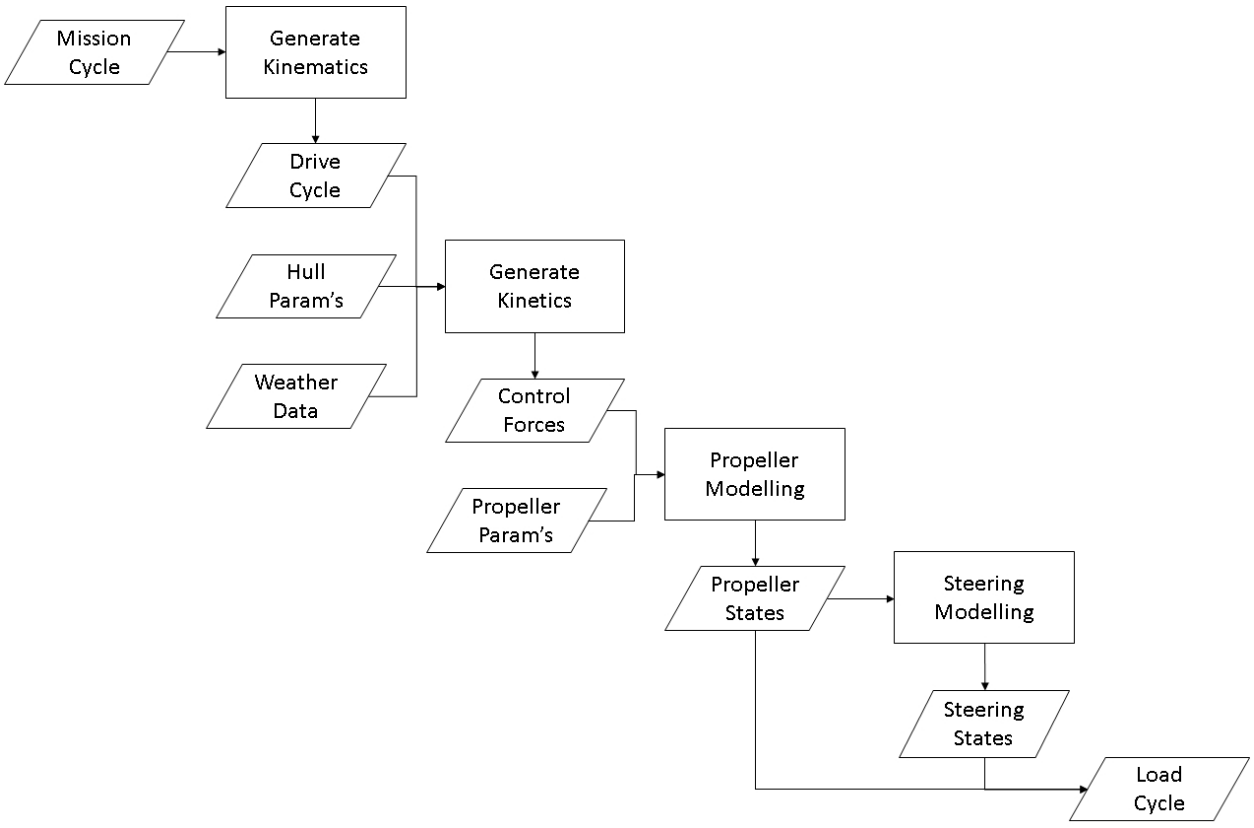

Figure 2: General methodology - process flowchart

Chapter 1

Foundational Theory

In this chapter, the foundational theory, upon which the process illustrated in figure 2 will be constructed, is presented. First, the theory of mapping from a mission cycle to an equivalent drive cycle is given, including definitions of a number of requisite frames of reference. The equations governing vessel dynamics are then stated in six degrees of freedom, as per [Fossen, 2011], before subsequently being reduced to the case of surge-sway-yaw, which is the case assumed in this thesis. Then, surrogate geometries for a vessel's hull and propeller(s) are introduced and a number of relevant general results are derived. Finally, a theory for extracting wave drift from a given sea state is developed.

1.1 Mapping from Mission Cycle to Drive Cycle

In order to generate a load cycle from a given mission cycle, one must first translate the mission cycle into an appropriate drive cycle. This section will detail how one can do this in general.

1.1.1 Frames of Reference

In order to express the dynamics of a seagoing vessel in a sufficiently detailed manner, it is necessary to make use of a number of different frames of reference. In this subsection, the body-fixed frame, $\{b\}$, north-east-down frame, $\{n\}$, and earth-centered, earth-fixed frame, $\{e\}$, will all be defined.

Body-Fixed Frame

The body-fixed frame is, as its name suggests, a Cartesian frame that is affixed to the vessel. This frame may be illustrated as follows

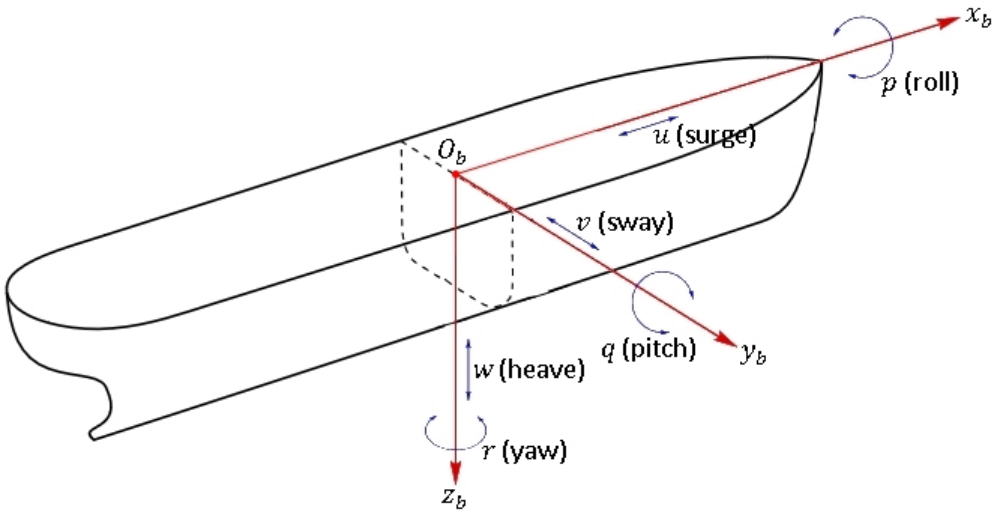

Figure 1.1: Body-fixed frame (adapted from [Brosen, 2006])

where O_b is the frame origin, conventionally placed miships on the waterplane, x_b is oriented positive forward, y_b is oriented positive starboard, and z_b is generated by $x_b \times y_b$. These axes are commonly referred to as "surge", "sway", and "heave" respectively. Rotations about these axes are commonly referred to as "roll", "pitch", and "yaw" respectively. Finally, the velocities along/about these axes are denoted by u, v, w, p, q, and r respectively (see figure 1.1).

North-East-Down Frame

The north-east-down frame (NED) is an earth-fixed Cartesian frame set in the plane tangent to the earth at the position of the vessel (see figure 1.2 for illustration). Its component axes are defined such that x_n is oriented due north, y_n is oriented due east, and z_n is generated by $x_n \times y_n$. Finally, the origin of $\{n\}$, O_n, is defined such that it is coincident with O_b.

Earth-Centered, Earth-Fixed Frame

The earth-centered, earth-fixed frame (ECEF) is, as its name suggests, an earth-fixed Cartesian frame with origin, O_e, at the centre of the earth. Its component axes are defined such that z_e is the vector from O_e to the north pole, x_e is the vector from O_e to the intersection of the equator and the prime meridian[1], and y_e is generated by $z_e \times x_e$. The following illustrates both the ECEF and NED frames

[1]The prime meridian is the meridian of longitude which passes through the British Royal Observatory in Greenwich, England

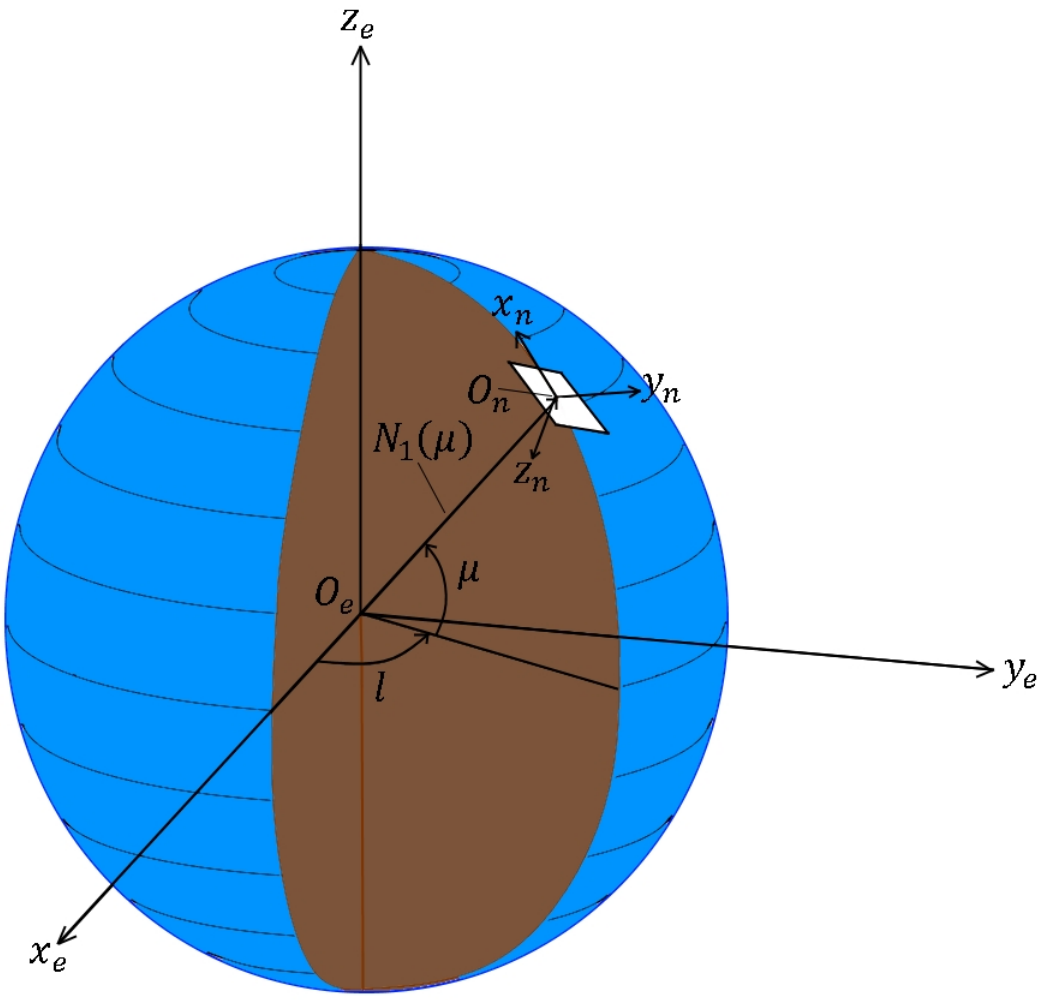

Figure 1.2: ECEF and NED frames (adapted from [Fossen, 2011])

Figure 1.2 also illustrates two other important concepts, namely

1) any arbitrary position on the surface of the earth can be defined using two angles: latitude, μ, and longitude, l; and,

2) the earth is not perfectly spherical, but rather is more of an ellipsoid (as evidenced in figure 1.2 by the fact that span(z_n) need not contain O_e). $N_1(\ )$ in figure 1.2 denotes the latitudinal (or vertical) radius of curvature of the earth at latitude μ, and is defined as follows

$$N_1(\mu) = \frac{r_e^2}{\sqrt{r_e^2 \cos^2(\mu) + r_p^2 \sin^2(\mu)}} \tag{1.1}$$

where the equatorial and polar radii of the earth are given by

$$r_e = 6378137 \text{ m}$$

$$r_p = 6356752 \text{ m}$$

1.1.2 Mission to Drive Formula

Suppose one has values for $\frac{d\mu}{dt}$ and $\frac{dl}{dt}$. From this, it follows that[2]

$$\frac{dx_n}{dt} = N_1(\mu)\frac{d\mu}{dt} \tag{1.2a}$$

$$\frac{dy_n}{dt} = N_1(\mu)\cos(\mu)\frac{dl}{dt} \tag{1.2b}$$

In addition, suppose one has values for ψ and $\frac{d\psi}{dt}$ as well, where ψ is the angle from x_n to x_b in the plane $\text{span}(x_n, y_n)$ (i.e., the vessel's heading). From this, obtaining values for u, v, and r is a matter of rotating from $\{n\}$ to $\{b\}$ as follows [Fossen, 2011]

$$\begin{bmatrix} u \\ v \\ r \end{bmatrix} = \begin{bmatrix} \cos(\psi) & \sin(\psi) & 0 \\ -\sin(\psi) & \cos(\psi) & 0 \\ 0 & 0 & 1 \end{bmatrix} \begin{bmatrix} \frac{dx_n}{dt} \\ \frac{dy_n}{dt} \\ \frac{d\psi}{dt} \end{bmatrix} \tag{1.3}$$

1.2 Vessel Dynamics Equations - Definitions

One of the central objects of this thesis is a means of translating a given drive cycle into the corresponding forces and moments required to propel the vessel as prescribed. For this purpose, the vessel dynamics equations of [Fossen, 2011] are here introduced. These equations can be stated, in vector form, as follows

$$\underbrace{\mathbf{M}_{RB}\dot{\nu} + \mathbf{C}_{RB}(\nu)\nu}_{\text{rigid-body dynamics}} + \underbrace{\mathbf{M}_A\dot{\nu}_r + \mathbf{C}_A(\nu_r)\nu_r + \mathbf{D}(\nu_r)\nu_r}_{\text{hydrodynamics}} + \underbrace{g(\eta) + g_0}_{\text{hydrostatics}} = \underbrace{\tau_{\text{control}} + \tau_{\text{wind}} + \tau_{\text{waves}}}_{\text{external forces}} \tag{1.4}$$

where the state vectors η, ν, and ν_r express

$$\eta = \begin{bmatrix} x_e & y_e & z_e & \phi & \theta & \psi \end{bmatrix}^T \tag{1.5a}$$

$$\nu = \begin{bmatrix} u & v & w & p & q & r \end{bmatrix}^T \tag{1.5b}$$

$$\nu_r = \begin{bmatrix} u - u_c & v - v_c & w - w_c & p - p_c & q - q_c & r - r_c \end{bmatrix}^T \tag{1.5c}$$

The various equation terms will be clearly defined in the following subsections.

1.2.1 State Vectors

The three state vectors, η, ν, and ν_r describe, respectively, the global position and orientation of the vessel, the body-fixed velocities and angular velocities of the vessel, and the body-fixed velocities and angular velocities of the vessel relative to the water. Their sub-vectors are as follows

1) $\begin{bmatrix} x_e & y_e & z_e \end{bmatrix}^T$ is a vector describing the position of O_b in $\{e\}$;

2) $\begin{bmatrix} \phi & \theta & \psi \end{bmatrix}^T$ is a vector describing the Euler angle sequence to rotate from $\{n\}$ to $\{b\}$;

3) $\begin{bmatrix} u & v & w \end{bmatrix}^T$ is a vector of body-fixed velocities in surge, sway, and heave (see figure 1.1 for illustration);

4) $\begin{bmatrix} p & q & r \end{bmatrix}^T$ is a vector of body-fixed angular velocities about surge, sway, and heave (i.e., roll, pitch, and yaw, see figure 1.1 for illustration);

5) $\begin{bmatrix} u - u_c & v - v_c & w - w_c \end{bmatrix}^T$ is a vector, in $\{b\}$, of the velocities in surge, sway, and heave of the vessel relative to the water, with the $(\ )_c$ being the respective velocities of the water; and,

6) $\begin{bmatrix} p - p_c & q - q_c & r - r_c \end{bmatrix}^T$ is a vector, in $\{b\}$, of the angular velocities in pitch, roll, and yaw of the vessel relative to the water, with the $(\ )_c$ being the respective angular velocities of the water.

[2] Of course, inputs here must be given here in terms of rad and rad/s, not deg and deg/s.

1.2.2 Mass-Inertia Matrices

Rigid-Body Mass-Inertia Matrix

The rigid-body mass-inertia matrix, $\mathbf{M}_{RB}$, is defined as follows

$$\mathbf{M}_{RB} = \begin{bmatrix} m\mathbf{I}_{3\times 3} & -m\mathbf{S}(r_g^b) \\ m\mathbf{S}(r_g^b) & \mathbf{I}_g - m\mathbf{S}^2(r_g^b) \end{bmatrix} \tag{1.6}$$

where m is the mass (or displacement) of the vessel, r_g^b is the vector, in $\{b\}$, from the vessel centre of gravity (CG) to O_b, $\mathbf{I}_{3\times 3}$ is the 3×3 identity matrix, $\mathbf{I}_g$ is the vessel inertia tensor about CG given by

$$\mathbf{I}_g = \begin{bmatrix} I_{xx} & -I_{xy} & -I_{xz} \\ -I_{yx} & I_{yy} & -I_{yz} \\ -I_{zx} & -I_{zy} & I_{zz} \end{bmatrix} \tag{1.7}$$

and $\mathbf{S}(\ )$ is the cross-product operator (or skew operator) defined as follows

$$\mathbf{S}(a) = \begin{bmatrix} 0 & -a_3 & a_2 \\ a_3 & 0 & -a_1 \\ -a_2 & a_1 & 0 \end{bmatrix} \tag{1.8}$$

Note that

$$\mathbf{S}(a)b = \begin{bmatrix} 0 & -a_3 & a_2 \\ a_3 & 0 & -a_1 \\ -a_2 & a_1 & 0 \end{bmatrix} \begin{bmatrix} b_1 \\ b_2 \\ b_3 \end{bmatrix} = \begin{bmatrix} a_2b_3 - a_3b_2 \\ a_3b_1 - a_1b_3 \\ a_1b_2 - a_2b_1 \end{bmatrix} = a \times b$$

and $\mathbf{S}^n(\ ) = \underbrace{\mathbf{S}(\ )\mathbf{S}(\ )\ldots\mathbf{S}(\ )}_{n \text{ times}}$.

Added Mass-Inertia Matrix

The added mass-inertia matrix, $\mathbf{M}_A$, is a matrix of the form

$$\mathbf{M}_A = \begin{bmatrix} A_{11} & A_{12} & \ldots & A_{16} \\ A_{21} & A_{22} & \ldots & A_{26} \\ \vdots & \vdots & \ddots & \vdots \\ A_{61} & A_{62} & \ldots & A_{66} \end{bmatrix} \tag{1.9}$$

The computation of these terms will be detailed in the section concerning the surrogate hull geometry.

1.2.3 Coriolis-Centripetal Matrices

Rigid-Body Coriolis-Centripetal Matrix

The rigid-body Coriolis-centripetal matrix, $\mathbf{C}_{RB}(\nu)$, can be expressed as follows (Theorem 3.2 of [Fossen, 2011])

$$\mathbf{C}_{RB}(\nu) = \begin{bmatrix} \mathbf{0}_{3\times 3} & -\mathbf{S}(m\mathbf{I}_{3\times 3}\nu_1 - m\mathbf{S}(r_g^b)\omega) \\ -\mathbf{S}(m\mathbf{I}_{3\times 3}\nu_1 - m\mathbf{S}(r_g^b)\omega) & -\mathbf{S}(m\mathbf{S}(r_g^b)\nu_1 + \mathbf{I}_g - m\mathbf{S}^2(r_g^b)\omega) \end{bmatrix} \tag{1.10}$$

where $\nu_1 = \begin{bmatrix} u & v & w \end{bmatrix}^T$ and $\omega = \begin{bmatrix} p & q & r \end{bmatrix}^T$.

Hydrodynamic Coriolis-Centripetal Matrix

As per Theorem 3.2 of [Fossen, 2011], the hydrodynamic Coriolis-centripetal matrix, $\mathbf{C}_A(\nu_r)$, can be expressed as follows

IF

$$\mathbf{M}_A = \begin{bmatrix} \mathbf{A}_{\text{ul}} & \mathbf{A}_{\text{ur}} \\ \mathbf{A}_{\text{ll}} & \mathbf{A}_{\text{lr}} \end{bmatrix}$$

THEN

$$\mathbf{C}_A(\nu_r) = \begin{bmatrix} \mathbf{0}_{3\times 3} & -\mathbf{S}(\mathbf{A}_{\text{ul}}\nu_{r1} + \mathbf{A}_{\text{ur}}\nu_{r2}) \\ -\mathbf{S}(\mathbf{A}_{\text{ul}}\nu_{r1} + \mathbf{A}_{\text{ur}}\nu_{r2}) & -\mathbf{S}(\mathbf{A}_{\text{ll}}\nu_{r1} + \mathbf{A}_{\text{lr}}\nu_{r2}) \end{bmatrix} \tag{1.11}$$

where $\nu_{r1} = \begin{bmatrix} u - u_c & v - v_c & w - w_c \end{bmatrix}^T$ and $\nu_{r2} = \begin{bmatrix} p - p_c & q - q_c & r - r_c \end{bmatrix}^T$.

1.2.4 Damping Matrix

The damping matrix, $\mathbf{D}(\nu_r)$, is constructed from the superposition of two component matrices: a linear damping matrix, $\mathbf{D}$, and a non-linear damping matrix, $\mathbf{D}_n(\nu_r)$. That is

$$\mathbf{D}(\nu_r) = \mathbf{D} + \mathbf{D}_n(\nu_r) \tag{1.12}$$

Linear Damping Matrix

The linear damping matrix is a matrix of the form

$$\mathbf{D} = \begin{bmatrix} B_{11V} & 0 & 0 & 0 & 0 & 0 \\ 0 & B_{22V} & 0 & -Y_p & 0 & -Y_r \\ 0 & 0 & B_{33V} + B_{33} & 0 & -Z_q & 0 \\ 0 & -K_v & 0 & B_{44V} + B_{44} & 0 & -K_r \\ 0 & 0 & -M_w & 0 & B_{55V} + B_{55} & 0 \\ 0 & -N_v & 0 & -N_p & 0 & B_{66V} \end{bmatrix} \tag{1.13}$$

where the diagonal terms are defined by equations 6.76 - 6.81 of [Fossen, 2011]. The off-diagonal terms are cross-flow terms (for example, Y_p is the linear damping coefficient in sway due to relative velocity component $p - p_c$) and they are not explicitly defined in [Fossen, 2011]. They will need to be either ignored, approximated, or determined experimentally. More details on how the undefined terms will be handled in this thesis will be presented later.

Non-Linear Damping Matrix

The non-linear damping matrix is a 6×6 matrix whose non-zero terms are as follows

$$\mathbf{D}_{n11}(\nu_r) = X_{|u|u}|u - u_c| \tag{1.14a}$$

$$\mathbf{D}_{n22}(\nu_r) = Y_{|v|v}|v - v_c| + Y_{|r|v}|r - r_c| \tag{1.14b}$$

$$\mathbf{D}_{n26}(\nu_r) = Y_{|v|r}|v - v_c| + Y_{|r|r}|r - r_c| \tag{1.14c}$$

$$\mathbf{D}_{n33}(\nu_r) = Z_{|w|w}|w - w_c| \tag{1.14d}$$

$$\mathbf{D}_{n44}(\nu_r) = K_{|p|p}|p - p_c| \tag{1.14e}$$

$$\mathbf{D}_{n55}(\nu_r) = M_{|q|q}|q - q_c| \tag{1.14f}$$

$$\mathbf{D}_{n62}(\nu_r) = N_{|v|v}|v - v_c| + N_{|r|v}|r - r_c| \tag{1.14g}$$

$$\mathbf{D}_{n66}(\nu_r) = N_{|v|r}|v - v_c| + N_{|r|r}|r - r_c| \tag{1.14h}$$

where each of the X, Y, Z, K, M, N terms are non-linear damping coefficients (for example, $X_{|u|u}$ is the coefficient in surge due to relative velocity component $u - u_c$). [Fossen, 2011] gives an explicit form for $X_{|u|u}$ as follows

$$X_{|u|u} = \frac{1}{2}\rho A_x C_x \tag{1.15}$$

where ρ is fluid density, A_x is the area of the submerged hull cross-section normal to x_b, and C_x is the current coefficient in surge. The current coefficient is related to wetted hull area, S, cross-section area, and friction coefficient, C_f, in the following way

$$C_x = \frac{S}{A_x} C_f \tag{1.16}$$

Similarly, $Y_{|v|v}$ and $Z_{|w|w}$ are given by

$$Y_{|v|v} = \frac{1}{2}\rho A_y C_y \tag{1.17a}$$

$$Z_{|w|w} = \frac{1}{2}\rho A_z C_z \tag{1.17b}$$

The remaining terms are not explicitly defined in [Fossen, 2011], and thus will need to be either ignored, approximated, or determined experimentally. More details on how the undefined terms will be handled in this thesis will be presented later.

1.2.5 Weight-Buoyancy and Trim Vectors

Weight-Buoyancy Vector

The weight-buoyancy vector, as its name suggest, captures the forces in $\{b\}$ due to weight and buoyancy. It is given as follows

$$g(\eta) = \begin{bmatrix} (W-B)\sin(\theta) \\ -(W-B)\cos(\theta)\sin(\phi) \\ -(W-B)\cos(\theta)\cos(\phi) \\ -(y_g W - y_{cb} B)\sin(\theta) + (x_g W - x_{cb} B)\cos(\theta)\cos(\phi) \\ (z_g W - z_{cb} B)\sin(\theta) + (x_g W - x_{cb} B)\cos(\theta)\cos(\phi) \\ -(x_g W - x_{cb} B)\cos(\theta)\sin(\phi) - (y_g W - y_{cb} B)\sin(\theta) \end{bmatrix} \tag{1.18}$$

where W is force of weight, B is force of buoyancy, and $\begin{bmatrix} x_{cb} & y_{cb} & z_{cb} \end{bmatrix}^T$ is the vector from CB to O_b in $\{b\}$, with CB being the vessel's centre of buoyancy.

Trim Vector

The trim vector captures forces in $\{b\}$ due to ballast systems and fluid tanks. It is given as follows

$$g_0 = g \begin{bmatrix} 0 \\ 0 \\ -\sum_i \rho_i V_i \\ -\sum_i \rho_i y_i V_i \\ \sum_i \rho_i x_i V_i \\ 0 \end{bmatrix} \tag{1.19}$$

where g is acceleration due to gravity, ρ_i is the density of the fluid in tank i, V_i is the volume of fluid in tank i, and $\begin{bmatrix} x_i & y_i & z_i \end{bmatrix}^T$ is the vector from the centroid of the fluid in tank i to O_b in $\{b\}$.

1.2.6 External Force-Moment Vectors

The vectors τ_{control}, τ_{wind}, and τ_{waves} capture, respectively, the external forces and moments upon the vessel due to thrusters, wind, and waves. Each of these vectors is expressed as follows

$$\tau_{(\ )} = \begin{bmatrix} F_u \\ F_v \\ F_w \\ M_p \\ M_q \\ M_r \end{bmatrix} \tag{1.20}$$

where the F's are forces and the M's are moments (for example, F_u is force in surge and M_r is moment in yaw).

1.3 Vessel Dynamics Equations - Simplification

This thesis will not make use of the full six degrees of freedom of equation 1.4, but will instead reduce to a three degrees of freedom, surge-sway-yaw model by invoking the following

$$w \approx 0 \quad p \approx 0 \quad q \approx 0 \quad \phi \approx 0 \quad \theta \approx 0$$

That is, assume there is negligible motion in heave, roll, and pitch, and, as such, the Euler angles ϕ and θ are negligibly small. This choice is made because, as per [Fossen, 2011], a surge-sway-yaw model is generally used for dynamic-positioning, trajectory-tracking, and path-following applications. For the purpose of this thesis, it is therefore judged that a surge-sway-yaw model strikes a good compromise between tractability and accuracy. In addition, the current at any point on the surface of the earth is herein assumed to be irrotational. As a result, the state vector ν_r is immediately reduced to

$$\nu_r = \begin{bmatrix} u - u_c & v - v_c & w - w_c & p & q & r \end{bmatrix}^T$$

The effects of these simplifying assumptions will be presented in the following subsections.

1.3.1 State Vectors

Since the dynamics of only surge, sway, and yaw are available under a surge-sway-yaw model, the state vectors immediately collapse to the following

$$\eta^* = \begin{bmatrix} \mu & l & \psi \end{bmatrix}^T \tag{1.21a}$$

$$\nu^* = \begin{bmatrix} u & v & r \end{bmatrix}^T \tag{1.21b}$$

$$\nu_r^* = \begin{bmatrix} u - u_c & v - v_c & r \end{bmatrix}^T \tag{1.21c}$$

with the reduced form of η^* being defined as per [Fossen, 2011]. A consequence of these reductions in the state vectors is that all other matrices and vectors that comprise equation 1.4 must also collapse in order to remain dimensionally commensurate. That is, all 6×6 matrices are reduced to 3×3 by keeping only those elements that are in the intersections of rows 1, 2, and 6 and columns 1, 2, and 6 (i.e., in the surge, sway, and yaw rows/columns). In addition, only the 1st, 2nd, and 6th elements of $g(\eta)$, g_0, and the τ's are retained. Finally, note that under a surge-sway-yaw model, the Euler angle ψ and the vessel's heading (that is, the angle from x_n to x_b in the plane $\text{span}(x_n, y_n)$) are necessarily the same thing.

1.3.2 Mass-Inertia Matrices

Rigid-Body Mass-Inertia Matrix

Expanding the expression for $\mathbf{M}_{RB}$ given in equation 1.6, collapsing to 3×3 in the manner described above, and then discarding zero terms yields the following

$$\mathbf{M}^*_{RB} = \begin{bmatrix} m & 0 & -my_g \\ 0 & m & mx_g \\ -my_g & mx_g & I_{zz} + m(x_g^2 + y_g^2) \end{bmatrix} \tag{1.22}$$

This can be expressed equivalently by

$$\mathbf{M}^*_{RB} = \begin{bmatrix} m & 0 & -my_g \\ 0 & m & mx_g \\ -my_g & mx_g & I_{zz}^{O_b} \end{bmatrix} \tag{1.23}$$

where $I_{zz}^{O_b}$ is mass moment of inertia in yaw about O_b.

Added Mass-Inertia Matrix

The matrix $\mathbf{M}_A$ reduces immediately to the following

$$\mathbf{M}^*_A = \begin{bmatrix} A_{11} & A_{12} & A_{16} \\ A_{21} & A_{22} & A_{26} \\ A_{61} & A_{62} & A_{66} \end{bmatrix} \tag{1.24}$$

1.3.3 Coriolis-Centripetal Matrices

Rigid-Body Coriolis-Centripetal Matrix

Expanding the expression for $\mathbf{C}_{RB}$ given in equation 1.10, collapsing to 3×3 in the manner described above, and then discarding zero terms yields the following

$$\mathbf{C}^*_{RB}(\nu^*) = \begin{bmatrix} 0 & 0 & -mv - mx_g r \\ 0 & 0 & mu - my_g r \\ mv + mx_g r & -mu + my_g r & 0 \end{bmatrix} \tag{1.25}$$

Hydrodynamic Coriolis-Centripetal Matrix

Expanding the expression for $\mathbf{C}_A$ given in equation 1.11, collapsing to 3×3 in the manner described above, and then discarding zero terms yields the following

$$\mathbf{C}^*_A(\nu^*_r) = \begin{bmatrix} 0 & 0 & -A_{21}u_r - A_{22}v_r - A_{26}r \\ 0 & 0 & A_{11}u_r + A_{12}v_r + A_{16}r \\ A_{21}u_r + A_{22}v_r + A_{26}r & -A_{11}u_r - A_{12}v_r - A_{16}r & 0 \end{bmatrix} \tag{1.26}$$

where $u_r = u - u_c$ and $v_r = v - v_c$.

1.3.4 Damping Matrix

Linear Damping Matrix

The linear damping matrix reduces immediately to the following

$$\mathbf{D}^* = \begin{bmatrix} B_{11V} & 0 & 0 \\ 0 & B_{22V} & -Y_r \\ 0 & -N_v & B_{66V} \end{bmatrix} \tag{1.27}$$

Non-Linear Damping Matrix

The non-linear damping matrix reduces immediately to the following

$$\mathbf{D}_n^*(\nu_r^*) = \begin{bmatrix} -X_{|u|u}|u_r| & 0 & 0 \\ 0 & -Y_{|v|v}|v_r| - Y_{|r|v}|r| & -Y_{|v|r}|v_r| - Y_{|r|r}|r| \\ 0 & -N_{|v|v}|v_r| - N_{|r|v}|r| & -N_{|v|r}|v_r| - N_{|r|r}|r| \end{bmatrix} \tag{1.28}$$

1.3.5 Weight-Buoyancy and Trim Vectors

Weight-Buoyancy Vector

The weight-buoyancy vector collapses under surge-sway-yaw to

$$g^*(\eta^*) = \begin{bmatrix} (W-B)\sin(\theta) \\ -(W-B)\cos(\theta)\sin(\phi) \\ -(x_g W - x_{cb}B)\cos(\theta)\sin(\phi) - (y_g W - y_{cb}B)\sin(\theta) \end{bmatrix}$$

However, since $\phi \approx 0$ and $\theta \approx 0$, it follows that $\sin(\phi) \approx 0$ and $\sin(\theta) \approx 0$ and therefore

$$g^*(\eta^*) \approx \begin{bmatrix} 0 \\ 0 \\ 0 \end{bmatrix} \tag{1.29}$$

Thus, $g^*(\eta^*)$ need not appear in the reduced equations for surge-sway-yaw.

Trim Vector

The trim vector collapses under surge-sway-yaw to

$$g_0^* = g \begin{bmatrix} 0 \\ 0 \\ 0 \end{bmatrix} \tag{1.30}$$

Thus, g_0^* need not appear in the reduced equations for surge-sway-yaw.

1.3.6 External Force-Moment Vectors

The vectors τ_{control}, τ_{wind}, and τ_{waves} collapse under surge-sway-yaw to

$$\tau_{(\ )}^* = \begin{bmatrix} F_u \\ F_v \\ M_r \end{bmatrix} \tag{1.31}$$

1.3.7 Reduced Governing Equations

As per the simplifications detailed above, equation 1.4 reduces, under surge-sway-yaw, to the following

$$\underbrace{\mathbf{M}_{RB}^*\dot{\nu^*} + \mathbf{C}_{RB}^*(\nu^*)\nu^*}_{\text{rigid-body dynamics}} + \underbrace{\mathbf{M}_A^*\dot{\nu^*}_r + \mathbf{C}_A^*(\nu_r^*)\nu_r^* + \mathbf{D}^*(\nu_r^*)\nu_r^*}_{\text{hydrodynamics}} = \underbrace{\tau_{\text{control}}^* + \tau_{\text{wind}}^* + \tau_{\text{waves}}^*}_{\text{external forces}}$$

However, for the sake of brevity, these equations will simply be stated as

$$\underbrace{\mathbf{M}_{RB}\dot{\nu} + \mathbf{C}_{RB}(\nu)\nu}_{\text{rigid-body dynamics}} + \underbrace{\mathbf{M}_A\dot{\nu_r} + \mathbf{C}_A(\nu_r)\nu_r + \mathbf{D}(\nu_r)\nu_r}_{\text{hydrodynamics}} = \underbrace{\tau_{\text{control}} + \tau_{\text{wind}} + \tau_{\text{waves}}}_{\text{external forces}} \tag{1.32}$$

with all subsequent references being references to the reduced matrices/vectors.

1.4 Surrogate Geometry I - Wigley N43 Hull

In order to fully determine the environmental forces and moments upon a seagoing vessel, it is necessary to define the geometry of the submerged hull. This, however, will vary from case to case depending on the particular design of the vessel under consideration. Since this thesis seeks general results, a compromise between accuracy, generality, and simplicity will therefore have to be struck. To that end, this thesis will assume a Wigley N43 hull geometry, defined, in $\{b\}$, by the relatively simple equations [Sun et al., 2012]

$$y_+(x,z) = \frac{B}{2}\left(1-\left(\frac{2x}{L}\right)^2\right)\left(1-\left(\frac{z}{T}\right)^2\right)\left(1+\frac{1}{5}\left(\frac{2x}{L}\right)^2\right)+\cdots$$
$$\frac{B}{2}\left(\frac{z}{T}\right)^2\left(1-\left(\frac{z}{T}\right)^8\right)\left(1-\left(\frac{2x}{L}\right)^2\right)^4 \quad \text{for} \quad \begin{cases} x \in \left[-\frac{L}{2}, \frac{L}{2}\right] \\ z \in [0,T] \end{cases} \tag{1.33a}$$

$$y_-(x,z) = -y_+(x,z) \quad \text{for} \quad \begin{cases} x \in \left[-\frac{L}{2}, \frac{L}{2}\right] \\ z \in [0,T] \end{cases} \tag{1.33b}$$

where B is beam at the waterline, L is length at the waterline, T is draft, and $y_+(x,z)$ is the half-beam measure at point (x,z). For example, for the case of a vessel having $T < \frac{B}{2} < \frac{L}{2}$, the N43 hull geometry can be illustrated as per figures 1.3 - 1.6. Assuming this geometry then allows one to establish a number of useful geometric properties, as detailed in the following subsections.

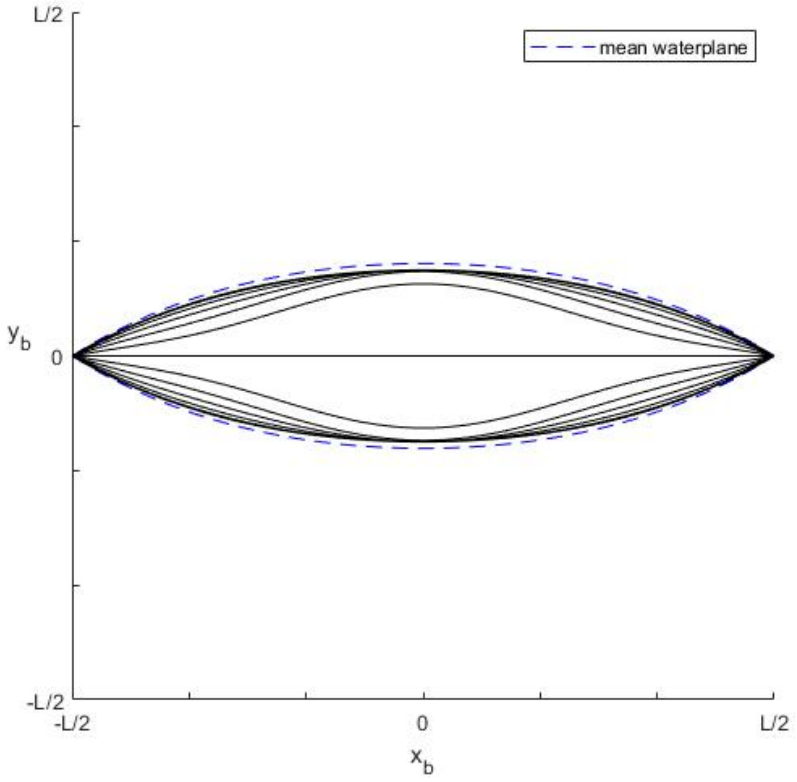

Figure 1.3: Wigley N43 hull waterplane cuts

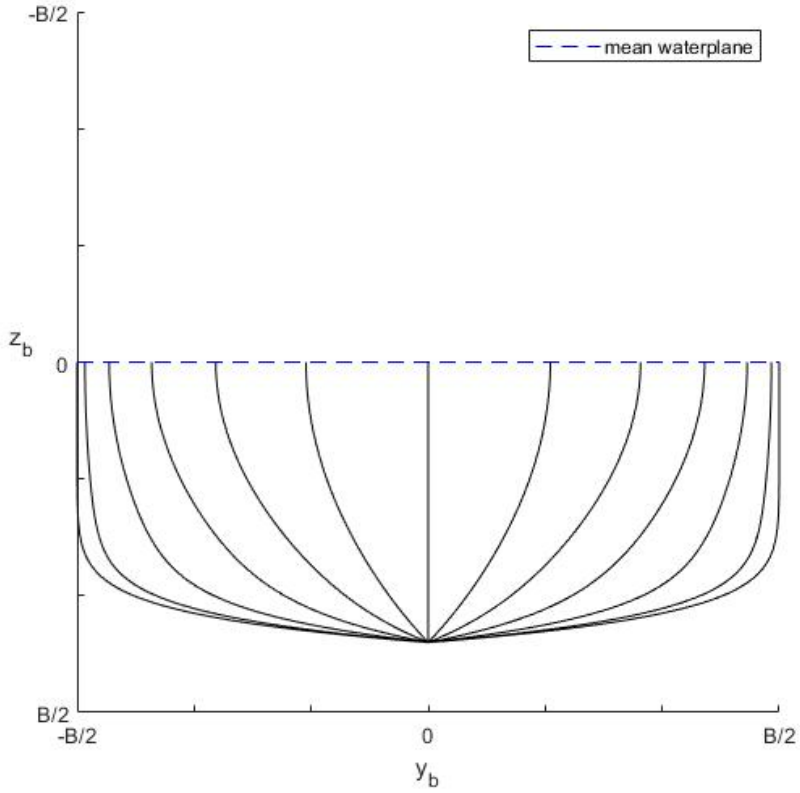

Figure 1.4: Wigley N43 hull transverse cuts

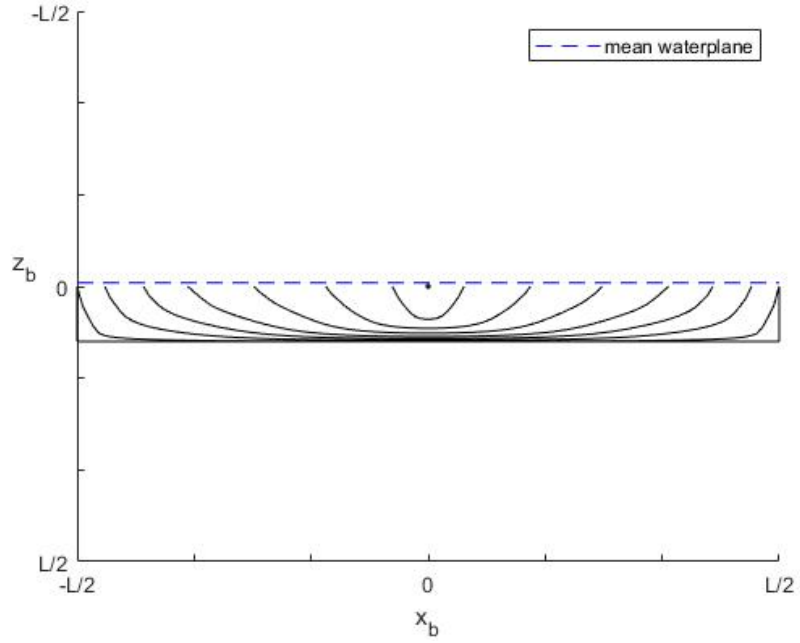

Figure 1.5: Wigley N43 hull longitudinal cuts

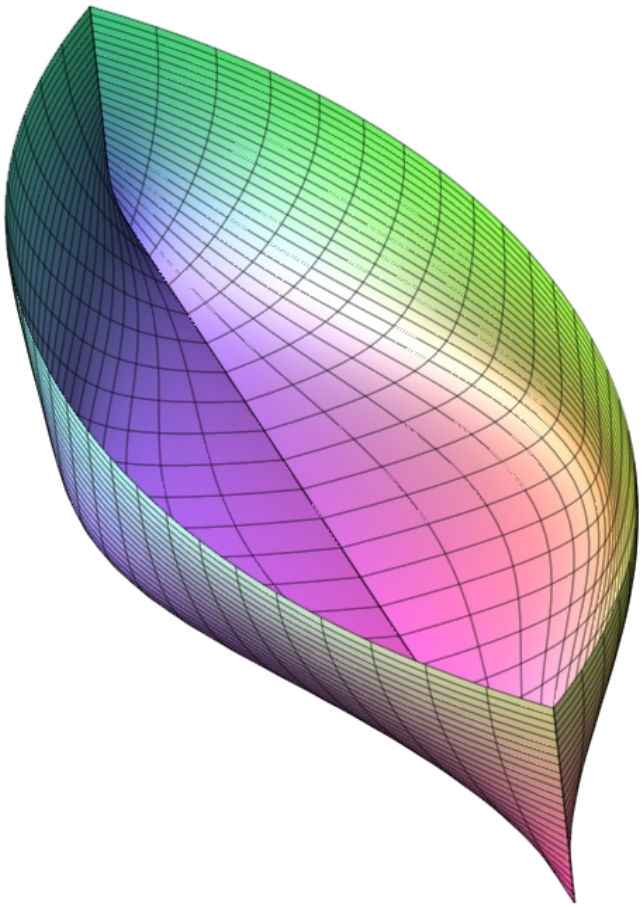

Figure 1.6: Wigley N43 hull 3D view

1.4.1 Volumes and Areas

The displaced volume of the Wigley N43 geometry can be determined as follows

$$V_{\text{disp}}(B,L,T) = \int_{-\frac{L}{2}}^{\frac{L}{2}} \int_{0}^{T} \int_{-y_+(x,z)}^{y_+(x,z)} dydzdx = \frac{29144}{51975} LBT \cong 0.56073LBT \tag{1.34}$$

which implies that the Wigley N43 geometry has a block coefficient, C_b, of about 0.56.

The area of an arbitrary waterplane cut can be determined as follows

$$A_{z_b}(z,L,B,T) = \int_{-\frac{L}{2}}^{\frac{L}{2}} \int_{-y_+(x,z)}^{y_+(x,z)} dydx = \frac{4LB}{1575T^{10}} \left(273T^{10} - 113T^8 z^2 - 160z^{10}\right) \cong \cdots$$
$$\frac{LB}{T^{10}} \left(0.69333T^{10} - 0.28698T^8 z^2 - 0.40635z^{10}\right) \tag{1.35}$$

This then yields $A_{z_b}(0,L,B,T) \cong 0.69333LB$ which, in turn, implies that the Wigley N43 geometry has a waterplane coefficient, C_{wp}, of about 0.69.

The area of an arbitrary transverse cut can be determined as follows

$$A_{x_b}(x,L,B,T) = \int_0^T \int_{-y_+(x,z)}^{y_+(x,z)} dydz = \frac{2BT(L^2-4x^2)}{165L^8}\left(75L^6 - 196L^4x^2 + 960L^2x^4 - 1280x^6\right) \cong \cdots$$
$$\frac{BT(L^2-4x^2)}{L^8}\left(0.90909L^6 - 2.37576L^4x^2 + 11.63636L^2x^4 - 15.51515x^6\right) \quad (1.36)$$

This then yields $A_{x_b}(0,L,B,T) \cong 0.90909BT$ which, in turn, implies that the Wigley N43 geometry has a midship section coefficient, C_m, of about 0.91. This then also implies a prismatic coefficient, $C_p = \frac{C_b}{C_m}$, of about 0.62.

The abeam projected area of the hull can be determined as follows

$$A_{\text{abeam}}(L,B,T) = \int_{-\frac{L}{2}}^{\frac{L}{2}} \int_0^T dzdx = LT \quad (1.37)$$

In order to determine the wetted area of the Wigley N43 hull, consider a differential area element of the hull

$$dA = (d\text{width})(d\text{height}) = \sqrt{dx^2+dy^2}\sqrt{dy^2+dz^2} \quad (1.38)$$

Since equation 1.33a gives the half-beam measure at point (x,z), it follows that

$$dA = \sqrt{\left(1+\left(\frac{\partial}{\partial x}y_+(x,z)\right)^2\right)\left(1+\left(\frac{\partial}{\partial z}y_+(x,z)\right)^2\right)}dxdz \quad (1.39)$$

And so, due to port-starboard symmetry, the wetted area of the Wigley N43 hull is given by

$$A_{\text{wetted}} = 2\int_0^T \int_{-\frac{L}{2}}^{\frac{L}{2}} \sqrt{\left(1+\left(\frac{\partial}{\partial x}y_+(x,z)\right)^2\right)\left(1+\left(\frac{\partial}{\partial z}y_+(x,z)\right)^2\right)}dxdz \quad (1.40)$$

Unfortunately, equation 1.40 does not yield a closed-form solution, and so it will have to be evaluated numerically on a case-by-case basis (although doing this, in general, is made simple by the availability of equation 1.33a).

Before concluding this subsection, it is worth noting that [Avallone et al., 2017, Tupper, 2013] give the following typical values for the form coefficients of merchant vessels

$$C_b \in [0.45, 0.85]$$
$$C_{wp} \in [0.65, 0.95]$$
$$C_m \in [0.90, 0.99]$$
$$C_p \in [0.60, 0.90]$$

Therefore, the form coefficients for the Wigley N43 geometry are within the typical ranges given by [Avallone et al., 2017, Tupper, 2013] for merchant vessels (albeit towards the lower bounds for C_{wp}, C_m, and C_p), and thus the N43 geometry is a realistic hull geometry.

1.4.2 Mass and Mass Moment of Inertia

The displaced mass of the Wigley N43 geometry can be determined as follows

$$m = \rho V_{\text{disp}} = \rho C_b LBT \quad (1.41)$$

where ρ is the density of the fluid displaced by the hull.

The mass moment of inertia (about O_b), in yaw, for the Wigley N43 hull, can be determined in the following manner. First, suppose the interior of the hull is filled uniformly with seawater having density ρ; then, by definition

$$I_{zz}^{O_b} = \int_{V_{\text{disp}}} ||\vec{r}_{dV}||_2^2 (\rho dV) \tag{1.42}$$

where $\vec{r}_{dV}$ is the vector from O_b to the differential volume element dV, projected onto the plane span(x_b, y_b). Equation 1.42 can be expressed equivalently as follows

$$I_{zz}^{O_b} = \rho \int_0^T \int_{-\frac{L}{2}}^{\frac{L}{2}} \int_{-y_+(x,z)}^{y_+(x,z)} (x^2 + y^2) dy dx dz \tag{1.43}$$

Fortunately, this multiple integral does yield the following closed-form expression (expressed approximately, after simplifying)

$$I_{zz}^{O_b} \cong \rho LBT(0.02875B^2 + 0.02637L^2) \tag{1.44}$$

Equivalent expressions for $I_{xx}^{O_b}$ and $I_{yy}^{O_b}$ can be generated in exactly the same manner; they are given approximately by

$$I_{xx}^{O_b} \cong \rho LBT(0.02875B^2 + 0.14246T^2) \tag{1.45}$$

$$I_{yy}^{O_b} \cong \rho LBT(0.02637L^2 + 0.14246T^2) \tag{1.46}$$

Now, in reality, the interior of the hull will not be filled uniformly with seawater, so one might introduce a correction factor to equation 1.44 in order to compensate for the fact that the term ρ in equation 1.42 should have been a function of location, $\rho(x, y, z)$, rather than a constant. Therefore, assume there exists a scalar $C_{\text{inertia}} \in (0, 1]$ such that

$$I_{zz}^{O_b} \cong C_{\text{inertia}} \rho LBT(0.02875B^2 + 0.02637L^2) \tag{1.47}$$

It follows that C_{inertia} is indeed in $(0, 1]$ because an inertia of less than zero makes no physical sense, an inertia of zero implies that there is no vessel, and a $C_{\text{inertia}} > 1$ would imply that the net density of the hull interior is greater than that of seawater, in which case the vessel would sink. Experimentation as part of the case studies performed in developing this thesis suggest $C_{\text{inertia}} \in [0.03, 0.07]$ for car-deck ferries (see Appendix A for details). At present, no other types of vessel have been investigated as part of this thesis, but presumably other types would admit different values of C_{inertia}. For instance, consider a fully-loaded tanker; the interior of the hull would be mostly filled uniformly with a liquid, and so, depending on the liquid density, C_{inertia} could approach 1 in this case.

1.4.3 Added Mass and Added Mass Moment of Inertia

In order to apply the foundational theory presented previously, one must be able to generate appropriate values with which to populate $\mathbf{M}_A$ (see equation 1.24). Fortunately, a general method for computing 2D added masses does exist; Sedov's technique, which is detailed in [Korotkin, 2009]. This technique can be described as follows.

Consider a 2D contour γ, and assume there exists a function $f(\xi)$ given by

$$f(\xi) = \frac{k}{\xi} + k_0 + k_1\xi + k_2\xi^2 + k_3\xi^3 + \cdots \tag{1.48}$$

which defines a conformal mapping from the unit disc in the ξ-plane to the exterior (filled with fluid) of the contour γ. Then, the 2D added masses λ_{11}, λ_{22}, and λ_{66} can be computed as follows

$$\lambda_{11} = -\rho(A_{\text{enclosed}} - 2\pi k\overline{k} + \pi(kk_1 + \overline{kk_1})) \tag{1.49a}$$

$$\lambda_{22} = -\rho(A_{\text{enclosed}} - 2\pi k\overline{k} - \pi(kk_1 + \overline{kk_1})) \tag{1.49b}$$

$$\lambda_{66} = \frac{i\rho}{2} \oint \overline{\omega_3}\left(\frac{1}{\xi}\right) \frac{d\omega_3}{d\xi} d\xi \tag{1.49c}$$

where A_{enclosed} is the area enclosed by the contour γ, and ω_3 is a complex function of ξ. For the special case of an ellipse, simple, closed-form solutions have been found. Consider an ellipse as follows

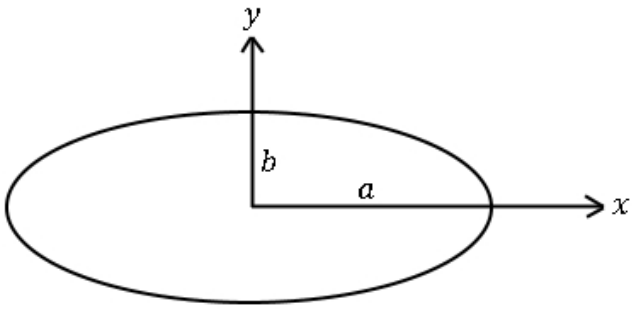

Figure 1.7: Ellipse contour

with x oriented forward, y oriented to starboard, a being the semi-major axis, and b being the semi-minor axis. The 2D added masses for this contour are [Korotkin, 2009]

$$\lambda_{11} = \rho\pi b^2 \tag{1.50a}$$

$$\lambda_{22} = \rho\pi a^2 \tag{1.50b}$$

$$\lambda_{66} = \frac{\rho\pi}{8}(a^2 - b^2)^2 \tag{1.50c}$$

$$\lambda_{12} = \lambda_{16} = \lambda_{26} = 0 \tag{1.50d}$$

with $\lambda_{12} = \lambda_{16} = \lambda_{26} = 0$ following from the symmetry of the ellipse. Consider, then, an arbitrary waterplane section of the Wigley N43 geometry enclosed within a bounding ellipse as follows

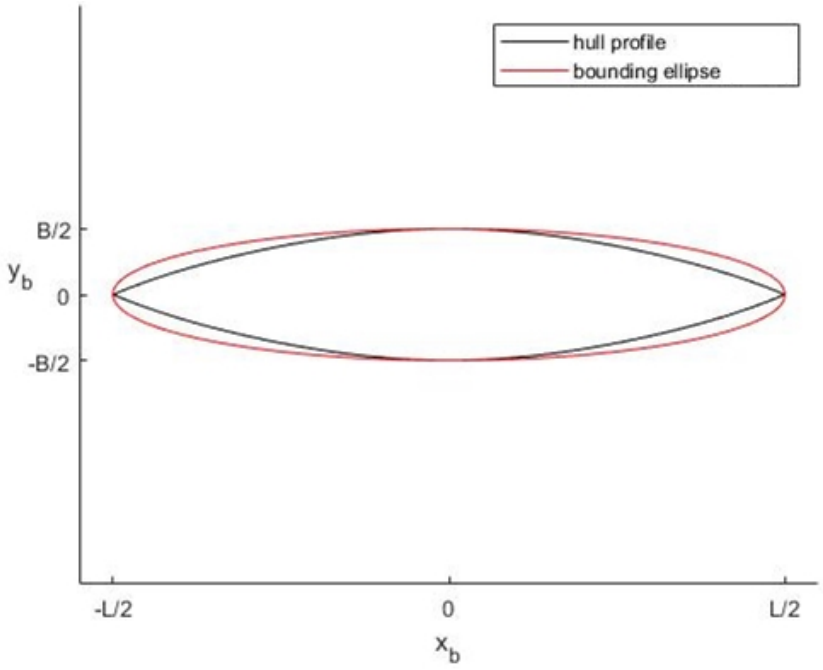

Figure 1.8: Waterplane bounding ellipse

Taking $b(z) = y_+(0, z)$ and $a(z) \equiv \frac{L}{2}$, as is the case for the Wigley N43 geometry, and integrating equations 1.50 over the vessel draft then yields the following added masses for the bounding ellipsoid[3]

$$A_{11}^{\text{ellipsoid}} = \frac{50\rho\pi}{231} B^2 T \tag{1.51a}$$

$$A_{22}^{\text{ellipsoid}} = \frac{\rho\pi}{4} L^2 T \tag{1.51b}$$

$$A_{66}^{\text{ellipsoid}} \cong \frac{\rho\pi T}{100}(0.78125L^4 - 1.35281L^2B^2 + 0.63862B^4) \tag{1.51c}$$

$$A_{12}^{\text{ellipsoid}} = A_{16}^{\text{ellipsoid}} = A_{26}^{\text{ellipsoid}} = 0 \tag{1.51d}$$

As for correcting equations 1.51 so as to better represent more realistic hull geometries, [Sen and Vinh, 2016] offer the following experimental results for a particular hull having $L = 170$ m, $B = 22.8$ m, and $T = 9.3$ m

$$A_{11} = 6.680 \times 10^5 \ \text{kg}$$

$$A_{22} = 2.171 \times 10^7 \ \text{kg}$$

$$A_{66} = 3.379 \times 10^{10} \ \text{kg.m}^2$$

Applying equations 1.51 to this same hull yields the following

$$A_{11}^{\text{ellipsoid}} = 3.370 \times 10^6 \ \text{kg}$$

$$A_{22}^{\text{ellipsoid}} = 2.164 \times 10^8 \ \text{kg}$$

$$A_{66}^{\text{ellipsoid}} = 1.894 \times 10^{11} \ \text{kg.m}^2$$

which shows that equations 1.51 are overestimating the added masses (as one might logically expect, since the ellipsoid is bounding). Therefore, in order to predict A_{11}, A_{22}, and A_{66} in general, one might scale equations 1.51 as follows

$$A_{11} \cong \frac{10\rho\pi}{231} B^2 T \tag{1.52a}$$

$$A_{22} \cong \frac{\rho\pi}{40} L^2 T \tag{1.52b}$$

$$A_{66} \cong \frac{\rho\pi T}{100}(0.13940L^4 - 0.24138L^2B^2 + 0.11395B^4) \tag{1.52c}$$

As for constructing a means of approximating A_{26}, which one cannot get from the bounding ellipsoid due to forward-aft symmetry, [Fossen, 2011] gives the following typical values for the added masses of a "conventional ship"

$$A_{11} = 1.4 \times 10^6 \ \text{kg}$$

$$A_{22} = 7.5 \times 10^6 \ \text{kg}$$

$$A_{26} = 4 \times 10^7 \ \text{kg.m}^2$$

$$A_{66} = 4.5 \times 10^9 \ \text{kg.m}^2$$

If "conventional ship" is taken to mean a merchant vessel on the order of $L = 115$ m, $B = 37.5$ m, and $T = 7$ m, then it is of interest to note that equations 1.52 yield, for this vessel, the following results

[3] It should be noted that these added masses are zero-frequency added masses, which is deemed appropriate for a surge-sway-yaw model such as the one applied in this thesis [Fossen, 2011].

$$A_{11} \cong 1.372 \times 10^6 \ \text{kg}$$

$$A_{22} \cong 7.453 \times 10^6 \ \text{kg}$$

$$A_{66} \cong 4.535 \times 10^9 \ \text{kg.m}^2$$

The "conventional ship" results of Fossen then suggest the following approximation scheme for A_{26}

$$\begin{gathered} \text{IF vessel has forward-aft symmetry, THEN} \\ A_{26} = 0 \\ \text{ELSE} \\ A_{26} \cong \frac{A_{66}}{10^{\lfloor \log_{10}(A_{66}) \rfloor}} \times 10^{\lfloor \log_{10}(A_{22}) \rfloor + 1} \end{gathered} \tag{1.53}$$

that is, for vessels lacking forward-aft symmetry, let A_{26} be the significand of A_{66} muliplied by 10 raised to the power order of A_{22} plus one. A_{12} and A_{16} will always be zero due to port-starboard symmetry (which is present in general). Equations 1.52, along with equation 1.53, thus allow one to rapidly generate approximate values for added masses in general.

1.5 Surrogate Geometry II - Wageningen B-Series Propeller

In order to fully determine the propeller states for a seagoing vessel, it is necessary to define the geometry of the propeller(s). This, however, will vary from case to case depending on the particular design of the vessel under consideration. Since this thesis seeks general results, a compromise between accuracy, generality, and simplicity will therefore once again have to be struck. To that end, this thesis will assume a Wageningen B-series geometry. This particular geometry can be illustrated as follows

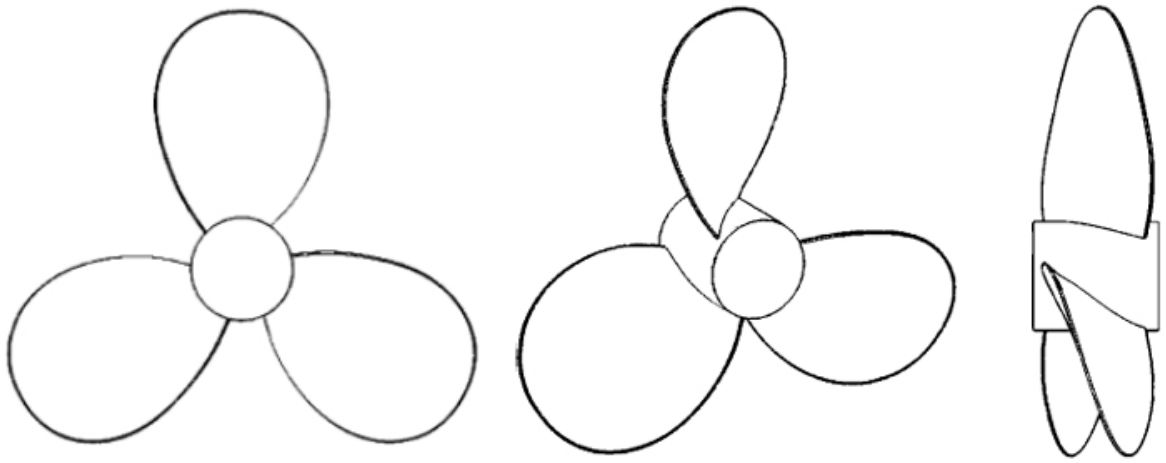

Figure 1.9: Wageningen B-series propeller, three blade variant (adapted from [Yeo et al., 2014])

This geometry is chosen because the work of [Bernitsas et al., 1981] provides general results for determining thrust coefficients, K_T, and torque coefficients, K_Q, given basic propeller properties. Using this work, it is possible to define general functions[4]

$$K_T = f_1\left(J, \frac{P}{D}, \frac{A_b}{A_s}, n_{\text{blades}}, \text{Re}_D\right) \tag{1.54a}$$

[4]Indeed, such functions are already defined, in polynomial form, in [Bernitsas et al., 1981]. They are quite long, however, and so are not re-printed here.

$$K_Q = f_2\left(J, \frac{P}{D}, \frac{A_b}{A_s}, n_{\text{blades}}, \text{Re}_D\right) \tag{1.54b}$$

where P is propeller pitch, D is propeller diameter, A_b is total blade face area, A_s is swept area, n_{blades} is the number of propeller blades, and Re_D is Reynolds number at characteristic length D. J is advance ratio, defined as

$$J = \frac{V_{\text{flow}}}{(\text{rps})D} \tag{1.55}$$

with V_{flow} being fluid speed relative to the propeller, and rps being propeller speed in revolutions per second. Since K_T and K_Q are defined as

$$K_T = \frac{T_{\text{prop}}}{\rho(\text{rps})^2 D^4} \tag{1.56a}$$

$$K_Q = \frac{Q_{\text{prop}}}{\rho(\text{rps})^2 D^5} \tag{1.56b}$$

it follows that one can construct general functions for propeller thrust, T_{prop}, and propeller torque, Q_{prop}

$$T_{\text{prop}} = \rho f_1(\cdots)(\text{rps})^2 D^4 \tag{1.57a}$$

$$Q_{\text{prop}} = \rho f_2(\cdots)(\text{rps})^2 D^5 \tag{1.57b}$$

It should be noted, however, that equations 1.57 will inherit the same limits of applicability exhibited by equations 1.54, namely

$$2 \leq n_{\text{blades}} \leq 7$$

$$0.30 \leq \tfrac{A_b}{A_s} \leq 1.05$$

$$0.5 \leq \tfrac{P}{D} \leq 1.40$$

1.6 Second-Order Wave Dynamics

As per [Fossen, 2011, Pinkster, 1971], the forces and moments upon a vessel due to wave encounter can be split into two components

1) a zero-mean oscillatory component (i.e., first-order wave dynamics); and,

2) a slowly varying wave drift component (i.e., second-order wave dynamics)

it is then generally assumed that these components are additive as follows [Fossen, 2011]

$$\tau_{\text{waves}} = \tau_{\text{waves1}} + \tau_{\text{waves1}}$$

where the τ_{waves1} and τ_{waves2} terms are the first and second-order components, respectively. However, as per [Pinkster, 1971], seeking to design a vessel which can counteract the forces and moments due to the first-order component usually leads to the requirement for impractically large and highly dynamic thruster forces[5]; this, in turn, would place a great deal of strain upon the vessel's machinery. Therefore, the first-order wave component is generally not considered as part of a dynamic positioning or path following problem and, as such, is ignored in this thesis. The handling of the second-order component, however, is presented below.

[5]For example, consider the forces required to restrain a periodic motion in one dimension; let these forces be defined by $F(t) = (m + m_A)\frac{d^2}{dt^2}(x_0 \cos(\omega t)) = -(m + m_A)x_0\omega^2 \cos(\omega t)$. For the case of $m + m_A = 3.35 \times 10^6$ kg, $x_0 = 1$ m, and $\omega = \frac{2\pi}{9}$ rad/s, the maximum magnitude of $F(t)$ would be $(m + m_A)x_0\omega^2 = 1.63 \times 10^6$ N. For a vessel of about 3100 tonnes displacement, this amount of thrust is excessive and likely exceeds the capabilities of the vessel's plant altogether.

1.6.1 Statistics from Variance Density

Suppose one wishes to describe the sea surface at a point. One way to do so is to observe the change in surface elevation, η, at that point and then construct from that a cosine series of the form [NDBC, 1996]

$$\eta(\theta, t) = \sum_{i=0}^{\infty} a_i D(f_i, \theta) \cos(2\pi f_i t + \phi_i)$$

where θ is wave heading (in $\{n\}$), t is time, a_i is the amplitude of the i^{th} wave mode, $D(\ )$ is a direction and frequency dependent spreading function, f_i is the frequency of the i^{th} wave mode, and ϕ_i is the phase shift of the i^{th} wave mode. By definition, the total variance in η is given by

$$\text{var}(\eta) = \sigma_\eta^2 = \text{E}[\eta^2] - \text{E}[\eta]^2$$

where E[ ] denotes expected value. Assuming $\text{E}[\eta] = 0$, this then simplifies to

$$\sigma_\eta^2 = \text{E}[\eta^2]$$

which can be shown (by way of orthogonality), for an appropriately defined spreading function $D(\ )$, to return

$$\sigma_\eta^2 = \frac{1}{2} \sum_{i=0}^{\infty} a_i^2$$

Therefore, the variance in η follows strictly from the wave mode amplitudes. This motivates the introduction of a wave variance density spectrum, $E(f, \theta)$, which encodes the variance density of each (f, θ) component of the overall sea surface at a point. An example variance density spectrum might look like the following

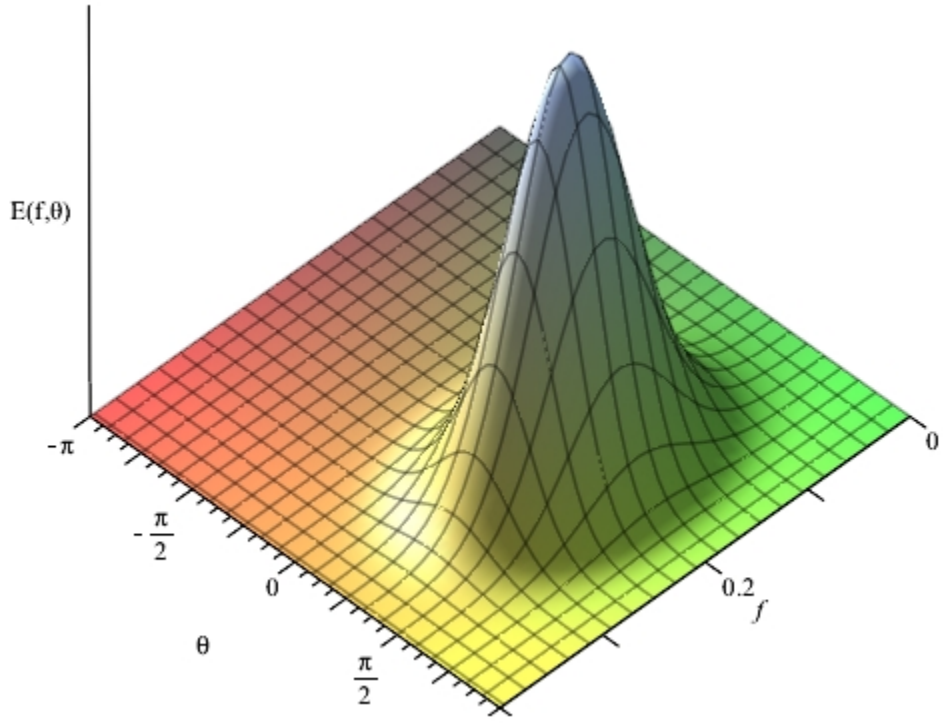

Figure 1.10: Example directional wave spectrum

Given a variance density spectrum, one can extract various statistical measures as follows

$$\sigma_\eta^2 = \int_0^{2\pi} \int_0^{\infty} \mathrm{E}(f,\theta)\ df d\theta \tag{1.58}$$

$$f_p = \frac{1}{\sigma_\eta^2} \int_0^{2\pi} \int_0^{\infty} \mathrm{E}(f,\theta) f\ df d\theta \tag{1.59}$$

$$\theta_p = \frac{1}{\sigma_\eta^2} \int_0^{2\pi} \int_0^{\infty} \mathrm{E}(f,\theta) \theta\ df d\theta \tag{1.60}$$

$$H_s = 4\sqrt{\sigma_\eta^2} \tag{1.61}$$

where equation 1.58 recovers the total variance in mode amplitudes, equation 1.59 gives the peak, or dominant, wave frequency, equation 1.60 gives the peak, or dominant, wave heading, and equation 1.61 gives the so-called significant wave height (i.e., the mean height of the highest 1/3 of waves encoded in the spectrum). From the peak wave frequency, one can define the peak wave period as

$$T_p = \frac{1}{f_p} \tag{1.62}$$

which is a representative measure of the period of the higher wave modes [NDBC, 1996]. From this, it follows that a condensed description of the sea surface at a point can be given by (H_s, T_p, θ_p).

1.6.2 Wave Heights as a Random Variable

Given a condensed sea surface description, it is possible to model the probability density of wave heights, H, according to a Rayleigh distribution as follows[6] [Buckham, 2017]

$$\mathrm{PDF}(H) = \frac{H}{4\sigma_\eta^2} \exp\left(\frac{-H^2}{8\sigma_\eta^2}\right) \tag{1.63}$$

Invoking equation 1.61 and simplifying then yields

$$\mathrm{PDF}(H) = \frac{4H}{H_s^2} \exp\left(\frac{-2H^2}{H_s^2}\right) \tag{1.64}$$

For example, under this model, the wave height probability density of a sea having $H_s = 2.4$ m would present as follows

[6] Assuming the underlying variance density spectrum is unimodal and narrow, as in figure 1.10 for instance.

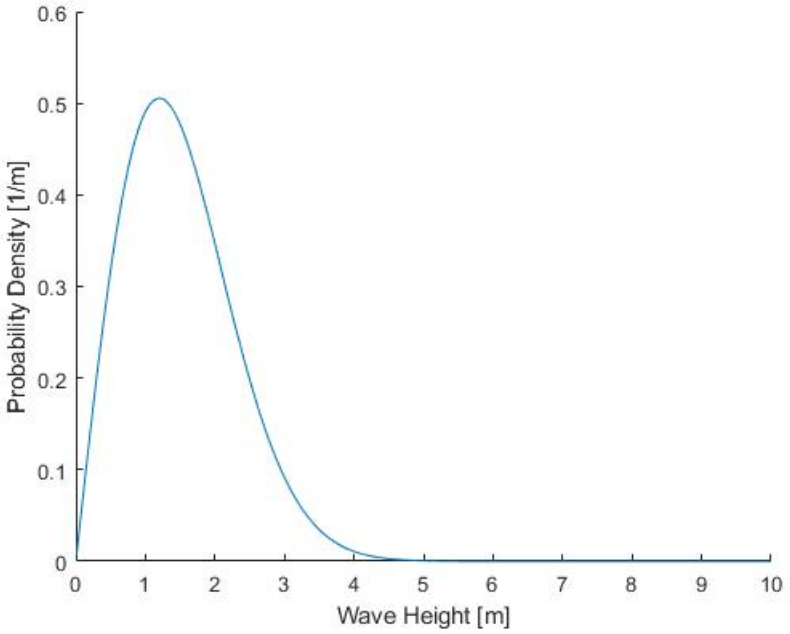

Figure 1.11: Example Rayleigh distribution ($H_s = 2.4$ m)

In addition, under this model, it can be shown that

$$\Pr[H \leq 0.02H_s] \cong 0.001 \tag{1.65a}$$

$$\Pr[H \leq 2H_s] \cong 0.999 \tag{1.65b}$$

since

$$\int_0^{\frac{H_s}{50}} \text{PDF}(H)dH = 1 - e^{-\frac{1}{1250}} \cong 0.00080$$

$$\int_0^{2H_s} \text{PDF}(H)dH = 1 - e^{-8} \cong 0.99966$$

Therefore, one can assume $0.02H_s$ to be a lower bound and $2H_s$ to be an upper bound on the wave heights one might reasonably expect to encounter when in a sea having significant wave height H_s.

1.6.3 Determining Wave Number from Condensed Description

One consequence of linear wave theory is the dispersion relation, given as follows

$$\omega^2 = gk \tanh(kh) \tag{1.66}$$

where ω is the angular frequency of a wave, defined by

$$\omega = \frac{2\pi}{T} \tag{1.67}$$

with T being wave period, g is acceleration due to gravity, k is wave number, defined by

$$k = \frac{2\pi}{\lambda} \tag{1.68}$$

with λ being wave length, and h is sea depth. Given a condensed description (H_s, T_p, θ_p) and the sea depth, h, at a point, one might solve for the peak wave number, k_p, given implicitly by dispersion as follows

$$\left(\frac{2\pi}{T_p}\right)^2 = gk_p \tanh(k_p h) \tag{1.69}$$

With this k_p in hand, one might assume wave number to be a function of wave height as follows

$$k(H) = cH^{-0.8}$$

where c is an arbitrary constant. The proposed exponent of -0.8 follows from the average wave length vs average wave height data provided in [Ellis and Garrison, 2016]. If one then requires that $k(H_s) = k_p$, then the constant c is defined and the following model results

$$k(H) = k_p \left(\frac{H_s}{H}\right)^{0.8} \tag{1.70}$$

For example, for a sea surface described by $H_s = 2.4$ m, $T_p = 13$ s, and $\theta_p = 4.974$ rad (i.e., heading 285), at a point having depth 3200 m, the peak wave number is $k_p = 0.0238$ 1/m. Plotting the wave numbers $k(H)$ over the interval $H \in [0.02H_s, 2H_s]$ then yields figure 1.12. The corresponding wave length vs height plot is illustrated in figure 1.13. Of note is the fact that figures 1.12 and 1.13 both illustrate values consistent with wave lengths reported as typical in [Sandwell, 2010, FCIT, 2005, Janssen, 2004].

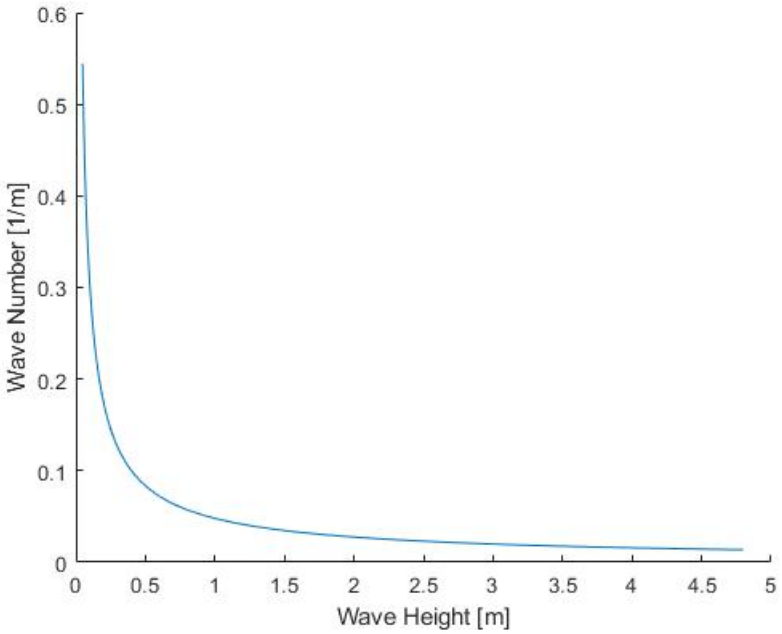

Figure 1.12: Example wave number vs height plot

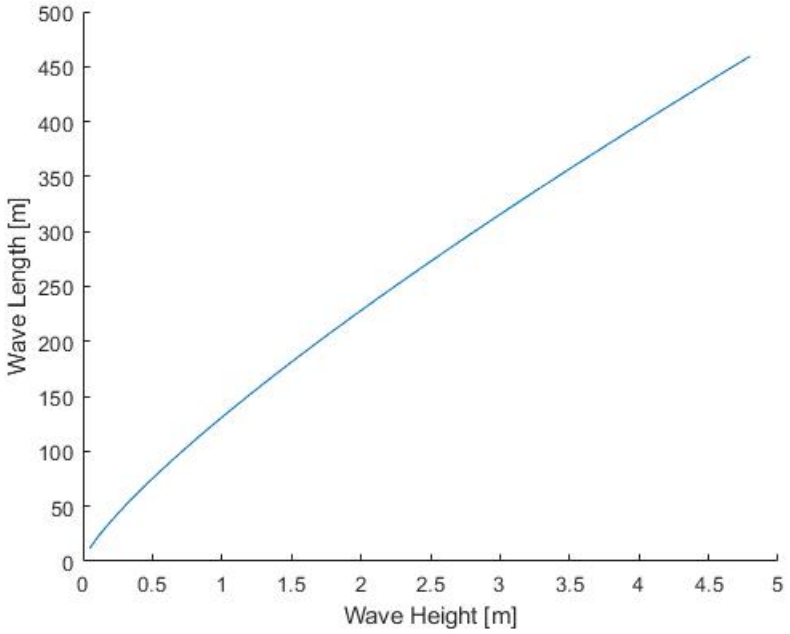

Figure 1.13: Example wave length vs height plot

1.6.4 Computing Wave-Drift over Vessel Draft

A classical result due to [Stokes, 1880] defines the horizontal drift velocity of particles throughout the depth of an ocean wave as follows (with depth, z, oriented positive downward)

$$\overline{u}_S = \frac{1}{8}\omega k H^2 \frac{\cosh(2k(h-z))}{\sinh^2(kh)} \tag{1.71}$$

Given a condensed sea surface description, one can, for any given wave height H, define the corresponding wave number, $k(H)$, by way of equation 1.70 defined previously. With this value in hand, one can then define the corresponding angular frequency, $\omega(H)$, by way of dispersion as follows

$$\omega(H) = \sqrt{gk(H)\tanh(k(H)h)} \tag{1.72}$$

The wave parameters of equation 1.71, ω and k, can therefore be defined entirely in terms of H. Finally, one might define an expected drift over the vessel draft, T, as follows

$$\mathrm{E}[\overline{u}_S] = \frac{1}{T}\int_0^T \int_{0.02H_s}^{2H_s} \overline{u}_S \mathrm{PDF}(H) dH dz \tag{1.73}$$

Note that this is effectively a current with magnitude $\mathrm{E}[\overline{u}_S]$ and heading θ_p, and so the effect of second-order wave dynamics can be captured in equation 1.32 by including wave drift within the definition of ν_r. Equation 1.32 thus reduces to

$$\underbrace{\mathbf{M}_{RB}\dot{\nu} + \mathbf{C}_{RB}(\nu)\nu}_{\text{rigid-body dynamics}} + \underbrace{\mathbf{M}_A\dot{\nu}_r + \mathbf{C}_A(\nu_r)\nu_r + \mathbf{D}(\nu_r)\nu_r}_{\text{hydrodynamics}} = \underbrace{\tau_{\text{control}} + \tau_{\text{wind}}}_{\text{external forces}} \tag{1.74}$$

Chapter 2

Practical Implementation

In this chapter, the details of implementing the process illustrated in figure 2 are presented. First, the handling of the kinematics is summarized, including how to generate the required body-fixed velocities and accelerations. In addition, the kinematics portion also touches upon the practical concern of necessary filtering when approximating derivatives using finite differences. The kinetics portion then handles populating the elements of equation 1.74 in order to allow for the generation of the required control forces and moments. The kinetics portion also discusses how to correct for the effect of hull fouling on drag. Then, the propeller dynamics portion discusses how to generate sufficient propeller states from given control forces and moments. This portion includes several important results, including how to define the propeller thrust vectors for an arbitrary number and placement of propellers, as well as how to correct for effects, on generated thrust and required torque, due to oblique inflow, the presence of a propeller nozzle, and propeller fouling. The steering dynamics portion then discusses how to generate sufficient steering gear states from given propeller states. This portion also includes the introduction of a generalized steering gear model. Finally, a method for generating appropriate characteristic periods, in surge, sway, yaw, propeller dynamics, and steering dynamics, is developed.

2.1 Modelling Kinematics

2.1.1 Defining ν

Recall the formula given by equation 1.3

$$\begin{bmatrix} u \\ v \\ r \end{bmatrix} = \begin{bmatrix} \cos(\psi) & \sin(\psi) & 0 \\ -\sin(\psi) & \cos(\psi) & 0 \\ 0 & 0 & 1 \end{bmatrix} \begin{bmatrix} \frac{dx_n}{dt} \\ \frac{dy_n}{dt} \\ \frac{d\psi}{dt} \end{bmatrix}$$

For the purpose of this thesis, suppose one has only a partial and discrete mission cycle; that is, a sequence of n waypoints $\{(t_i, \mu_i, l_i)\}$ only. In order to begin generating the corresponding drive cycle, one might first approximate $\frac{d\mu}{dt}$ and $\frac{dl}{dt}$ by way of finite differences

$$\frac{d\mu}{dt} \approx \frac{\mu(t + \Delta t) - \mu(t)}{\Delta t} \tag{2.1a}$$

$$\frac{dl}{dt} \approx \frac{l(t + \Delta t) - l(t)}{\Delta t} \tag{2.1b}$$

for sufficiently small values of Δt. However, the given mission cycle may be sparse; that is, only a few waypoints spanning the vessel's mission. In this case, the mission cycle will have to be filled out in order to ensure that the max Δt between any two successive waypoints is sufficiently small for the purpose of equations 2.1. This can be accomplished by way of cubic spline interpolation over the given mission cycle. Suppose the vectors `t`, `lat`, and `long`, together defining a sparse and partial mission cycle, are loaded into a computer. Given these inputs, the following pseudocode describes a process by which one can generate a sufficiently dense sequence $\{(t_i, \mu_i, l_i)\}$.

```
guess initial value for interpolation resolution interp_res;

while max(dt_fill) > tolerance_dt
    map from t to the interval [0,1] such that t(0) --> 0 and t(end) --> 1;
    interpolate over [0,1] --> t to generate t_fill such that t_fill spans t and t_fill
        contains interp_res number of points;
end

interpolate over t --> lat in order to generate the mapping t_fill --> lat_fill such
    that lat_fill spans lat;
interpolate over t --> long in order to generate the mapping t_fill --> long_fill such
    that long_fill spans long;
```

Assume, then, that a sequence of appropriate values for $\frac{d\mu}{dt}$ and $\frac{dl}{dt}$ have been generated by way of finite differences as follows

```
for i = 1:(end - 1)
    dlat_dt(i) = (lat_fill(i + 1) - lat_fill(i))/(t_fill(i + 1) - t_fill(i));
    dlong_dt(i) = (long_fill(i + 1) - long_fill(i))/(t_fill(i + 1) - t_fill(i));
end

use a sliding Hampel filter to remove spikes due to zero-crossing events;

use linear interpolation to generate dlat_dt(end) and dlong_dt(end) values;
```

By applying equations 1.2, one can then generate appropriate values for $\frac{dx_n}{dt}$ and $\frac{dy_n}{dt}$. Finally, if one assumes that the vessel's heading is everywhere tangent to its trajectory (that is, $v \approx 0$), then one can recover values for ψ by way of

$$\psi(t) = \arctan\left(\left(\frac{dy_n}{dt}\right)\left(\frac{dt}{dx_n}\right)\right) \tag{2.2}$$

One implementation issue with equation 2.2, however, is spikes due to $\frac{dx_n}{dt} \to 0$ or $\frac{dy_n}{dt} \to 0$; fortunately, this can be mitigated as follows. Suppose the vectors `dxn_dt` and `dyn_dt` are loaded into a computer; then

```
for i = 1:end
    head(i) = arctangent(dyn_dt(i)/dxn_dt(i));
end

use a sliding Hampel filter to remove spikes;
```

One can then generate values for $\frac{d\psi}{dt}$ in the same manner as that applied above to generate $\frac{d\mu}{dt}$ and $\frac{dl}{dt}$ values. Finally, given the $v \approx 0$ assumption, it follows that the corresponding drive cycle can be generated as follows

$$u(t) = \cos(\psi)\frac{dx_n}{dt} + \sin(\psi)\frac{dy_n}{dt} \tag{2.3a}$$

$$v(t) \equiv 0 \tag{2.3b}$$

$$r(t) = \frac{d\psi}{dt} \tag{2.3c}$$

with r being expressed in terms of rad/s.

2.1.2 Defining ν_r

Recall that ν_r is defined, as per equation 1.21c (with $v \approx 0$), by

$$\nu_r = \begin{bmatrix} u - u_c \\ -v_c \\ r \end{bmatrix} \tag{2.4}$$

If one then defines the current terms, u_c and v_c, as follows [Fossen, 2011]

$$u_c = U_c \cos(\theta_c - \psi) + \mathrm{E}[\overline{u}_S] \cos(\theta_p - \psi) \tag{2.5a}$$

$$v_c = U_c \sin(\theta_c - \psi) + \mathrm{E}[\overline{u}_S] \sin(\theta_p - \psi) \tag{2.5b}$$

where U_c and θ_c are the magnitude and heading, respectively, of the fluid current at (t, μ, l), and $\mathrm{E}[\overline{u}_S]$ and θ_p are as defined previously at (t, μ, l), then it follows that one can generate appropriate values for ν_r given sufficient data on weather conditions. Specifically, one would need data on U_c, θ_c, H_s, T_p, θ_p, and h everywhere over the mission cycle of the vessel.

2.1.3 Filtering ν and ν_r

A practical concern in approximating derivatives by way of finite differences is the amplification of high frequency noise, generated in this case by the rounding errors inherent in floating point arithmetic. Therefore, the kinematics generated thus far (that is, ν and ν_r) will need to be filtered in order to remove this noise. This thesis will apply a moving average filter in all such cases, but the size of the sliding window is dependent on characteristic periods of the vessel in question. For now, introduce characteristic periods T_{surge}, T_{sway}, and T_{yaw}, for which typical values are on the order of 100 to 250 seconds [Fossen, 2011]. How these characteristic periods can be determined in general, however, will have to wait until a later section as results for both drag and propeller dynamics will have to be presented first. Still, how the characteristic periods will be used in filtering is presented here.

Consider one period of a cosine wave contaminated with white noise (bounded to within +/- 5% of wave amplitude)

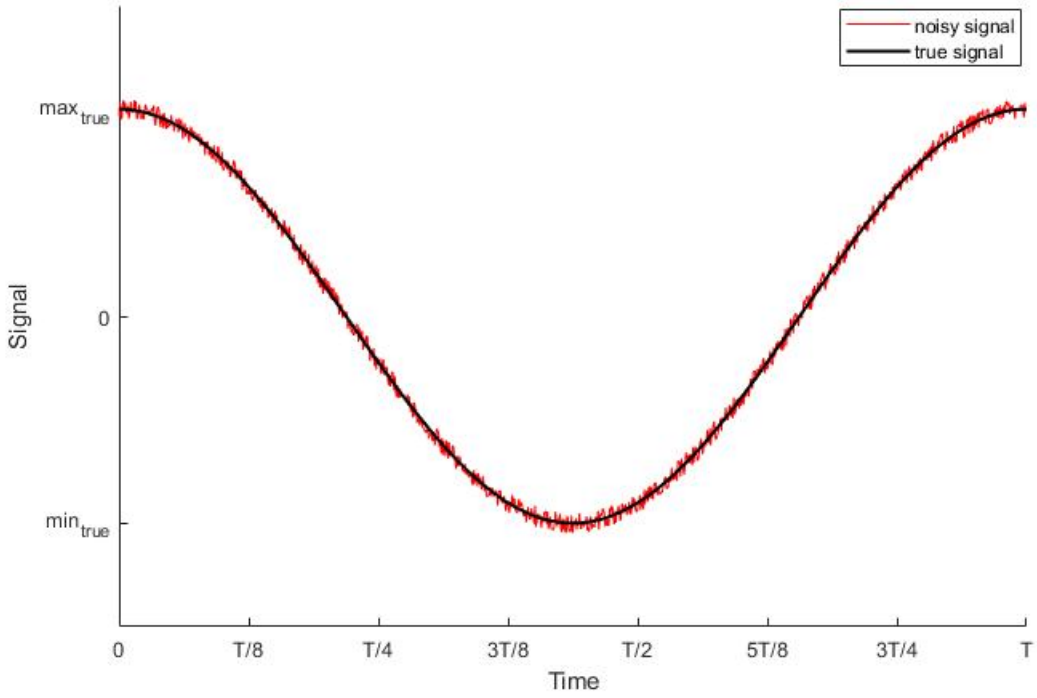

Figure 2.1: Noisy cosine wave

By applying a moving average filter, with sliding windows varying from one period, T, to one eighth of a period, $\frac{T}{8}$, the results illustrated in figures 2.2 and 2.3 were generated.

Figures 2.2 and 2.3 show that, as the smoothing window was decreased to $\frac{T}{8}$, good convergence on the true signal was achieved. Indeed, at this level of filtering, the maximum error between the true signal and filtered signal was found to be bounded to within +/- 1.5% of the true signal amplitude. In addition, at this level of filtering, no evidence of over-fitting was observed; that is, the noise did not present in the filtered signal. Therefore, it is judged that, for the purpose of this thesis, where filtering is necessary, it suffices to filter using a window of one eighth of the appropriate characteristic period.

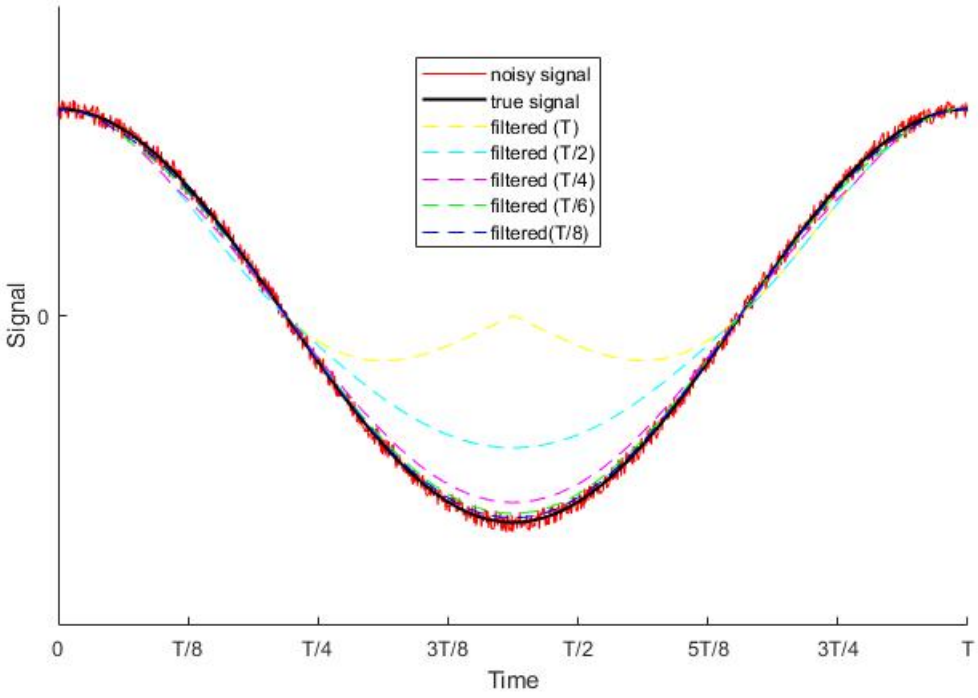

Figure 2.2: Results of filtering the noisy cosine wave, $t \in [0, T]$

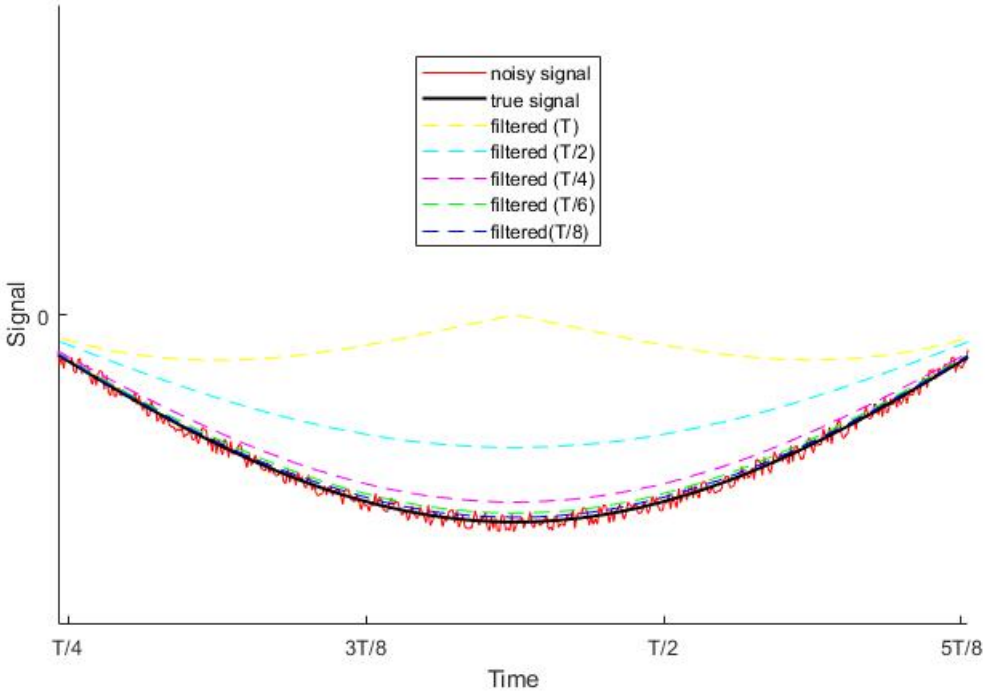

Figure 2.3: Results of filtering the noisy cosine wave, $t \in [\frac{T}{4}, \frac{5T}{8}]$

2.1.4 Defining $\dot{\nu}$ and $\dot{\nu_r}$

Values for $\dot{\nu}$ and $\dot{\nu_r}$ can be generated by way of finite differences, given values for ν and ν_r, as per the methodology presented above.

2.2 Modelling Kinetics

The elements of $\mathbf{M}_{RB}$ can be either extracted from the vessel's manual of trim and stability (if available), or can be approximated using the foundational theory for the Wigley N43 geometry. The elements of $\mathbf{M}_A$ can be generated by using equations 1.52 and 1.53. Subsequently, the elements of $\mathbf{C}_{RB}(\nu)$ and $\mathbf{C}_A(\nu_r)$, albeit variable over the mission cycle, follow entirely from the elements of $\mathbf{M}_{RB}$, $\mathbf{M}_A$, ν, and ν_r, and thus are fully defined if given these.

2.2.1 Damping Matrix

Recall that the damping matrix, $\mathbf{D}(\nu_r)$, is constructed from the superposition of a linear damping matrix and a non-linear damping matrix. This subsection will handle how to determine the elements of $\mathbf{D}$ and $\mathbf{D}_n(\nu_r)$.

Defining D

The diagonal elements of $\mathbf{D}$ are defined in [Fossen, 2011] as follows

$$B_{11V} = \frac{m + A_{11}}{T_{\text{surge}}} \tag{2.6a}$$

$$B_{22V} = \frac{m + A_{22}}{T_{\text{sway}}} \tag{2.6b}$$

$$B_{66V} = \frac{I_{zz}^{O_b} + A_{66}}{T_{\text{yaw}}} \tag{2.6c}$$

with the $T_{(\ )}$'s being characteristic periods of surge, sway, and yaw dynamics, respectively (the generation of these characteristic periods will be handled in a later section). The off-diagonal elements of $\mathbf{D}$ can be deduced from semi-empirical results due to [Bandyk, 2009] as follows

$$-Y_r = \frac{1}{2}\pi\rho L^3 \left(\frac{T}{L}\right)^2 \left(-\frac{1}{2} + \frac{11}{5}\left(\frac{B}{L}\right) - \frac{2}{25}\left(\frac{B}{T}\right)\right) \overline{\nu_{r1}} \tag{2.7}$$

$$-N_v = \frac{1}{2}\pi\rho L^3 \left(\frac{T}{L}\right)^2 \left(\frac{1}{2} + \frac{12}{5}\left(\frac{T}{L}\right)\right) \overline{\nu_{r1}} \tag{2.8}$$

where $\overline{\nu_{r1}}$ is a measure of mean ship relative speed, given by

$$\overline{\nu_{r1}} = \frac{1}{T_{\text{mission}}} \int_0^{T_{\text{mission}}} \sqrt{u_r^2 + v_r^2}\, dt \tag{2.9}$$

with T_{mission} being mission duration. The linear damping matrix is thus fully defined.

Defining $\mathbf{D}_n(\nu_r)$

For the purpose of this thesis, it is easier to handle the non-linear damping as a force/moment vector, rather than as a matrix times a relative velocity. The non-linear damping forces/moments F_{un}, F_{vn}, and M_{rn} can be determined as follows [Fossen, 2011, USNA, 2007]

$$F_{un} = F_{unV} + F_{unW} \tag{2.10}$$

$$F_{vn} = -\frac{1}{2}\rho T \int_{-\frac{L}{2}}^{\frac{L}{2}} C_d^{2D}(x)|v_r + xr|(v_r + xr)dx \tag{2.11}$$

$$M_{rn} = -\frac{1}{2}\rho T \int_{-\frac{L}{2}}^{\frac{L}{2}} C_d^{2D}(x)x|v_r + xr|(v_r + xr)dx \tag{2.12}$$

where F_{unV} is the non-linear component, in surge, due to viscous drag (friction and form), F_{unW} is the non-linear component, in surge, due to wave-making, and C_d^{2D} is a 2D drag coefficient. Note that equations 2.11 and 2.12 represent cross-flow drag, in sway and yaw, following from a strip theory approach. One can, as per [Fossen, 2011], approximate the 2D drag coefficients using a generalized curve due to [Hoerner, 1965] which may be expressed as follows

$$C_d^{2D}\left(\frac{B(x)}{2T}\right) \cong 1.5949 \exp\left(-2.7160\left(\frac{B(x)}{2T}\right)^2 + 0.1885\left(\frac{B(x)}{2T}\right) - 0.1462\right) + 0.6405 \tag{2.13}$$

plotting this curve over the interval $\left(\frac{B}{2T}\right) \in [0, 4]$ then yields the following

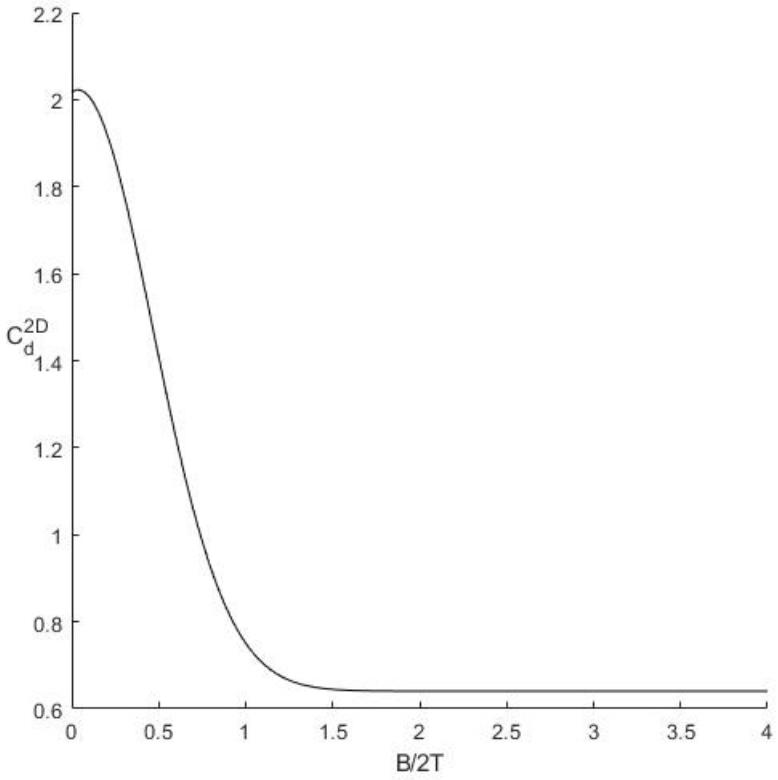

Figure 2.4: Hoerner curve (C_d^{2D})

By taking $B(x) = 2y_+(x, 0)$ in equation 2.13, one can evaluate equations 2.11 and 2.12 for any given drive cycle, current conditions, and hull dimensions.

As for F_{un}, the non-linear viscous drag component can be defined as [Fossen, 2011, USNA, 2007]

$$F_{unV} = -\frac{3}{5}\rho C_V A_{\text{wetted}}|u_r|u_r \tag{2.14}$$

where the coefficient $\frac{3}{5}$, as opposed to $\frac{1}{2}$, follows from a 15% - 20% additional drag allowance for typical hull appendages[1] [Hoerner, 1965], and C_V is a viscous drag coefficient defined by

$$C_V = (1 + K)C_f \tag{2.15}$$

with the form factor, K, being defined approximately by [USNA, 2007]

$$K \cong 19 \left(\frac{C_b B}{L} \right)^2 \tag{2.16}$$

and the friction drag coefficient, C_f, being a function of Reynolds number, Re_L, as follows [Fossen, 2011,USNA, 2007,ITTC, 1957]

$$C_f = \frac{3}{40(\log_{10}(\mathrm{Re}_L) - 2)^2} \tag{2.17}$$

with Reynolds number being given, in this case, by

$$\mathrm{Re}_L = \frac{\rho u_r L}{\mu}$$

with μ being the dynamic viscosity of the fluid.

The non-linear wave-making component can be expressed similarly by

$$F_{unW} = -\frac{1}{2}\rho C_w A_{\mathrm{wetted}} |u_r| u_r \tag{2.18}$$

where C_w is a wave-making coefficient. The following semi-empirical results due to [bin Tarafder et al., 2007] give C_w as a function of Froude number, Fr_L, for a Wigley hull having a rectangular midship section (similar to the N43 geometry)

[1] I.e., propeller(s), propeller A-brace(s), rudder(s), stabilizer(s), etc. In marine engineering parlance, this is also often referred to as a thrust deduction factor [MIT, 2004].

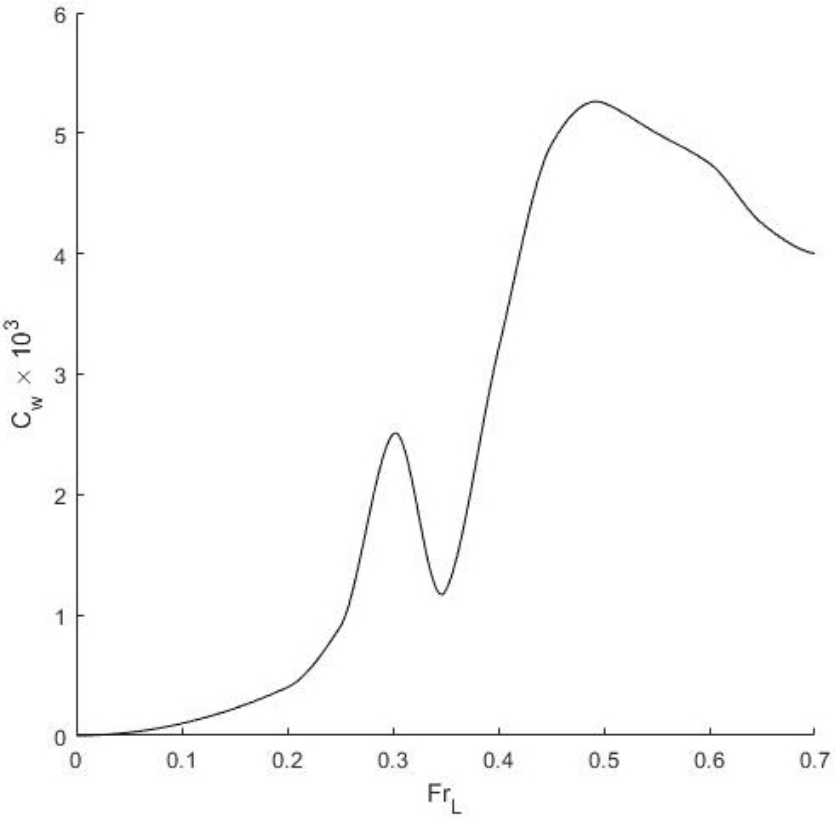

Figure 2.5: C_w for Wigley hull (rectangular midship section, adapted from [bin Tarafder et al., 2007])

with Froude number being given, in this case, by

$$\mathrm{Fr}_L = \frac{u_r}{\sqrt{gL}}$$

By implementing $C_w(\mathrm{Fr}_L)$ as a lookup function, based on the results in [bin Tarafder et al., 2007], one can fully define F_{unW}. Therefore, one can evaluate F_{un} for any given drive cycle, current conditions, and hull dimensions. Finally, if one defines τ_{nldrag} as

$$\tau_{\mathrm{nldrag}} = \begin{bmatrix} F_{un} \\ F_{vn} \\ M_{rn} \end{bmatrix} \tag{2.19}$$

then equation 1.74 can be re-written as

$$\underbrace{\mathbf{M}_{RB}\dot{\nu} + \mathbf{C}_{RB}(\nu)\nu}_{\text{rigid-body dynamics}} + \underbrace{\mathbf{M}_A\dot{\nu}_r + \mathbf{C}_A(\nu_r)\nu_r + \mathbf{D}\nu_r}_{\text{hydrodynamics}} = \underbrace{\tau_{\mathrm{control}} + \tau_{\mathrm{nldrag}} + \tau_{\mathrm{wind}}}_{\text{external forces}} \tag{2.20}$$

As a general double-check of the methodology proposed above, consider an arbitrary N43 hull sailing ahead in a straight line, at constant speed, in calm water. Using the above methodology, the following general plot was produced

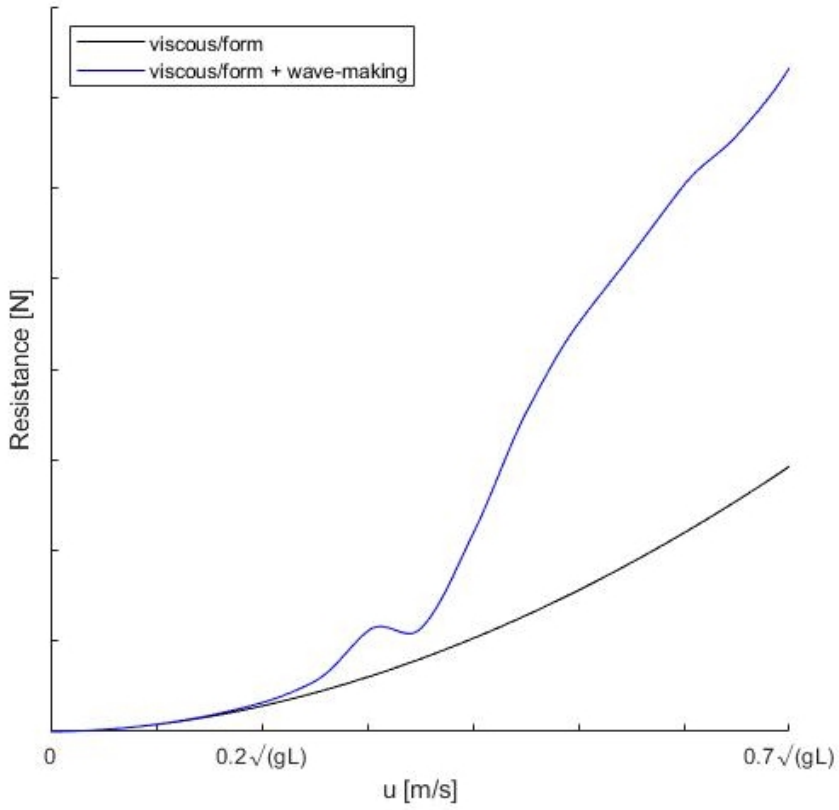

Figure 2.6: N43 hull general surge resistance (constant speed, constant course, calm water)

An inspection of figure 2.6 shows that the method above is qualitatively consistent with the literature (compare, for instance, with figure 7.6 of [USNA, 2007]). A detailed validation of the above defined drag equations, using data due to [Rahimpour and McIntyre, 2018], was also carried out as part of the case studies performed in developing this thesis; see Appendix B for results.

2.2.2 Correcting for Hull Fouling

The drag equations presented above assume a hydraulically smooth hull; in reality, however, this is rarely the case. For example, [Schultz, 2007] presents the following results derived from studying the increase in total resistance due to fouling for the case of an Oliver Hazard Perry class frigate

Table 2.1: Predictions of the change in total resistance

Description of Condition	% ΔR_T
Hydraulically smooth hull	0
Typical as applied anti-fouling coating	2 - 4
Deteriorated coating or light slime	10 - 11
Heavy slime	16 - 20
Small calcareous fouling or weed	25 - 34
Medium calcareous fouling	36 - 52
Heavy calcareous fouling	55 - 80

Therefore, one might capture the increase in total resistance due to fouling by way of scaling the $\mathbf{D}\nu_r$ and τ_{nldrag} terms of equation 2.20 in the following way

$$\underbrace{\mathbf{M}_{RB}\dot{\nu} + \mathbf{C}_{RB}(\nu)\nu}_{\text{rigid-body dynamics}} + \underbrace{\mathbf{M}_A\dot{\nu}_r + \mathbf{C}_A(\nu_r)\nu_r + C_{\text{foul,hull}}\mathbf{D}\nu_r}_{\text{hydrodynamics}} = \underbrace{\tau_{\text{control}} + C_{\text{foul,hull}}\tau_{\text{nldrag}} + \tau_{\text{wind}}}_{\text{external forces}} \tag{2.21}$$

with $C_{\text{foul,hull}} \geq 1$ being a hull fouling coefficient taking values as follows

Table 2.2: Hull fouling coefficient values

Description of Condition	$C_{\text{foul,hull}}$
Hydraulically smooth hull	1.00
Typical as applied anti-fouling coating	1.03
Deteriorated coating or light slime	1.11
Heavy slime	1.18
Small calcareous fouling or weed	1.30
Medium calcareous fouling	1.44
Heavy calcareous fouling	1.68

the values in table 2.2 being derived from the midpoints of the ranges given in table 2.1.

2.2.3 Wind Forces and Moments

The method for handling winds is essentially the same as that for handling currents. Let ν_w be given by (assuming irrotational winds)

$$\nu_w = \begin{bmatrix} u_{rw} \\ v_{rw} \\ r \end{bmatrix} = \begin{bmatrix} u - u_w \\ v - v_w \\ r \end{bmatrix} \tag{2.22}$$

If one is given wind conditions (U_w, θ_w), where U_w is wind magnitude and θ_w is wind heading, then it follows, by the same procedure applied to currents, that

$$\nu_w = \begin{bmatrix} u - U_w \cos(\theta_w - \psi) \\ v - U_w \sin(\theta_w - \psi) \\ r \end{bmatrix} \tag{2.23}$$

The forces and moments due to winds can then be expressed by [Fossen, 2011]

$$\tau_{\text{winds}} = \begin{bmatrix} F_{uw} \\ F_{vw} \\ M_{rw} \end{bmatrix} = \begin{bmatrix} -\frac{1}{2}\rho_a C_X A_{yz_w} |u_{rw} - s_y r|(u_{rw} - s_y r) \\ -\frac{1}{2}\rho_a C_Y A_{xz_w} |v_{rw} + s_x r|(v_{rw} + s_x r) \\ s_x F_{vw} - s_y F_{uw} \end{bmatrix} \tag{2.24}$$

where ρ_a is air density, A_{yz_w} is the lengthwise projected area (or sail area) of the vessel superstructure, s_y is the displacement, along y_b, from O_b to the centroid of A_{yz_w}, A_{xz_w} is the abeam projected area (or sail area) of the superstructure, and s_x is the displacement, along x_b, from O_b to the centroid of A_{xz_w}. The $C_{(\ )}$ are directional wind drag coefficients, in surge and sway, which may be tabulated as follows (underlying data from [Blendermann, 1994]) for select vessel types

Table 2.3: Directional wind drag coefficients

Vessel Type	C_X	C_Y
Car Carrier	0.60	0.95
Cargo Vessel, loaded	0.65	0.85
Cargo Vessel, container on deck	0.55	0.85
Container Ship, loaded	0.55	0.90
Destroyer	0.65	0.85
Driving Support Vessel	0.80	0.90
Drilling Vessel	0.93	1.00
Ferry	0.50	0.90
Fishing Vessel	0.70	0.95
Liquefied Natural Gas Tanker	0.65	0.70
Offshore Supply Vessel	0.80	0.90
Passenger Liner	0.40	0.90
Research Vessel	0.65	0.85
Speed Boat	0.60	0.90
Tanker, loaded	0.90	0.70
Tanker, in ballast	0.75	0.70
Tender	0.55	0.85

Thus, one can evaluate τ_{winds} for any given drive cycle, wind conditions, vessel type, and superstructure geometry.

2.2.4 Control Forces and Moments

Determining the required control forces and moments, τ_{control}, everywhere over the vessel's mission cycle is thus a matter of solving equation 2.21 for τ_{control}

$$\tau_{\text{control}} = \underbrace{\mathbf{M}_{RB}\dot{\nu} + \mathbf{C}_{RB}(\nu)\nu}_{\text{rigid-body dynamics}} + \underbrace{\mathbf{M}_A\dot{\nu}_r + \mathbf{C}_A(\nu_r)\nu_r + C_{\text{foul,hull}}\mathbf{D}\nu_r}_{\text{hydrodynamics}} - \underbrace{(C_{\text{foul,hull}}\tau_{\text{nldrag}} + \tau_{\text{wind}})}_{\text{weather forces}} \tag{2.25}$$

2.3 Modelling Propeller Dynamics

2.3.1 Linear Thrust Problem

In order to determine propeller states from τ_{control}, one must know how the fitted thrusters will work together to generate the required control forces and moments. To that end, consider an arbitrary arrangement of n thrusters set in the plane $\text{span}(x_b, y_b)$ as follows

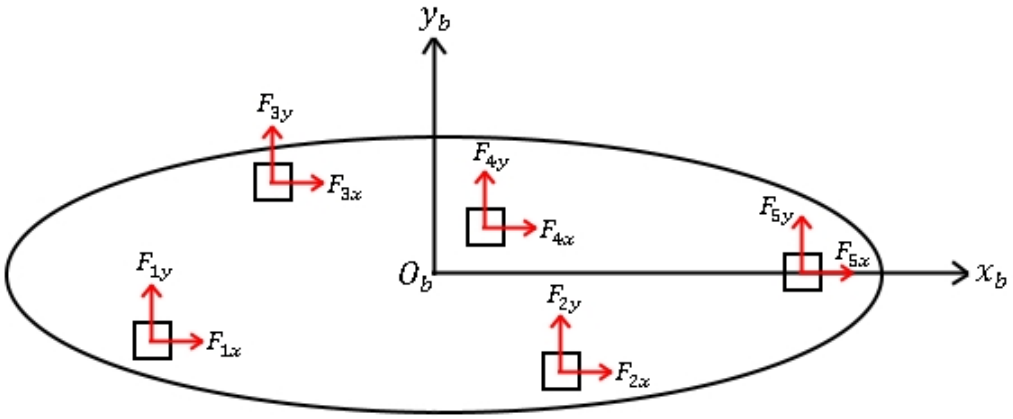

Figure 2.7: Arbitrary thruster arrangement

where each thruster, generating forces F_{ix} and F_{iy} as illustrated, is located at position (x_i, y_i). From this illustration, the following linear thrust problem can be constructed

$$\begin{bmatrix} 1 & 1 & \cdots & 1 & 0 & \cdots & 0 & 0 \\ 0 & 0 & \cdots & 0 & 1 & \cdots & 1 & 1 \\ -y_1 & -y_2 & \cdots & -y_n & x_1 & \cdots & x_{n-1} & x_n \end{bmatrix} \begin{bmatrix} F_{1x} \\ F_{2x} \\ \vdots \\ F_{nx} \\ F_{1y} \\ \vdots \\ F_{(n-1)y} \\ F_{ny} \end{bmatrix} = \tau_{\text{control}} \tag{2.26}$$

Now, for cases in which $n \geq 2$, equation 2.26 may admit an infinitude of solutions; denote the solution set to equation 2.26 by Ω. Therefore, it is physically meaningful to seek a solution

$$\vec{F}_{\text{thrust}} = \begin{bmatrix} F_{1x} \\ F_{2x} \\ \vdots \\ F_{nx} \\ F_{1y} \\ \vdots \\ F_{(n-1)y} \\ F_{ny} \end{bmatrix} \tag{2.27}$$

in Ω such that the norm of $\vec{F}_{\text{thrust}}$ is minimized. This, in essence, corresponds to the laziest possible thruster solution; a solution of interest, given the practical concerns of minimizing fuel consumption and wear on the vessel's plant. Therefore, given values for τ_{control}, one can generate corresponding minimal-norm thruster states $\vec{F}_{\text{thrust}}$.

2.3.2 Defining Thruster Magnitude and Angle

If one assumes that the thrusters have the freedom to generate thrust in any direction (in essence, they are azimuthing thrusters), then it follows that the magnitude, $T_{\text{prop},i}$, and angle (in {b}), $\theta_{\text{steer},i}$, of each thruster can be computed from $\vec{F}_{\text{thrust}}$ by way of

$$T_{\text{prop},i} = \sqrt{F_{ix}^2 + F_{iy}^2} \tag{2.28}$$

$$\theta_{\text{steer},i} = \arctan\left(\frac{F_{iy}}{F_{ix}}\right) \tag{2.29}$$

2.3.3 Defining Fluid Flow at Thruster

Consider the motion of a thruster relative to the fluid

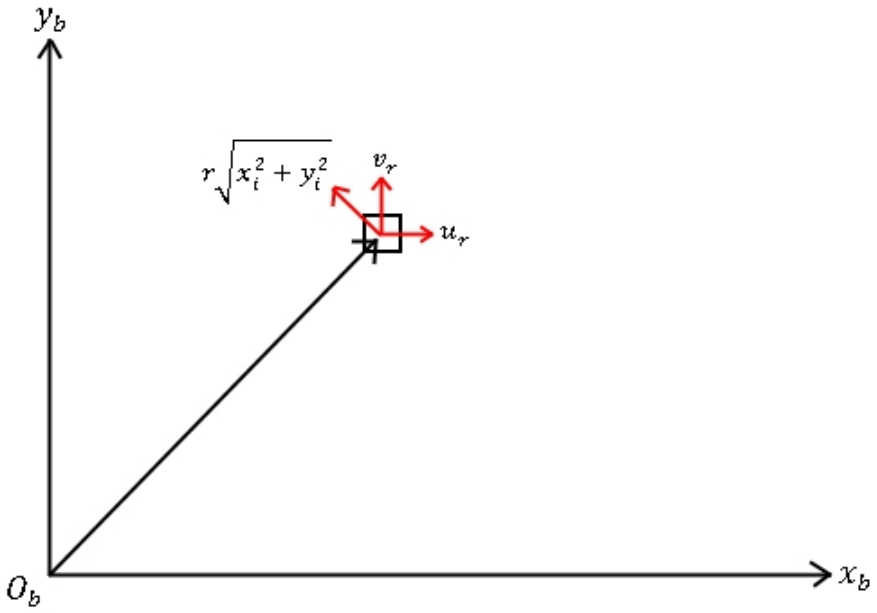

Figure 2.8: Thruster motion relative to fluid

Figure 2.8 then suggests the following expression for the velocity of the thruster relative to the fluid

$$\nu_{\text{thruster,fluid}} = \begin{bmatrix} u_r - r\sqrt{x_i^2 + y_i^2}\sin\left(\arctan\left(\frac{y_i}{x_i}\right)\right) \\ v_r + r\sqrt{x_i^2 + y_i^2}\cos\left(\arctan\left(\frac{y_i}{x_i}\right)\right) \\ 0 \end{bmatrix} \tag{2.30}$$

Relative fluid speed is therefore given by

$$V_{\text{flow}} = ||\nu_{\text{thruster,fluid}}||_2 \tag{2.31}$$

since $||\nu_{\text{thruster,fluid}}||_2 = ||\nu_{\text{fluid,thruster}}||_2$. Correcting for the fact that a thruster is operating in the vessel's wake, rather than in the free stream, can be achieved by applying a wake ratio, w, as follows

$$V_{\text{flow}} = (1 - w)||\nu_{\text{thruster,fluid}}||_2 \tag{2.32}$$

where $w = 0.1$ is a typical value in general [MIT, 2004, Andersen, 2016]. Finally, the angle between $\begin{bmatrix} F_{ix} & F_{iy} \end{bmatrix}^{\text{T}}$ and the line of fluid flow at the thruster is given by

$$\theta_{\text{flow},i} = \arccos\left(\frac{(1 - w)\nu_{\text{thruster,fluid}} \cdot \begin{bmatrix} F_{ix} & F_{iy} & 0 \end{bmatrix}^{\text{T}}}{V_{\text{flow}} T_{\text{prop},i}}\right) \tag{2.33}$$

To illustrate this, consider the following

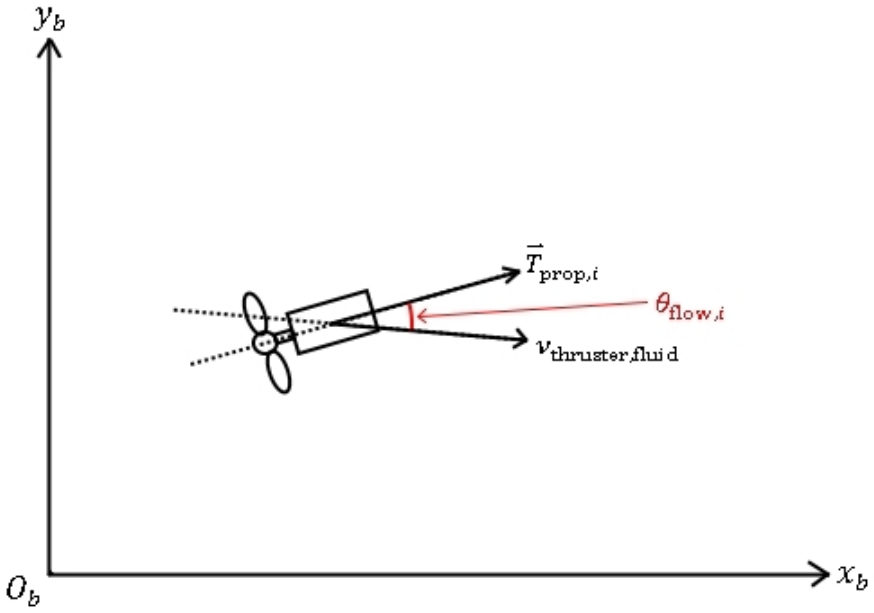

Figure 2.9: Flow angle at thruster

2.3.4 Defining Propeller Speed

Given a required thrust, $T_{\text{prop},i}$, propeller dimensions, and local conditions V_{flow} and $\theta_{\text{flow},i}$, one can determine the necessary propeller speed as follows.

Defining Base K_T Value

One can define a base value for K_T by way of equation 1.54a, given an initial guess for the propeller speed; say

$$\text{rps} = \frac{V_{\text{flow}}}{(J^*)D}$$

where J^* is the advance ratio at which the propeller obtains maximum efficiency. This value varies in pitch-diameter ratio, $\frac{P}{D}$, as follows [Techet, 2005]

Table 2.4: J^* values for the Wageningen B-series geometry

P/D	J^*
0.5	0.400
0.6	0.475
0.7	0.550
0.8	0.650
0.9	0.725
1.0	0.825
1.1	0.900
1.2	1.025
1.3	1.075
1.4	1.200

The data in table 2.4 can be visualized by referring to figure 6.3.10 of [Techet, 2005].

Correcting for Oblique Inflow

Suppose the effect of oblique inflow on K_T can be captured by way of scaling K_T as follows

$$K_T^* = C_{K_T,\theta}(J, \theta_{\text{flow},i}) K_T \tag{2.34}$$

where $C_{K_T,\theta}(\ )$ is a scalar dependent upon J and $\theta_{\text{flow},i}$. Computational results due to [Rahimpour, 2018][2] suggest the following values for $C_{K_T,\theta}(\ )$

Table 2.5: Effect of oblique inflow on K_T ($C_{K_T,\theta}(J, \theta_{\text{flow},i})$ values)

$J \setminus \theta_{\text{flow},i}$	0°	15°	30°	45°	60°	75°	90°	105°	120°	135°	150°	165°	180°
0.00000	1.00000	1.00000	1.00000	1.00000	1.00000	1.00000	1.00000	1.00000	1.00000	1.00000	1.00000	1.00000	1.00000
0.01314	1.00000	1.02818	1.02414	1.03127	1.03285	1.01975	1.03778	1.02153	1.04070	0.96719	1.01287	1.01375	0.99857
0.02629	1.00000	1.02882	1.03191	1.03586	1.04078	1.04165	1.04886	1.06198	1.07908	1.04211	0.98016	1.01532	1.01108
0.03943	1.00000	1.02934	1.03393	1.04053	1.04866	1.05855	1.06816	1.06493	1.08646	1.07682	0.99059	1.03446	1.02336
0.05257	1.00000	1.03005	1.03593	1.04538	1.05694	1.07118	1.08804	1.08900	1.03687	1.08911	0.95433	0.96145	1.05281
0.07886	1.00000	1.03170	1.04169	1.05599	1.07487	1.09504	1.11334	1.13192	1.17497	1.07887	1.09256	1.07400	1.06488
0.10515	1.00000	1.03351	1.04711	1.06740	1.09338	1.12379	1.15143	1.18170	1.17178	1.11826	1.07898	1.05945	1.07907
0.13144	1.00000	1.03550	1.05310	1.07964	1.11410	1.16407	1.17281	1.20609	1.21974	1.19278	1.26780	0.95142	1.12123
0.15772	1.00000	1.03742	1.05988	1.09312	1.13574	1.18267	1.23057	1.25505	1.31468	1.20893	1.29400	1.14723	1.14989
0.21030	1.00000	1.04258	1.07450	1.12398	1.18141	1.24579	1.30861	1.40576	1.42228	1.35057	1.44230	1.06033	1.20411
0.26287	1.00000	1.04870	1.09249	1.15557	1.23109	1.32064	1.41583	1.50817	1.62083	1.66162	1.55334	1.40576	1.27947
0.31545	1.00000	1.05623	1.11314	1.19112	1.29337	1.40801	1.53037	1.64835	1.80927	1.84466	1.70761	1.14788	1.35380
0.36802	1.00000	1.06498	1.13507	1.23433	1.36785	1.52113	1.69977	1.83961	2.04903	2.07561	1.93021	1.12821	1.34478
0.42060	1.00000	1.07422	1.15139	1.28313	1.45200	1.64614	1.83119	2.04431	2.30286	2.28485	1.86309	1.24127	1.48123
0.47317	1.00000	1.08452	1.16997	1.33506	1.55029	1.76099	2.03175	2.24847	2.53368	2.40802	1.69535	1.40654	1.13579
0.52575	1.00000	1.09767	1.19012	1.40065	1.66419	1.92195	2.26837	2.52631	2.86087	2.60383	1.90017	1.57320	1.30489
0.57832	1.00000	1.07719	1.21230	1.47120	1.79895	2.18657	2.57354	2.85803	3.26412	3.08341	2.12513	1.75754	1.53606
0.63090	1.00000	1.07682	1.24646	1.56928	1.98578	2.43962	2.94080	3.06586	3.73266	2.84952	2.43080	1.96922	1.79284
0.68347	1.00000	1.07749	1.28916	1.69661	2.23173	2.74212	3.35229	3.88008	4.00482	3.05548	2.58879	2.19925	2.10185
0.73605	1.00000	1.11072	1.38599	1.92039	2.61086	3.23531	4.08893	4.68023	5.04324	3.51792	3.13866	2.68918	2.58720
0.78862	1.00000	1.14906	1.51623	2.24342	3.18368	3.94362	4.68274	5.81404	5.93295	4.34380	3.92932	3.56597	3.25330
0.84120	1.00000	1.21870	1.74381	2.78432	4.15548	5.12407	6.74042	7.59324	7.55230	5.78111	5.23996	4.57528	4.27136
0.89377	1.00000	1.58357	2.52053	4.44221	6.90508	8.59515	10.93467	11.78011	12.15350	9.92038	8.89855	7.57851	7.23576
0.94635	1.00000	2.77917	5.34981	10.67973	17.13883	21.27308	27.94706	29.82969	30.94209	25.68558	22.50929	17.77430	19.03004

One might then assume that the above tabulated $C_{K_T,\theta}(\ )$ values are invariant with respect to propeller geometry in order to apply them in general. In such case, one can simply use table 2.5 as a general look-up table.

[2]These results are for a propeller having $D = 1.9$ m, $P = 2.275$ m, $n_{\text{blades}} = 4$, $A_b = 1.8429$ m^2, and a design speed of 309 rpm.

Correcting for Fitted Propeller Nozzle

Suppose the effect on K_T due to the presence of a propeller nozzle can be captured by way of scaling K_T^* as follows

$$K_T^{**} = C_{K_T,\text{nozzle}}(J) K_T^* \tag{2.35}$$

where $C_{K_T,\text{nozzle}}(\ )$ is a scalar dependent upon J. Computational results due to [Rahimpour, 2018], together with an application of equation 1.54a, yield the following values for $C_{K_T,\text{nozzle}}(\ )$

Table 2.6: Effect of propeller nozzle on K_T

J ($\theta_{\text{flow},i} = 0°$)	K_T **No Nozzle**	K_T **Nozzle**	$C_{K_T,\text{nozzle}}(J)$
0.00000	0.52946	0.67736	1.27933
0.01314	0.52636	0.67122	1.27521
0.02629	0.52318	0.66195	1.26524
0.03943	0.51992	0.65285	1.25566
0.05257	0.51658	0.64372	1.24612
0.07886	0.50967	0.62563	1.22751
0.10515	0.50246	0.60778	1.20962
0.13144	0.49511	0.59020	1.19206
0.15772	0.48729	0.57290	1.17568
0.21030	0.47083	0.53916	1.14512
0.26287	0.45333	0.50663	1.11756
0.31545	0.43486	0.47505	1.09242
0.36802	0.41548	0.44432	1.06941
0.42060	0.39526	0.41459	1.04892
0.47317	0.37426	0.38559	1.03027
0.52575	0.35254	0.35709	1.01291
0.57832	0.33018	0.32856	0.99511
0.63090	0.30723	0.29749	0.96829
0.68347	0.28376	0.26526	0.93481
0.73605	0.25983	0.22544	0.86763
0.78862	0.23552	0.18599	0.78969
0.84120	0.21088	0.14400	0.68285
0.89377	0.18598	0.08662	0.46574
0.94635	0.16088	0.03446	0.21419

The data in table 2.6 can be illustrated by the following figure

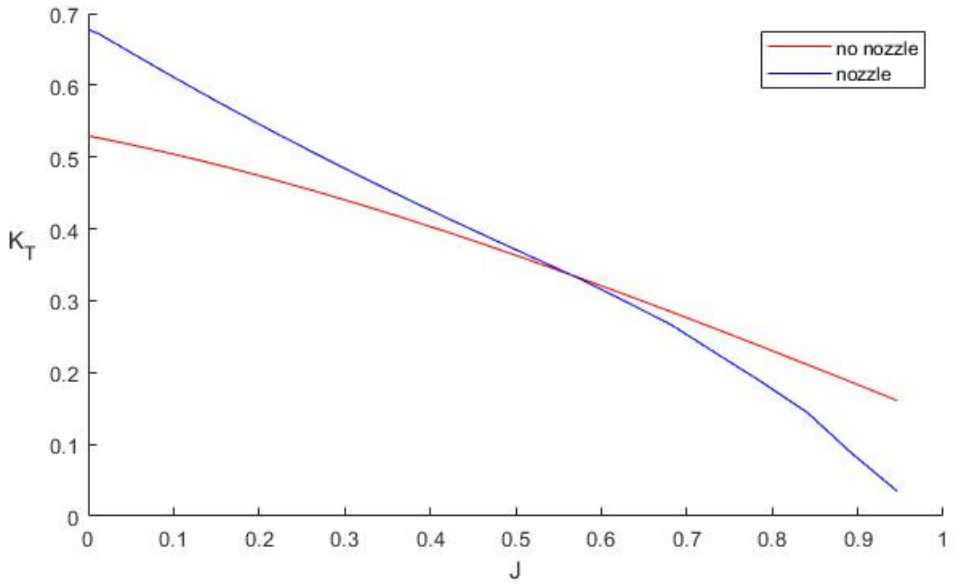

Figure 2.10: Effect of propeller nozzle on K_T

That is, K_T is higher for the nozzled propeller over a significant range of J ($J \in [0, \sim 0.55]$); the effect of this is that a nozzled propeller is more efficient at lower values of V_{flow} (see figure 2.13).[3] One might then assume that the above tabulated $C_{K_T,\text{nozzle}}(\ )$ values are invariant with respect to both $\theta_{\text{flow},i}$ and propeller geometry in order to apply them in general. In such case, one can simply use table 2.6 as a general look-up table.

[3]Assuming a fixed value for rps.

Correcting for Propeller Fouling

The effect of propeller fouling on propeller performance was investigated, using CFD, by [Owen et al., 2018][4]. A summary of results follows

Table 2.7: Effect of propeller fouling on K_T (% ΔK_T values)

Description of Condition	% ΔK_T
Hydraulically smooth propeller	0
Typical as applied anti-fouling coating	-1.16 $(J = 0.6)$ -1.65 $(J = 0.8)$ -2.58 $(J = 1.0)$ -4.52 $(J = 1.2)$
Deteriorated coating or light slime	-3.17 $(J = 0.6)$ -4.25 $(J = 0.8)$ -6.08 $(J = 1.0)$ -10.00 $(J = 1.2)$
Heavy slime	-6.15 $(J = 0.6)$ -7.97 $(J = 0.8)$ -11.74 $(J = 1.0)$ -19.37 $(J = 1.2)$
Small calcareous fouling or weed	-10.30 $(J = 0.6)$ -12.11 $(J = 0.8)$ -15.85 $(J = 1.0)$ -23.32 $(J = 1.2)$
Medium calcareous fouling	-10.89 $(J = 0.6)$ -13.05 $(J = 0.8)$ -17.27 $(J = 1.0)$ -25.50 $(J = 1.2)$
Heavy calcareous fouling	-10.89 $(J = 0.6)$ -13.05 $(J = 0.8)$ -17.27 $(J = 1.0)$ -25.50 $(J = 1.2)$

Suppose, then, that the effect on K_T due to propeller fouling can be captured by way of scaling K_T^{**} as follows

$$K_T^{***} = C_{K_T,\text{fouling}}(J) K_T^{**} \tag{2.36}$$

where $C_{K_T,\text{fouling}}(\ )$ is a scalar dependent upon J. Table 2.7 might then be transformed as follows

[4]The propeller studied had dimensions $D = 0.25$ m, $P = 0.41$ m, $n_{\text{blades}} = 5$, $A_b = 0.04$ m^2, and a design speed of 900 rpm.

Table 2.8: Effect of propeller fouling on K_T ($C_{K_T,\text{fouling}}(J)$ values)

Description of Condition	$C_{K_T,\text{fouling}}(J)$ $(\theta_{\text{flow},i} = 0°)$
Hydraulically smooth propeller	1
Typical as applied anti-fouling coating	0.9884 $(J = 0.6)$ 0.9835 $(J = 0.8)$ 0.9742 $(J = 1.0)$ 0.9548 $(J = 1.2)$
Deteriorated coating or light slime	0.9683 $(J = 0.6)$ 0.9575 $(J = 0.8)$ 0.9392 $(J = 1.0)$ 0.9000 $(J = 1.2)$
Heavy slime	0.9385 $(J = 0.6)$ 0.9203 $(J = 0.8)$ 0.8826 $(J = 1.0)$ 0.8063 $(J = 1.2)$
Small calcareous fouling or weed	0.8970 $(J = 0.6)$ 0.8789 $(J = 0.8)$ 0.8415 $(J = 1.0)$ 0.7668 $(J = 1.2)$
Medium calcareous fouling	0.8911 $(J = 0.6)$ 0.8695 $(J = 0.8)$ 0.8273 $(J = 1.0)$ 0.7450 $(J = 1.2)$
Heavy calcareous fouling	0.8911 $(J = 0.6)$ 0.8695 $(J = 0.8)$ 0.8273 $(J = 1.0)$ 0.7450 $(J = 1.2)$

The data in table 2.8 can be illustrated by the following figure

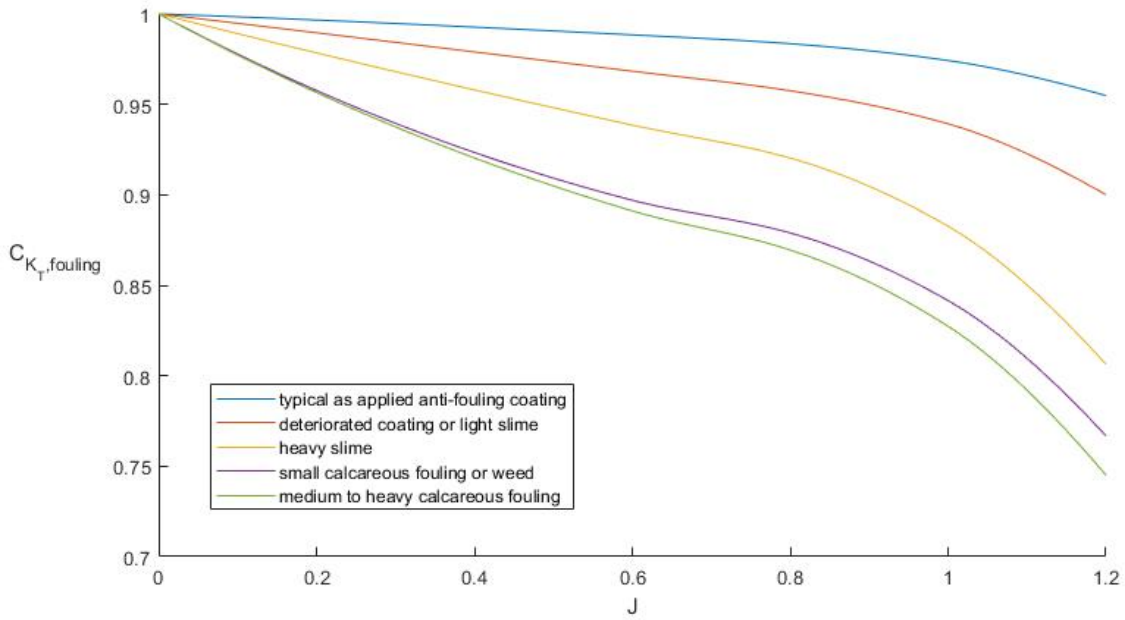

Figure 2.11: Effect of propeller fouling on $C_{K_T,\text{fouling}}$

That is, the thrust produced at a given J value generally decreases as the propeller fouling gets worse. This, in turn, results in a loss of efficiency, as one might logically expect. One might then assume that the above tabulated $C_{K_T,\text{fouling}}(\ )$ values are invariant with respect to both $\theta_{\text{flow},i}$ and propeller geometry in order to apply them in general. In such case, one can simply use table 2.8 as a general look-up table.

Solving for Propeller Speed

The final K_T value, after all relevant corrections, is thus given by

$$K_T = C_{K_T,\text{fouling}}(J) C_{K_T,\text{nozzle}}(J) C_{K_T,\theta}(J, \theta_{\text{flow},i}) f_1 \left(J, \frac{P}{D}, \frac{A_b}{A_s}, n_{\text{blades}}, \text{Re}_D \right) \tag{2.37}$$

where $f_1(\ )$ refers to equation 1.54a. Using equation 2.37, one can solve iteratively for the propeller speed necessary to deliver the required thrust, $T_{\text{prop},i}$; an algorithm for doing so follows

```
make initial guess rps = V_flow/(J_star*D);

while abs(thrust_error) > tolerance_error
    J = V_flow/(rps*D);
    Re_D = (density_fluid*V_flow*D)/viscosity_fluid;

    K_T = C_foul(J)*C_nozzle(J)*C_theta(J,theta_flow)*f1(J,P/D,A_b/A_s,n_blades,Re_D);

    thrust_gen = density_fluid*K_T*rps^2*D^4;

    thrust_error = T_prop - thrust_gen;

    drps = thrust_error/(2*density_fluid*K_T*rps*D^4);
    rps = rps + (1/2)*drps;
end
```

where the `drps` term follows from differentiating equation 1.56a while treating K_T as a constant

$$d\text{rps} = \frac{dT_{\text{prop}}}{2\rho K_T(\text{rps}) D^4} \tag{2.38}$$

2.3.5 Defining Propeller Torque

Given a propeller speed, propeller dimensions, and local conditions V_{flow} and $\theta_{\text{flow},i}$, one can determine the corresponding propeller torque as follows.

Defining Base K_Q Value

A base value for K_Q follows from equation 1.54b.

Correcting for Oblique Inflow

One can correct for effects on K_Q due to oblique inflow in the same manner by which it is accomplished for K_T. The relevant scalar values, due to [Rahimpour, 2018], are as follows

Table 2.9: Effect of oblique inflow on K_Q ($C_{K_Q,\theta}(J, \theta_{\text{flow},i})$ values)

$J \setminus \theta_{\text{flow},i}$	0°	15°	30°	45°	60°	75°	90°	105°	120°	135°	150°	165°	180°
0.00000	1.00000	1.00000	1.00000	1.00000	1.00000	1.00000	1.00000	1.00000	1.00000	1.00000	1.00000	1.00000	1.00000
0.01314	1.00000	0.99993	0.99807	0.99917	0.99894	1.00703	1.00852	1.00710	0.99292	0.96289	0.96768	1.03823	1.05686
0.02629	1.00000	1.00042	0.99859	0.99981	0.99968	1.00251	1.00574	1.00273	1.00973	0.96982	1.00125	1.03430	1.06708
0.03943	1.00000	1.00090	0.99913	1.00050	0.99759	1.00071	1.00020	0.99036	0.99432	0.97777	0.93316	1.04541	1.07845
0.05257	1.00000	1.00123	0.99819	1.00122	1.00133	1.00101	1.00963	0.99639	0.97278	0.96666	0.94852	1.24394	1.08324
0.07886	1.00000	1.00168	1.00037	1.00136	1.00272	1.00195	0.99626	0.99335	1.01538	0.92566	0.93699	1.06633	1.10363
0.10515	1.00000	1.00205	1.00090	1.00087	0.99461	0.99804	0.99437	0.99594	1.00918	0.91929	0.86608	1.44332	1.09091
0.13144	1.00000	1.00232	1.00070	1.00019	0.99373	0.99552	0.98324	1.01276	0.95841	0.91757	1.00228	1.01042	1.14207
0.15772	1.00000	1.00236	1.00064	0.99899	0.98855	0.99693	0.99414	1.00310	0.97583	0.89117	0.94345	1.11869	1.16244
0.21030	1.00000	1.00243	1.00061	0.99965	1.01447	0.99599	0.98165	1.00475	1.33278	0.89945	1.02079	1.07724	1.18806
0.26287	1.00000	1.00227	0.99929	1.00094	0.98223	1.00146	0.99858	0.99473	1.01389	0.98687	1.10105	1.24989	1.23744
0.31545	1.00000	1.00195	1.00042	1.00308	0.99747	1.00930	1.01038	1.01575	1.07243	1.02669	1.17217	1.09907	1.27445
0.36802	1.00000	1.00183	1.00253	1.00780	1.01890	1.02913	1.06113	1.08430	1.16459	1.10017	1.27395	1.15233	1.24212
0.42060	1.00000	1.00150	1.00073	1.01394	1.03147	1.06408	1.09644	1.16970	1.25742	1.17348	1.40237	1.26805	1.34109
0.47317	1.00000	1.00085	0.99842	1.01842	1.05390	1.10828	1.17770	1.25120	1.31399	1.34819	1.53040	1.43681	1.21723
0.52575	1.00000	1.00195	0.99775	1.02715	1.09818	1.17504	1.29830	1.35339	1.44382	1.49161	1.67771	1.58050	1.39864
0.57832	1.00000	0.98784	0.99689	1.03849	1.13588	1.25468	1.43154	1.47418	1.59321	1.48685	1.82557	1.69720	1.59104
0.63090	1.00000	0.98359	1.00052	1.05885	1.16078	1.34119	1.55251	1.56381	1.73224	2.01824	1.98151	1.79457	1.76750
0.68347	1.00000	0.98246	1.00784	1.08819	1.23582	1.42618	1.69579	1.85327	1.77903	2.13644	2.13718	1.97429	1.96086
0.73605	1.00000	0.99073	1.02826	1.13473	1.31670	1.56360	1.93208	2.07381	2.04997	2.35200	2.37418	2.20232	2.19796
0.78862	1.00000	0.99627	1.04902	1.19026	1.45678	1.72963	2.34938	2.31733	2.21693	2.60381	2.63819	2.57982	2.44146
0.84120	1.00000	0.99800	1.07225	1.25234	1.53074	1.91294	2.42368	2.49924	2.48002	2.92436	2.96206	2.81666	2.70352
0.89377	1.00000	1.02207	1.11891	1.35613	1.79194	2.16619	2.84133	2.72586	3.08255	3.38725	3.42204	3.31665	3.12495
0.94635	1.00000	1.03946	1.17021	1.48530	2.00594	2.41452	3.25020	3.26822	3.71032	3.95568	3.96984	3.73419	3.70792

Correcting for Fitted Propeller Nozzle

One can correct for effects on K_Q due to the presence of a propeller nozzle in the same manner by which it is accomplished for K_T. The relevant scalar values, due to [Rahimpour, 2018], are as follows

Table 2.10: Effect of propeller nozzle on K_Q

J ($\theta_{\text{flow},i} = 0°$)	$10K_Q$ **No Nozzle**	$10K_Q$ **Nozzle**	$C_{K_Q,\text{nozzle}}(J)$
0.00000	0.92715	0.67620	0.72933
0.01314	0.92213	0.67866	0.73597
0.02629	0.91700	0.67807	0.73945
0.03943	0.91176	0.67747	0.74303
0.05257	0.90642	0.67688	0.74676
0.07886	0.89542	0.67559	0.75450
0.10515	0.88400	0.67397	0.76240
0.13144	0.87157	0.67195	0.77097
0.15772	0.85843	0.66957	0.77999
0.21030	0.83143	0.66367	0.79823
0.26287	0.80328	0.65629	0.81701
0.31545	0.77390	0.64750	0.83668
0.36802	0.74327	0.63695	0.85696
0.42060	0.71138	0.62498	0.87854
0.47317	0.67829	0.61126	0.90119
0.52575	0.64400	0.59540	0.92453
0.57832	0.60858	0.57727	0.94856
0.63090	0.57204	0.55463	0.96956
0.68347	0.53445	0.52766	0.98730
0.73605	0.49583	0.49308	0.99444
0.78862	0.45626	0.45759	1.00293
0.84120	0.41576	0.42089	1.01234
0.89377	0.37439	0.37483	1.00117
0.94635	0.33219	0.32968	0.99245

The data in table 2.10 can be illustrated by the following figure

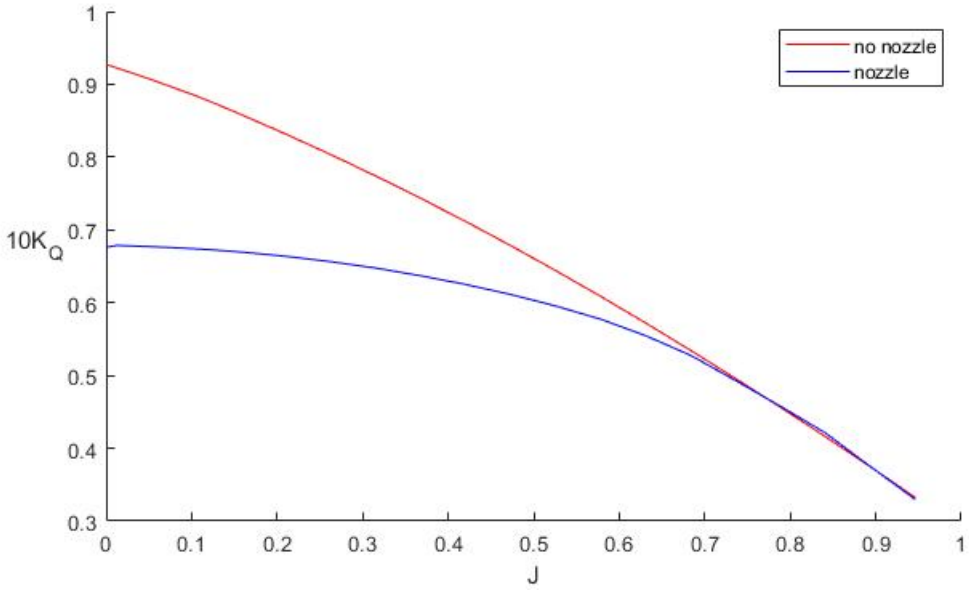

Figure 2.12: Effect of propeller nozzle on K_Q

That is, K_Q is lower for the nozzled propeller over a significant range of J ($J \in [0, \sim 0.75]$); the effect of this is that a nozzled propeller is more efficient at lower values of V_{flow}, as is illustrated by the following[5]

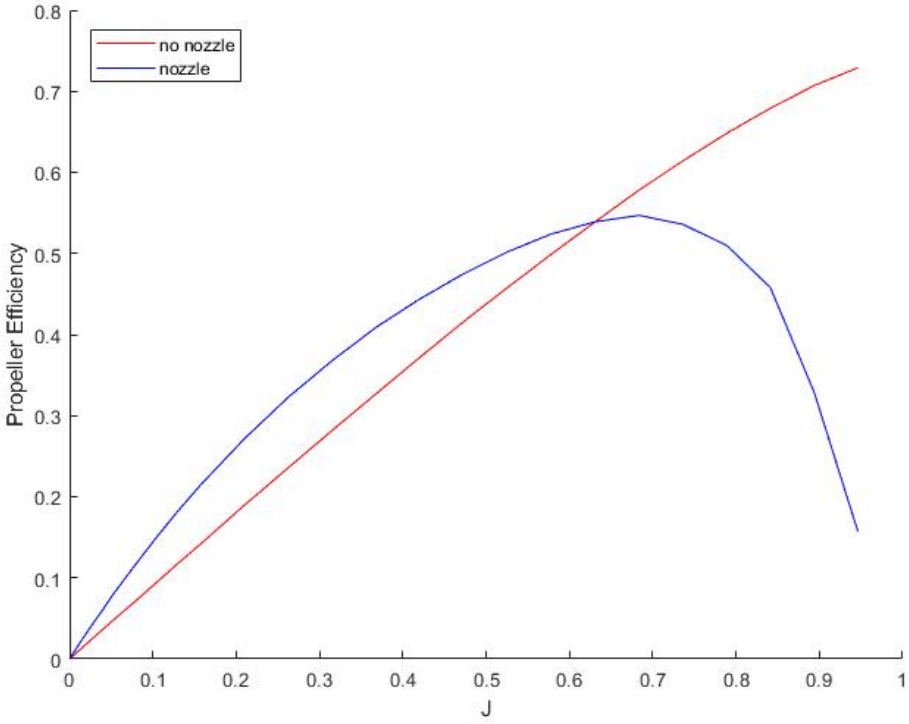

Figure 2.13: Effect of propeller nozzle on propeller efficiency

where propeller efficiency is as defined by equation 2.41.

[5]Assuming a fixed value for rps.

Correcting for Propeller Fouling

One can correct for effects on K_Q due to propeller fouling in the same manner by which it is accomplished for K_T. The relevant scalar values, due to [Owen et al., 2018], are as follows

Table 2.11: Effect of propeller fouling on K_Q ($C_{K_Q,\text{fouling}}(J)$ values)

Description of Condition	$C_{K_Q,\text{fouling}}(J)$ $(\theta_{\text{flow},i} = 0^\circ)$
Hydraulically smooth propeller	1
Typical as applied anti-fouling coating	1.0026 $(J = 0.6)$ 1.0016 $(J = 0.8)$ 0.9999 $(J = 1.0)$ 0.9959 $(J = 1.2)$
Deteriorated coating or light slime	1.0074 $(J = 0.6)$ 1.0066 $(J = 0.8)$ 1.0068 $(J = 1.0)$ 1.0036 $(J = 1.2)$
Heavy slime	1.0024 $(J = 0.6)$ 1.0037 $(J = 0.8)$ 0.9991 $(J = 1.0)$ 0.9859 $(J = 1.2)$
Small calcareous fouling or weed	1.0092 $(J = 0.6)$ 1.0246 $(J = 0.8)$ 1.0405 $(J = 1.0)$ 1.0654 $(J = 1.2)$
Medium calcareous fouling	1.0120 $(J = 0.6)$ 1.0264 $(J = 0.8)$ 1.0426 $(J = 1.0)$ 1.0690 $(J = 1.2)$
Heavy calcareous fouling	1.0120 $(J = 0.6)$ 1.0264 $(J = 0.8)$ 1.0426 $(J = 1.0)$ 1.0690 $(J = 1.2)$

The data in table 2.11 can be illustrated by the following figure

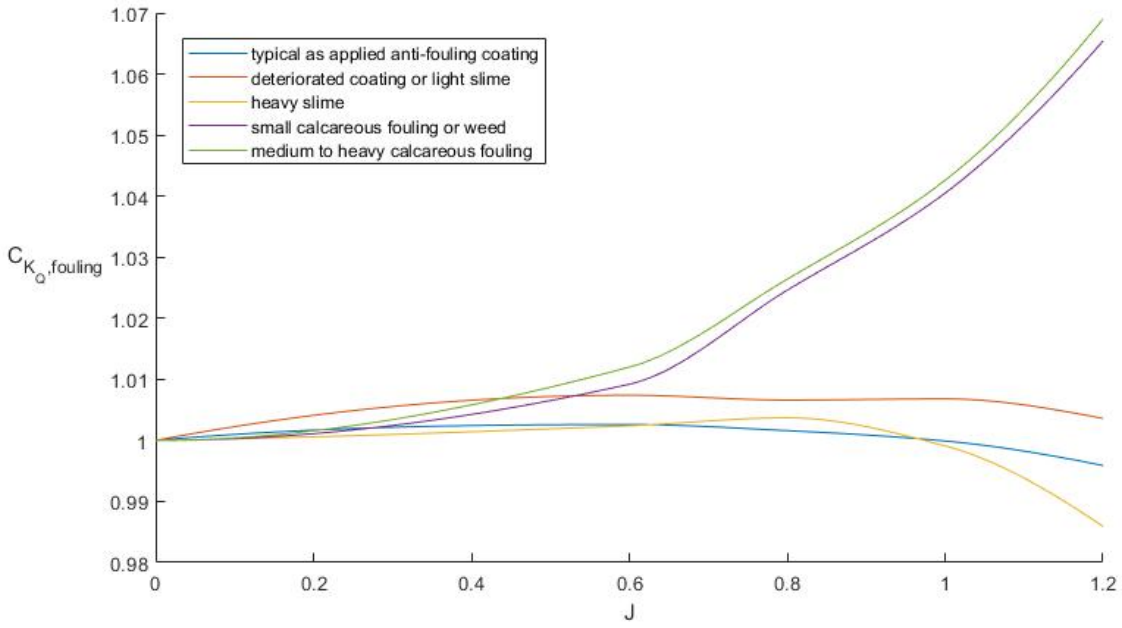

Figure 2.14: Effect of propeller fouling on $C_{K_Q,\text{fouling}}$

That is, the torque required at a given J value generally increases as the propeller fouling gets worse. This, in turn, results in a loss of efficiency, as one might logically expect.

Solving for Propeller Torque

The propeller torque corresponding to a given propeller speed, propeller dimensions, and local conditions V_{flow} and $\theta_{\text{flow},i}$ can thus be computed by way of the following

$$K_Q = C_{K_Q,\text{fouling}}(J) C_{K_Q,\text{nozzle}}(J) C_{K_Q,\theta}(J, \theta_{\text{flow},i}) f_2\left(J, \frac{P}{D}, \frac{A_b}{A_s}, n_{\text{blades}}, \text{Re}_D\right) \tag{2.39}$$

$$Q_{\text{prop}} = \rho K_Q (\text{rps})^2 D^5 \tag{2.40}$$

where $f_2(\ )$ refers to equation 1.54b.

2.3.6 Defining Propeller Design Speed

Take the propeller design speed to be that speed at which the propeller obtains maximum efficiency under V_{flow} = vessel cruise speed,[6] and $\theta_{\text{flow}} = 0°$. Since propeller efficiency, η_{prop}, is defined as [MIT, 2004]

$$\eta_{\text{prop}} = \frac{T_{\text{prop}} V_{\text{flow}}}{2\pi(\text{rps}) Q_{\text{prop}}} = \frac{K_T J}{2\pi K_Q} \tag{2.41}$$

it follows that one can determine propeller design speed by way of solving an optimization problem of the form "seek rps $\in (0, +\infty)$ such that η_{prop} is maximized". Given equations 1.55, 2.37, and 2.39, the above stated optimization problem is fully defined and thus can be solved.

[6] This will need to be either known or guessed. If one must guess, one might assume vessel cruise speed to be roughly 60% of hull speed; that is, vessel cruise speed [kts] $\cong 0.804\sqrt{L\ [\text{ft}]}$ (with speed being returned in knots, given a length, on the waterline, in feet).

2.4 Modelling Steering Dynamics

2.4.1 Governing Equation

The sum of moments acting on a rotating body obey the classical equation

$$\sum M = I\frac{d^2\theta}{dt^2} \tag{2.42}$$

where I is the mass moment of inertia of the body about the axis of rotation, and $\frac{d^2\theta}{dt^2}$ is the angular acceleration of the body. If one considers the steering gear for an azimuthing thruster, then equation 2.42 can be expanded to (assuming zero spring stiffness)

$$I_{\text{steer}}\frac{d^2\theta_{\text{steer}}}{dt^2} + b_{\text{steer}}\frac{d\theta_{\text{steer}}}{dt} = Q_{\text{steer}} \tag{2.43}$$

where I_{steer} is the mass moment of inertia of the steering gear, b_{steer} is the angular damping of the steering gear, and Q_{steer} is the moment driving the steering gear.

2.4.2 Generating Values for I_{steer} and b_{steer}

One can roughly approximate I_{steer} by way of modelling the steering gear as an assemblage of primitive geometries. For instance, consider the following assemblage

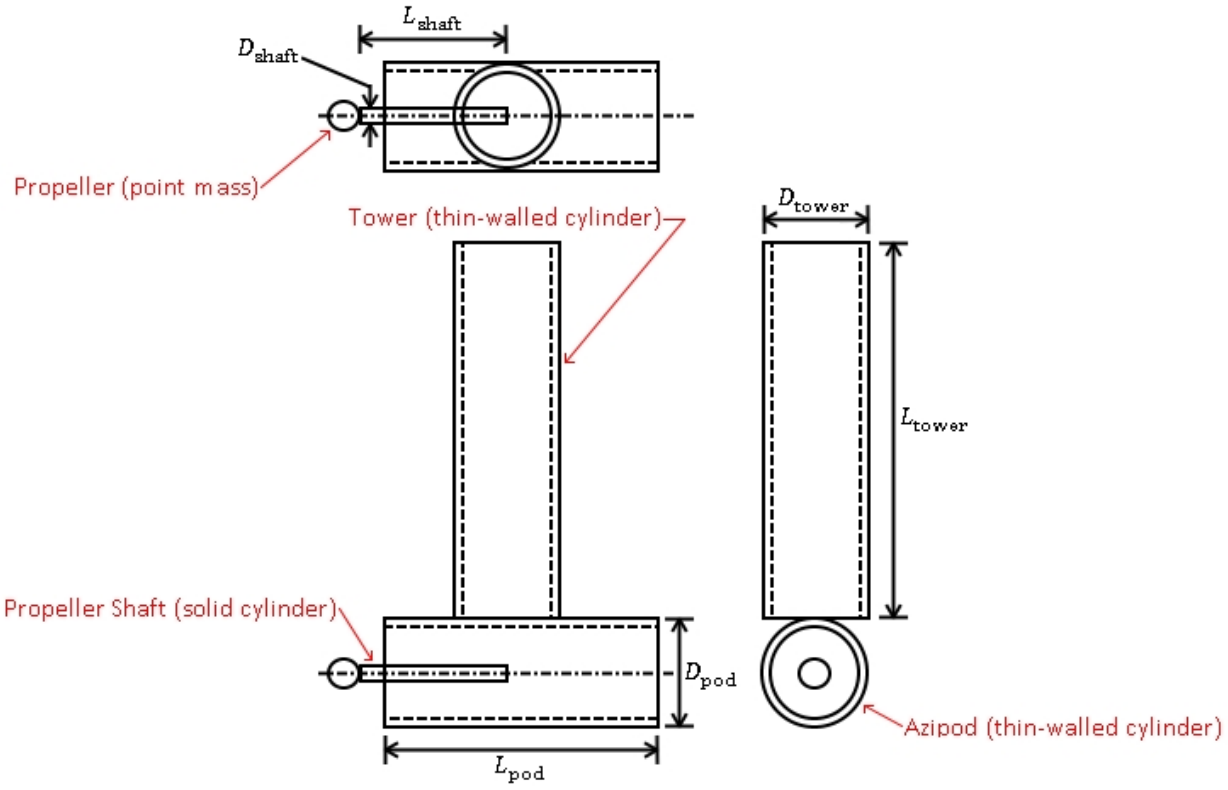

Figure 2.15: Steering gear model

The mass moments of inertia, about the tower axis, for each of the primitive geometries is then given by

$$I_{\text{prop}} = m_{\text{prop}} L_{\text{shaft}}^2 \tag{2.44a}$$

$$I_{\text{shaft}} = \frac{1}{3} m_{\text{shaft}} L_{\text{shaft}}^2 \tag{2.44b}$$

$$I_{\text{azipod}} = \frac{1}{12} m_{\text{pod}} \left(\frac{3}{2} D_{\text{pod}}^2 + L_{\text{pod}}^2 \right) \tag{2.44c}$$

$$I_{\text{tower}} = \frac{1}{4} m_{\text{tower}} D_{\text{tower}}^2 \tag{2.44d}$$

If one then assumes proportional dimensions as follows[7]

$$L_{\text{shaft}} = \frac{5}{2} P \tag{2.45a}$$

$$D_{\text{shaft}} = \frac{1}{3} D \tag{2.45b}$$

$$L_{\text{pod}} = 5P \tag{2.45c}$$

$$D_{\text{pod}} = \frac{3}{5} D \tag{2.45d}$$

$$L_{\text{tower}} = \frac{4}{5} T \tag{2.45e}$$

$$D_{\text{tower}} = \frac{3}{5} D \tag{2.45f}$$

with D and P being the diameter and pitch of the propeller, respectively, and T being the vessel draft, then equations 2.44 can be re-written as (assuming cylinder wall thicknesses of about 2% of cylinder diameter)

$$I_{\text{prop}} = \frac{25}{4} m_{\text{prop}} P^2 \tag{2.46a}$$

$$I_{\text{shaft}} \cong 0.45451 \rho D^2 P^3 \tag{2.46b}$$

$$I_{\text{azipod}} \cong \rho D^2 P (0.01385 D^2 + 0.64141 P^2) \tag{2.46c}$$

$$I_{\text{tower}} \cong 0.00443 \rho D^4 T \tag{2.46d}$$

with ρ being an appropriate material density (presumably that of steel). I_{steer} is then given by

$$I_{\text{steer}} = I_{\text{prop}} + I_{\text{shaft}} + I_{\text{azipod}} + I_{\text{tower}} \tag{2.47}$$

As for b_{steer}, one might assume that it is proportional to I_{steer} as follows (i.e., Rayleigh damping)

$$b_{\text{steer}} = \eta I_{\text{steer}} \tag{2.48}$$

Since a value for η is not immediately obvious, however, this thesis will simply assume that $\eta = 1 \, \frac{1}{\text{s}}$.

2.4.3 Generating Values for $\frac{d^2\theta_{\text{steer}}}{dt^2}$ and $\frac{d\theta_{\text{steer}}}{dt}$

Recall that, as a consequence of solving the linear thrust problem for a given τ_{control} and thruster arrangement, one generates everything needed to produce a sequence of θ_{steer} values (see equation 2.29). Therefore, one can produce corresponding values for $\frac{d\theta_{\text{steer}}}{dt}$ and $\frac{d^2\theta_{\text{steer}}}{dt^2}$ by way of the same finite differences scheme presented earlier.

[7] These choices are entirely arbitrary, as what exactly these proportions should be, in general, is not handled in this thesis.

2.4.4 Solving for Q_{steer}

With all necessary components in hand, one need only evaluate equation 2.43 in order to generate an appropriate sequence of Q_{steer} values for the steering gear of interest.

2.5 Generating Characteristic Periods

2.5.1 Generating T_{surge}

If one considers the surge-sway-yaw control of a vessel on a flat, infinite sea, then it seems reasonable to assume that the system response, to a non-oscillatory input, will be non-oscillatory in all of these degrees of freedom. Therefore, one might determine appropriate characteristic periods by way of observing the step-response of the vessel in each of these degrees of freedom and then extracting rise time (say, from 0% to 99% of steady state). Therefore, in order to determine a value for T_{surge} specifically, consider a one-dimensional problem, in surge, as follows[8]

$$(m_{\text{disp}} + A_{11})\frac{du}{dt} + C_{\text{foul,hull}}\left(\frac{3}{5}C_V + \frac{1}{2}C_w\right)\rho A_{\text{wetted}}u^2 = F_u(u) \tag{2.49}$$

with $F_u(\ )$ corresponding to the maximum sustainable thrust that the vessel can produce at speed u, and initial condition $u(0) = 0$.[9] Given appropriate values for the various scalars and coefficients present in equation 2.49, one can solve the above stated problem by way of the well-known Runge-Kutta fourth order algorithm. For example, the solution curve for an arbitrary case will look something like

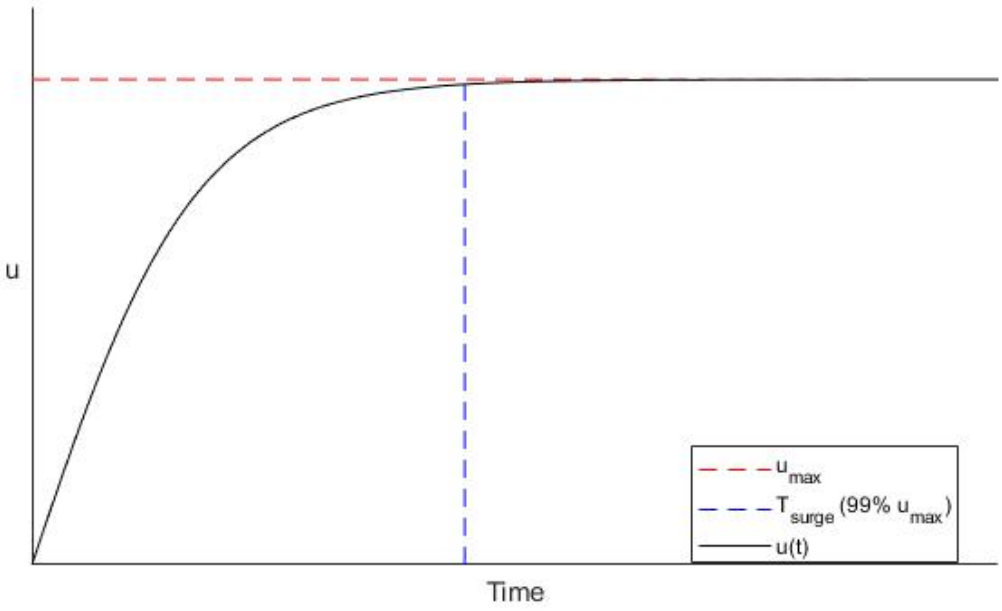

Figure 2.16: Step response in surge

from which one can extract T_{surge}.

[8] Assume no wind, waves, or current.

[9] The maximum sustainable thrust at a given speed can be determined from modelling the propeller dynamics at that speed. That is, $F_u(u) = \rho K_T(u)(\text{rps})^2 D^4$, since $K_T(\ )$ varies with u. Assume rps $\equiv$ propeller design speed.

2.5.2 Generating T_{sway}

In order to determine a value for T_{sway}, consider a one-dimensional problem, in sway, as follows

$$(m_{\text{disp}} + A_{22})\frac{dv}{dt} + C_{\text{foul,hull}}\left(\int_{-\frac{L}{2}}^{\frac{L}{2}} C_d^{2D}(x)dx\right)\frac{\rho T}{2}v^2 = F_v(v) \tag{2.50}$$

with $F_v(\ )$ corresponding to the maximum sustainable thrust that the vessel can produce at speed v, and initial condition $v(0) = 0$. From the solution to this problem, one can extract T_{sway} in the same manner as for T_{surge}.

2.5.3 Generating T_{yaw}

In order to determine a value for T_{yaw}, consider a one-dimensional problem, in yaw, as follows

$$(I_{zz}^{O_b} + A_{66})\frac{dr}{dt} + C_{\text{foul,hull}}\left(\int_{-\frac{L}{2}}^{\frac{L}{2}} C_d^{2D}(x)x^3dx\right)\frac{\rho T}{2}r^2 = M_r(r) \tag{2.51}$$

with $M_r(\ )$ corresponding to the maximum sustainable moment that the vessel can produce at speed r, and initial condition $r(0) = 0$. From the solution to this problem, one can extract T_{yaw} in the same manner as for T_{surge}.

2.5.4 Propeller and Steering Gear Periods

In order to determine appropriate propeller and steering gear periods, T_{prop} and T_{steer}, one might assume constant values for maximum sustainable propeller torque and steering moment, Q_{prop} and Q_{steer}. Assuming this, one can solve a pair of one-dimensional problems as follows.

Propeller Period

Model the propeller by way of an assemblage of primitive geometries as follows

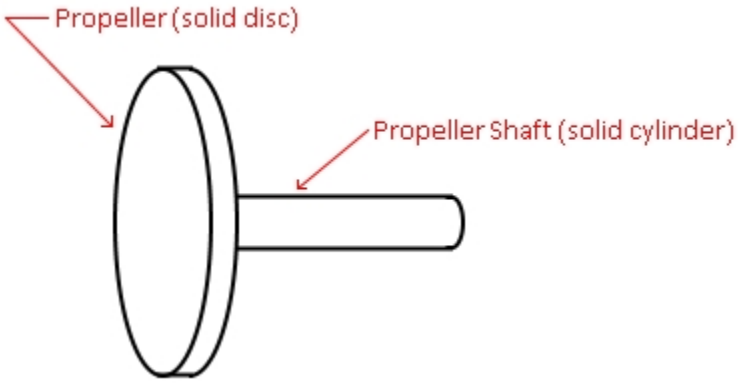

Figure 2.17: Propeller model

The total mass moment of inertia of the propeller and shaft, about the shaft axis, can thus be approximated by (taking proportional dimensions as previously)

$$I_{\text{propshaft}} \cong \frac{1}{8}m_{\text{prop}}D^2 + 0.00303\rho D^4 P \tag{2.52}$$

Using this, define the following one-dimensional problem

$$I_{\text{propshaft}} \frac{d\omega_{\text{prop}}}{dt} + \eta I_{\text{propshaft}} \omega_{\text{prop}} = Q_{\text{prop}} \tag{2.53}$$

with $\omega_{\text{prop}}(0) = 0$, and η as defined previously. The solution to equation 2.53 is given by

$$\omega_{\text{prop}}(t) = \frac{Q_{\text{prop}}}{\eta I_{\text{propshaft}}} \left(1 - e^{-\eta t}\right) \tag{2.54}$$

If one then takes T_{prop} to be the time needed to accelerate the propeller from $\omega_{\text{prop}} = 0$ to $\omega_{\text{prop}} = \omega_{\text{design}}$ (that is, the design speed of the propeller, in rad/s), then

$$T_{\text{prop}} = \frac{1}{\eta} \ln \left(\frac{Q_{\text{prop}}}{Q_{\text{prop}} - \eta I_{\text{propshaft}} \omega_{\text{design}}} \right) \tag{2.55}$$

Steering Gear Period

Consider the following one-dimensional problem

$$I_{\text{steer}} \frac{d^2\theta_{\text{steer}}}{dt^2} + \eta I_{\text{steer}} \frac{d\theta_{\text{steer}}}{dt} = Q_{\text{steer}} \tag{2.56}$$

with $\frac{d\theta_{\text{steer}}}{dt}|_{t=0} = \theta_{\text{steer}}(0) = 0$. The general solution to this problem is as follows

$$\theta_{\text{steer}} = \frac{Q_{\text{steer}}}{\eta^2 I_{\text{steer}}} (e^{-\eta t} - 1) + \frac{Q_{\text{steer}}}{\eta I_{\text{steer}}} t \tag{2.57}$$

If one then takes T_{steer} to be the time needed for the steering gear to complete one full revolution (i.e., $\theta_{\text{steer}}(T_{\text{steer}}) = 2\pi$), then

$$T_{\text{steer}} = \frac{2\pi\eta I_{\text{steer}}}{Q_{\text{steer}}} + \frac{1 + W\left(-e^{-\frac{Q_{\text{steer}} + 2\pi\eta^2 I_{\text{steer}}}{Q_{\text{steer}}}}\right)}{\eta} \tag{2.58}$$

where $W(\ )$ is the Lambert W function.

Chapter 3

Case Study Results

In this chapter, two case studies are considered as a means of validating the proposed load cycle generation process. Both cases are car-deck ferries, with case A being a more ideal candidate, given the proposed generation process, than candidate B. For each case, the hull geometry and propeller placement is introduced, along with some basic measures of the vessel. In addition, the vessel's mission is defined, in terms of distance transited, transit time, and the number of waypoints passed as input to the generation process. Results are then presented and compared to data collected either at sea or from the vessel's documentation. Finally, after both case studies have been presented, a general discussion of the results is offered.

3.1 Case Study A - Set-up

For this case study, a car-deck ferry having the following hull geometry and thruster arrangement was considered

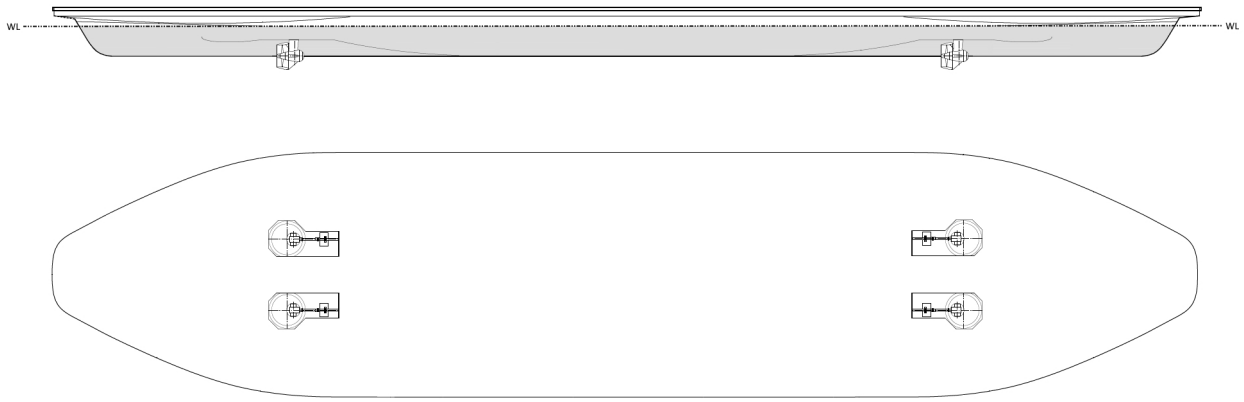

Figure 3.1: Car-deck ferry A - transverse and waterplane view

Of note in figure 3.1 is the fact that this case exhibits both forward-aft symmetry and no bulbous bow/stern. It is therefore an ideal candidate for approximation by way of the Wigley N43 geometry. In addition, this case is fitted with four, symmetrically placed, azimuthing thrusters (fitted with nozzled propellers), and so it is also an ideal candidate with respect to the methodology of propeller dynamics modelling presented previously. The basic measures of this hull are, roughly, length 105 m, beam 20 m, and draft 2.5 m. Displacement is on the order of 2500 tonnes given the loading condition considered.

A waypoint set, consisting of 16 waypoints, was generated from data collected at sea. The mission cycle considered spans 5 nautical miles in 27 minutes. Weather data was also collected from local stations in order to model currents and winds over the mission cycle. Waves were neglected, however, since this vessel operates in sheltered waters. Hull and propeller conditions were both assumed to be "deteriorated coating or light

slime". Finally, vessel specific hull and propeller parameters, derived from the vessel's drawings and manual of trim and stability, where used in all cases for which they were available.

3.2 Case Study A - Results

The process illustrated in figure 2 was implemented programmatically and then executed given the case of car-deck ferry A. Total runtime was 8 minutes 20 seconds on a 3.40 GHz quad-core processor, and thus the proposed methodology achieved a time ratio[1] of about 3.3:1 in this case.

3.2.1 Kinematics Results

A selection of the kinematics generated in this case can be plotted as as per figures 3.2 - 3.6. These kinematics were selected for presentation here because data collected at sea is available for each of them, and thus individual comparisons can be made. In addition, the latitude and longitude values are suppressed for privacy reasons.

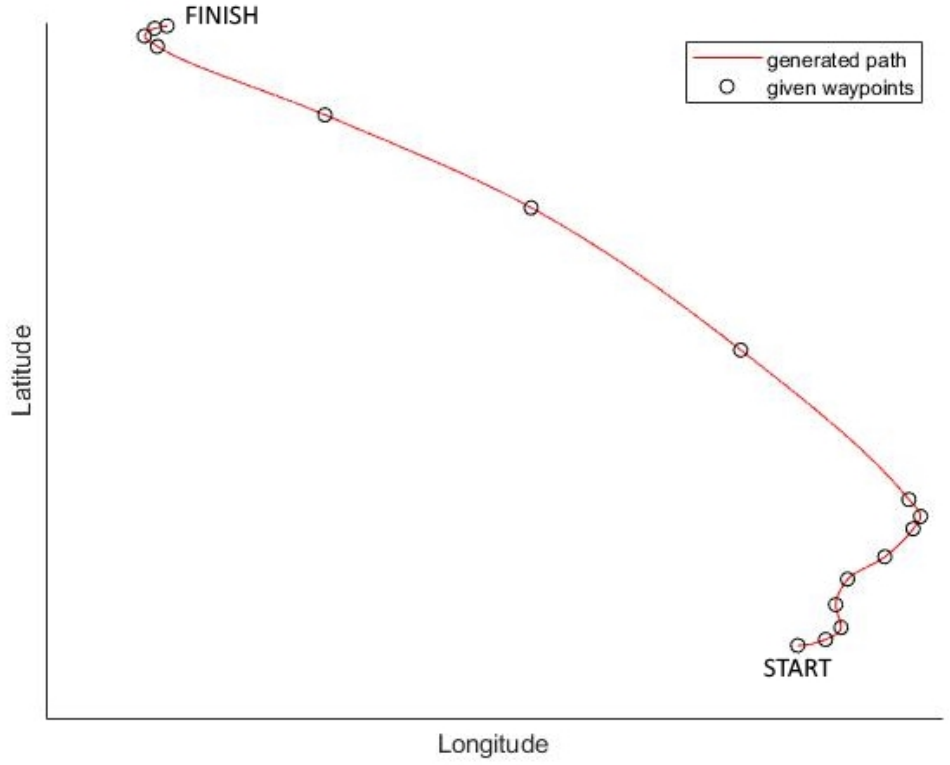

Figure 3.2: Vessel path (case A)

Figure 3.2 illustrates the mission cycle, as defined for this case (i.e., the waypoints), along with the path interpolated through the waypoints. The start and end points of the mission are defined so as to illustrate the directionality of this mission. Note that the waypoints are most densely packed in the intervals where the vessel is maneuvering in and out of dock, and least densely packed in the interval where the vessel is cruising (roughly constant heading, constant speed). This is done purposely, as the more dense the waypoints are over an interval of the mission, the smaller the timesteps used in simulating the dynamics over that interval.

[1] I.e., simulated time to execution time.

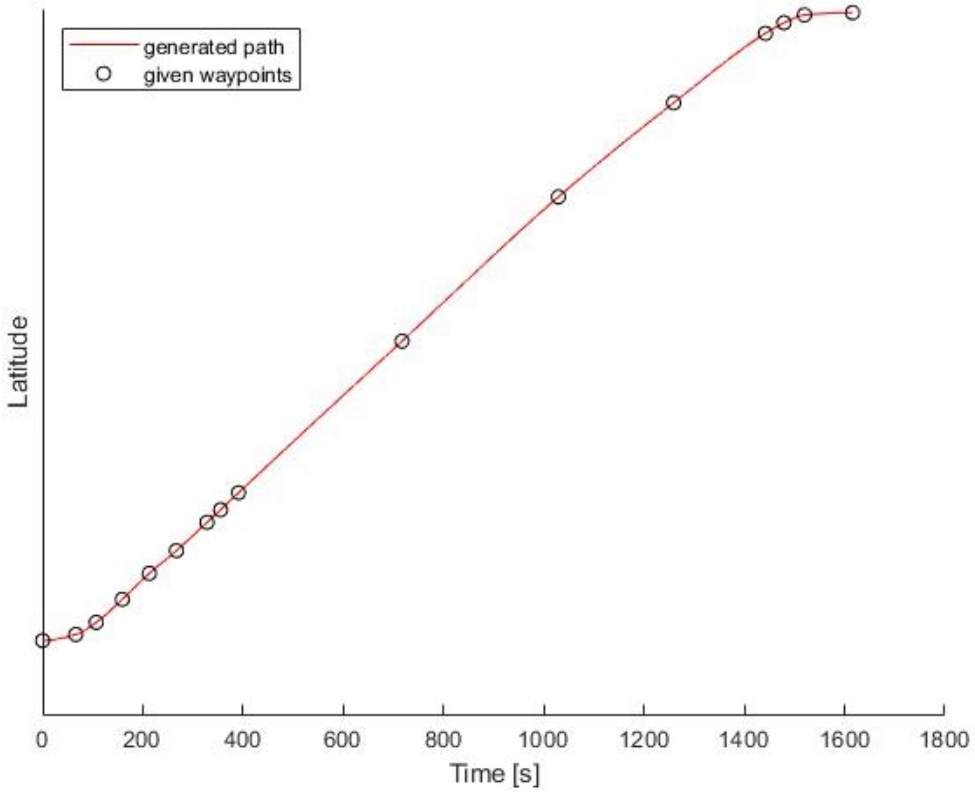

Figure 3.3: Vessel latitude vs time (case A)

Figure 3.3 also illustrates the given mission cycle and interpolated path, but instead vessel shows latitude versus time.

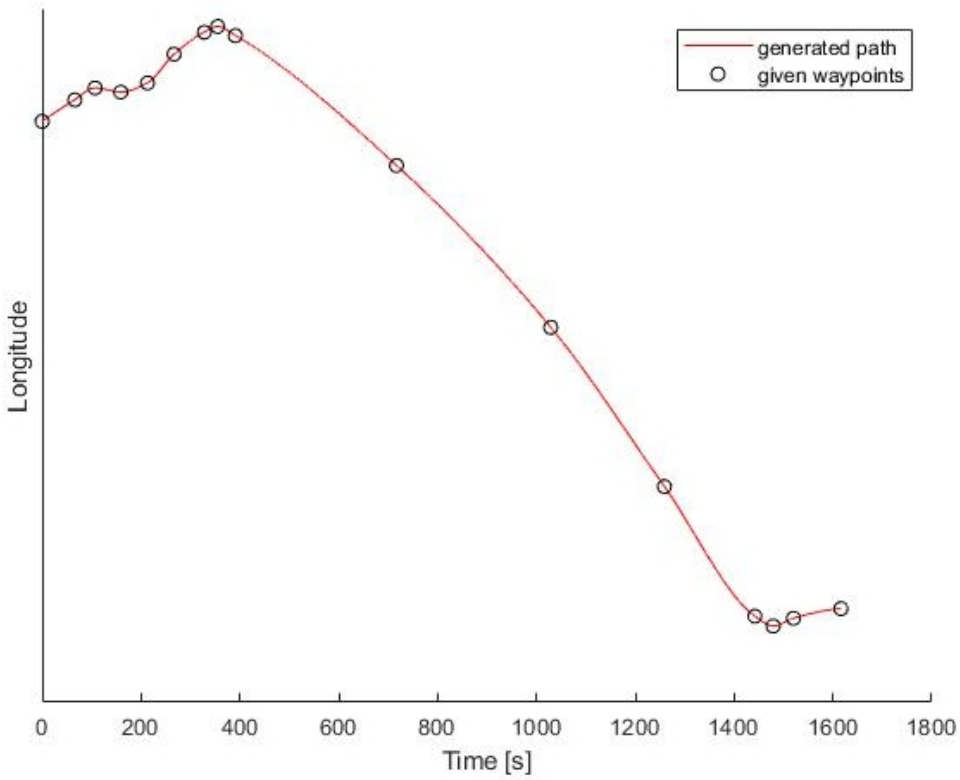

Figure 3.4: Vessel longitude vs time (case A)

Figure 3.4 also illustrates the given mission cycle and interpolated path, but instead shows vessel longitude versus time. Note also that the interval where both figures 3.3 and 3.4 exhibit a roughly constant slope is the interval over which the vessel is cruising. Since most of figures 3.3 and 3.4 exhibit a cruising state, one can conclude that this particular mission cycle is fairly static.

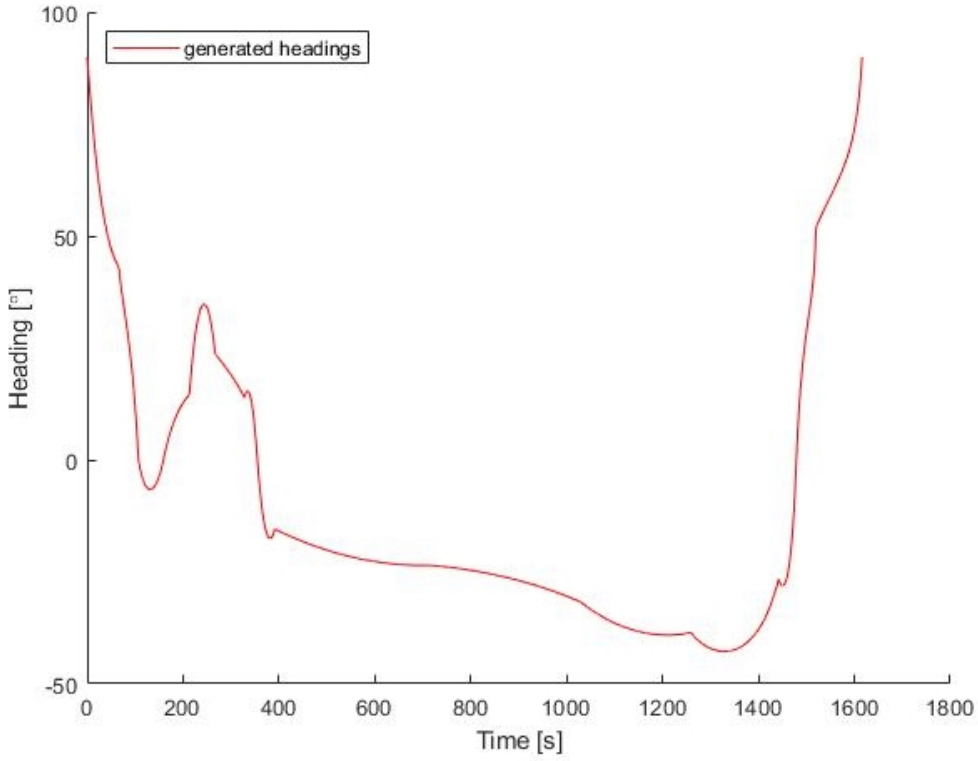

Figure 3.5: Vessel heading vs time (case A)

Figure 3.5 illustrates vessel heading versus time as generated by equation 2.2. Note that the interval over which the vessel heading is roughly constant is the interval over which the vessel is cruising.

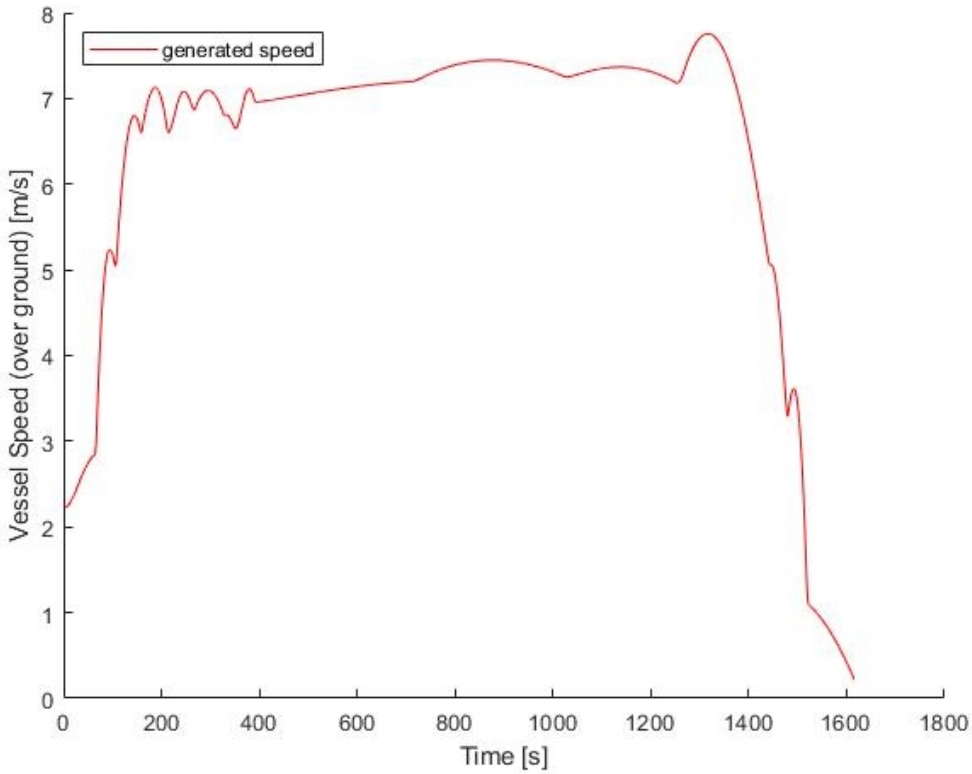

Figure 3.6: Vessel speed vs time (case A)

Figure 3.6 illustrates the vessel's speed over ground throughout the mission. For this mission, the vessel accelerates out of dock, cruises from the start point to the finish point, and then decelerates into dock.

3.2.2 Propeller Results

The propeller states generated in this case can be plotted as per figures 3.7, 3.8, and 3.9. Note that in figure 3.7, the results agree well with the propeller design speed (generated by way of section 2.3.6) while the vessel is cruising. The results in figure 3.9 are rather less than the propeller design power, but subsequent comparison will show this to be fairly accurate nonetheless. In the absence of data, however, one can immediately conclude that the results in figures 3.7 and 3.9 are feasible in that the propeller design values are nowhere exceeded.

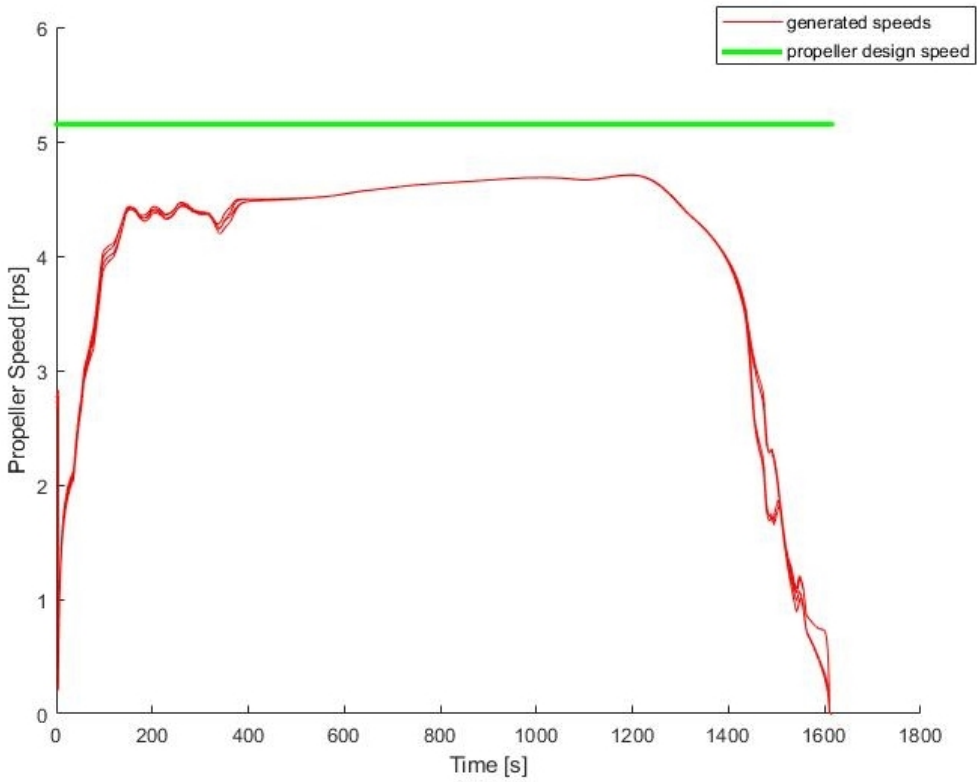

Figure 3.7: Propeller speeds vs time (case A)

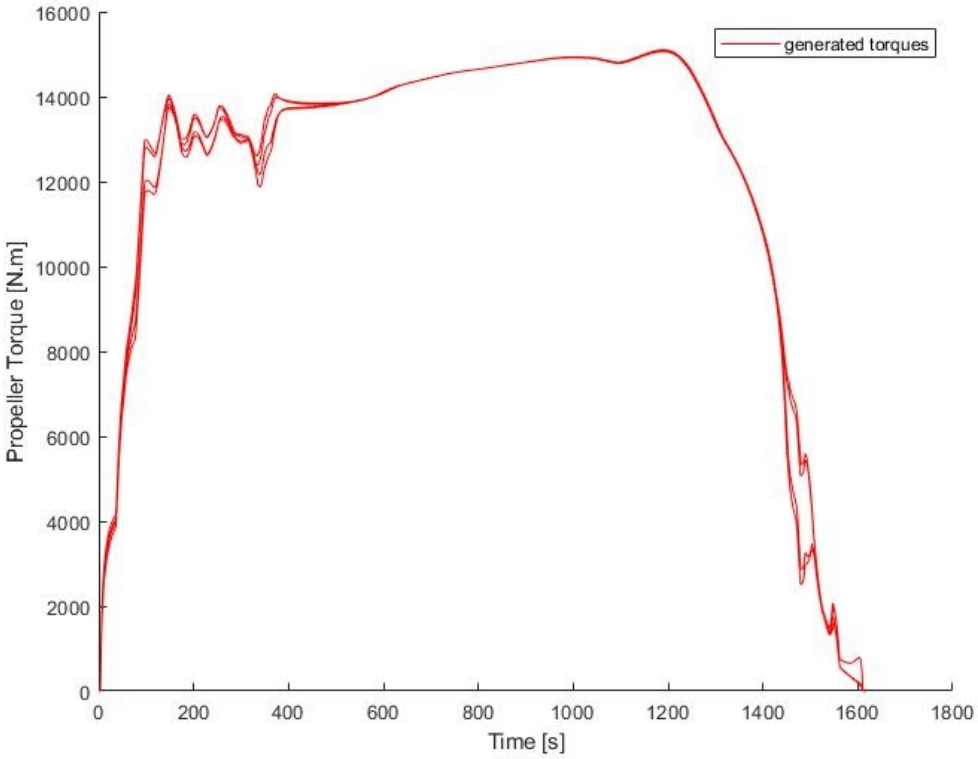

Figure 3.8: Propeller torques vs time (case A)

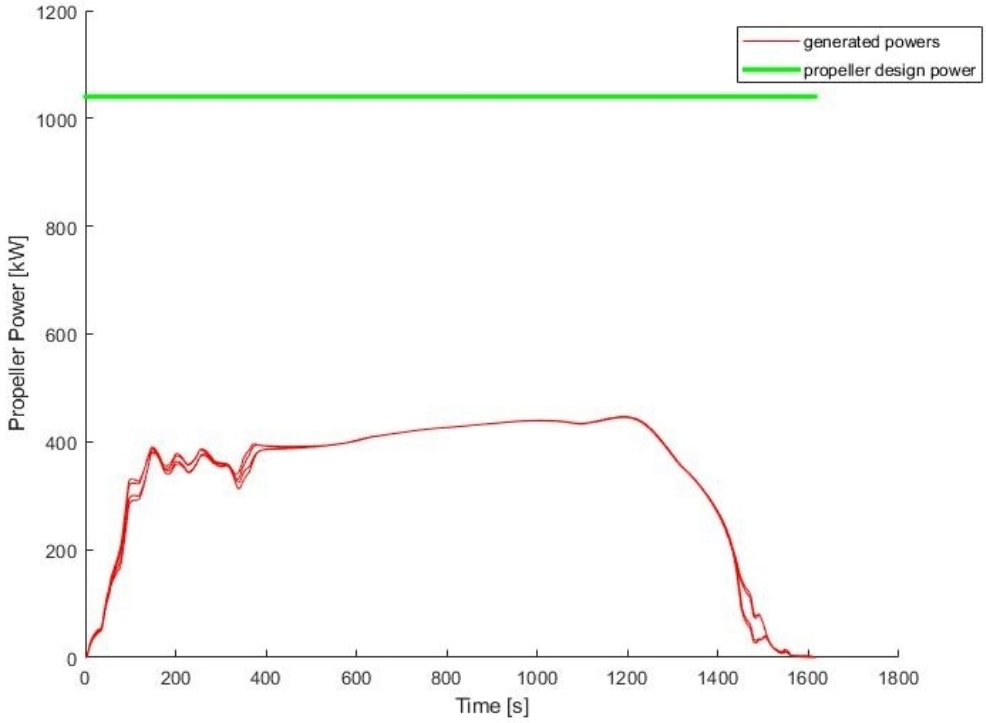

Figure 3.9: Propeller power vs time (case A)

3.2.3 Steering Gear Results

The steering gear states generated in this case can be plotted as per figures 3.10 and 3.11. Note that figure 3.10 indicates that the steering gear torques are bounded by about ±90 kN.m everywhere over the mission cycle. In addition, figure 3.11 indicates that the steering gear powers are bounded by about 85 kW everywhere over the mission cycle. It is interesting to note, then, that the steering gears fitted on the vessel considered in this case are each driven by a 75 kW hydraulic pump, according to the vessel's equipment list; this is consistent with the results illustrated in figure 3.11. No further comparison of steering gear results will be possible here, however, since operational data for the steering gear was not collected.

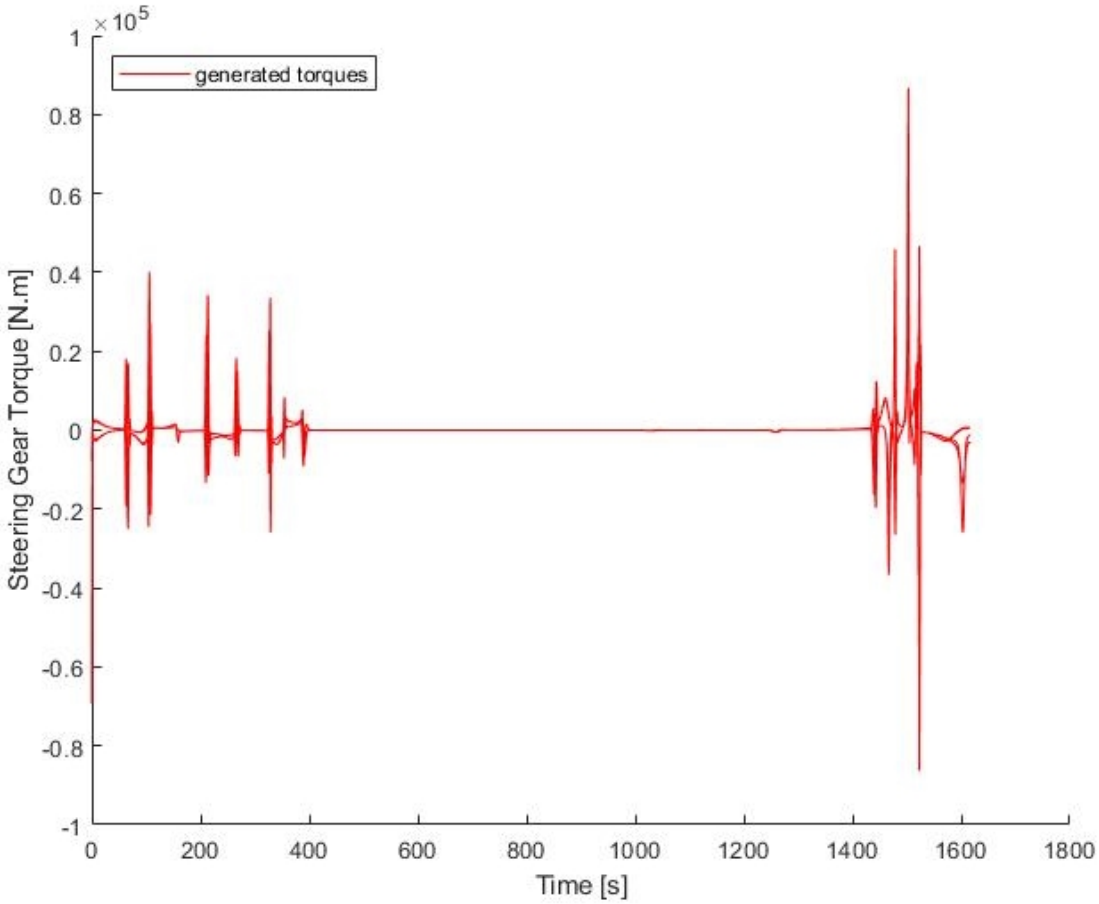

Figure 3.10: Steering gear torques vs time (case A)

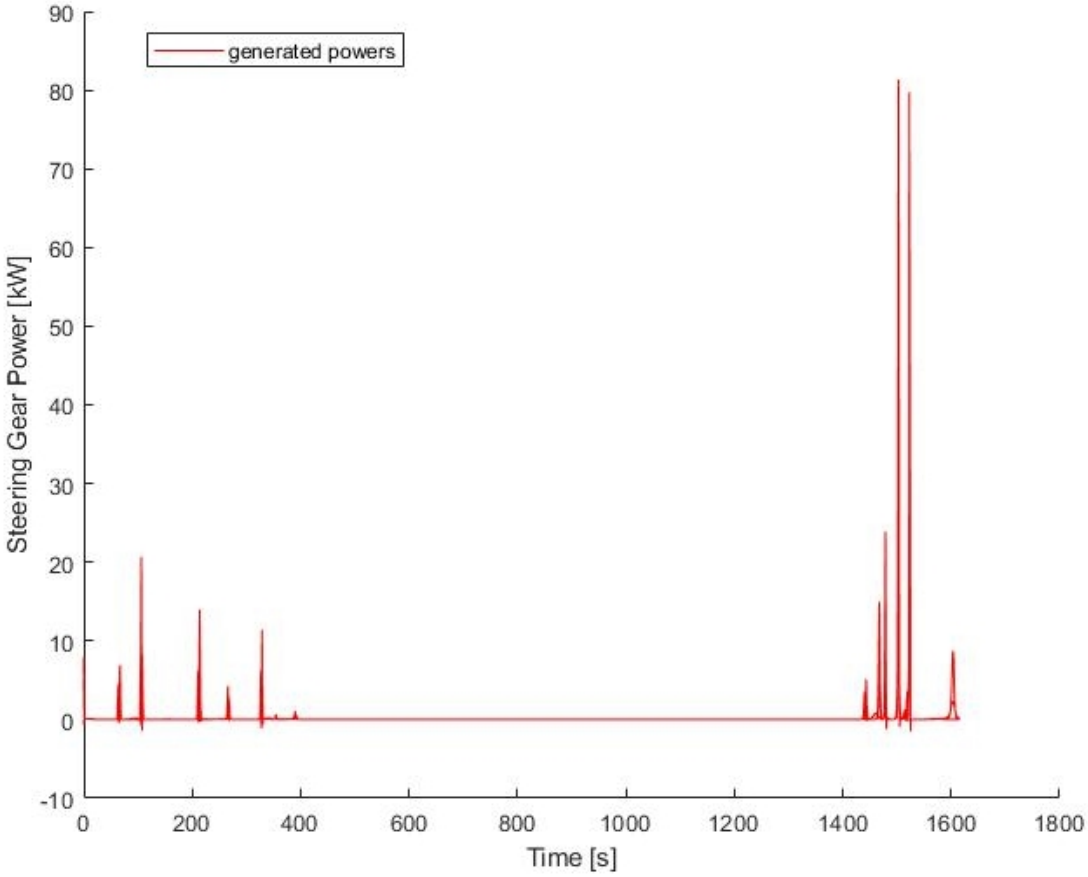

Figure 3.11: Steering gear power vs time (case A)

3.2.4 Work Done and Fuel Required

The work done by the vessel's propellers, in order to accomplish the given mission, can be determined by integrating the results of figure 3.9 over the mission cycle; this yields a result of 2185 MJ. Similarly, the work done by the vessel's steering gear can be determined by integrating the results of figure 3.11 over the mission cycle; this yields a result of 1.34 MJ. Therefore, the total work done by the vessel in accomplishing its mission is given almost entirely by the propeller work alone (as one might logically expect, given the fairly static mission cycle). From this, one can estimate a lower bound on the fuel required to accomplish the given mission. Assuming an energy density of about 38.5 MJ/L, which represents distillate fuel oil, 2185 MJ of energy is equivalent to about 60 litres of fuel. Assuming a transmission efficiency of 95% and an average engine thermal efficiency of, say, 15% over the mission cycle[2], the estimated lower bound on fuel consumption can be adjusted to about 420 litres. This is comparable to the fuel consumption recorded at sea, which for case A was about 435 litres per mission cycle. More accurate results could be obtained by mapping the propeller states to corresponding engine states and then referring to the engine's specific fuel consumption map. This approach could also yield emissions over the mission, if one has access to the engine's specific emissions map.

[2]This vessel is propelled by a classical mechanical plant.

3.3 Case Study A - Comparison

For this case, data was collected at sea for each of the kinematics and propeller results presented above [Grant and Zhu, 2017a]. A comparison between the generated results and the collected data follows.

3.3.1 Kinematics Results Comparison

A comparison of the kinematics results to the corresponding data is illustrated in figures 3.12 - 3.16, with the "cruising" partition being defined by those times for which vessel speed and heading are both relatively constant; all other times are considered "maneuvering".

As illustrated in figures 3.12, 3.13, and 3.14, the vessel path generated from the given waypoint set is in good agreement with the actual path traversed by the vessel. Figure 3.15 shows reasonably good agreement between generated vessel headings and recorded headings, with errors while cruising of about $\pm 2.5°$, and errors while maneuvering of about $\pm 10°$. These errors in heading are likely due to non-zero sway velocities (i.e., side-slipping), especially during maneuvering, which constitutes a violation of the heading tangent to path assumption made previously. In addition, the heading errors are worst towards the beginning and end of the mission (errors on the order of $\pm 35°$), where $\frac{dx_n}{dt}$ and $\frac{dy_n}{dt}$ become small thus leading to instability in the output of equation 2.2.

Figure 3.16 shows good agreement between the generated and recorded speeds of the vessel, with errors while cruising of about $\pm 1\%$ of the true speed, and errors while maneuvering of about $\pm 6\%$ of the true speed. The larger errors in maneuvering are likely due to differences in how the actual vessel is controlled versus how the simulated vessel is controlled. Recall that the control of the simulated vessel is defined by the linear thrust problem introduced previously (see, for instance, equation 2.26). This control scheme evidently differs from how the vessel is controlled in practice, especially during maneuvering. This will become even more evident once the propeller results are presented.

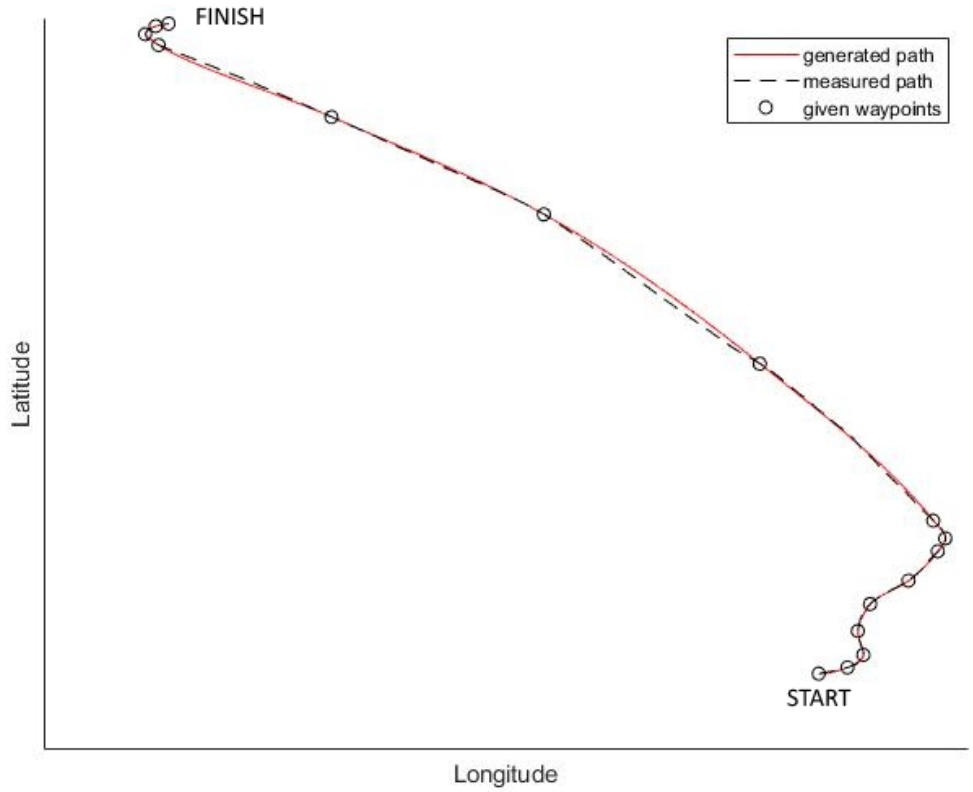

Figure 3.12: Vessel path (case A), comparison

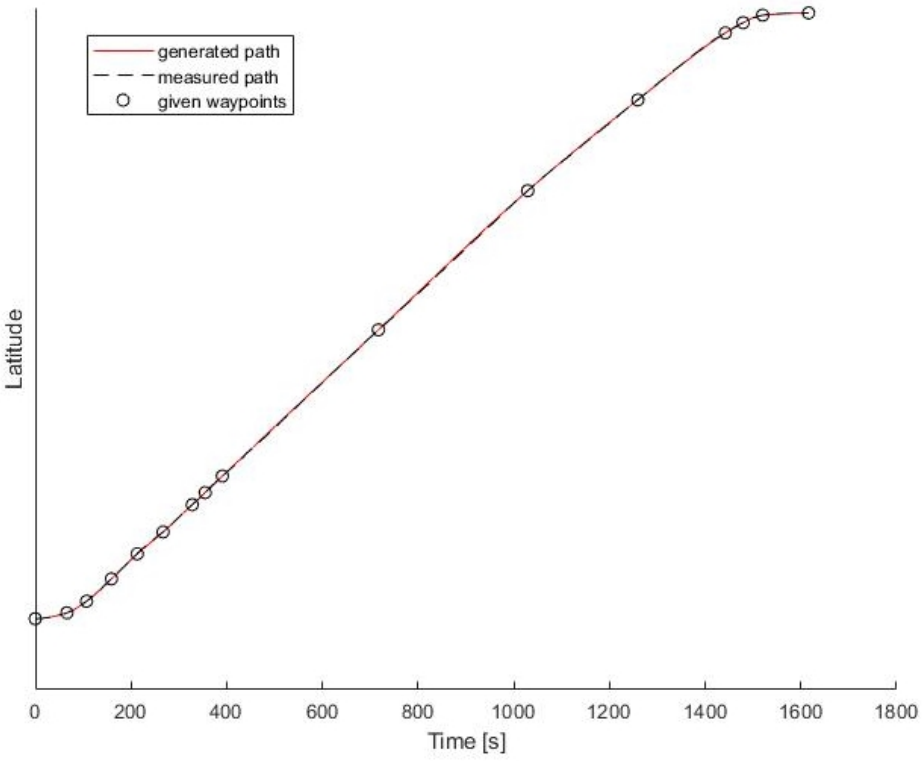

Figure 3.13: Vessel latitude vs time (case A), comparison

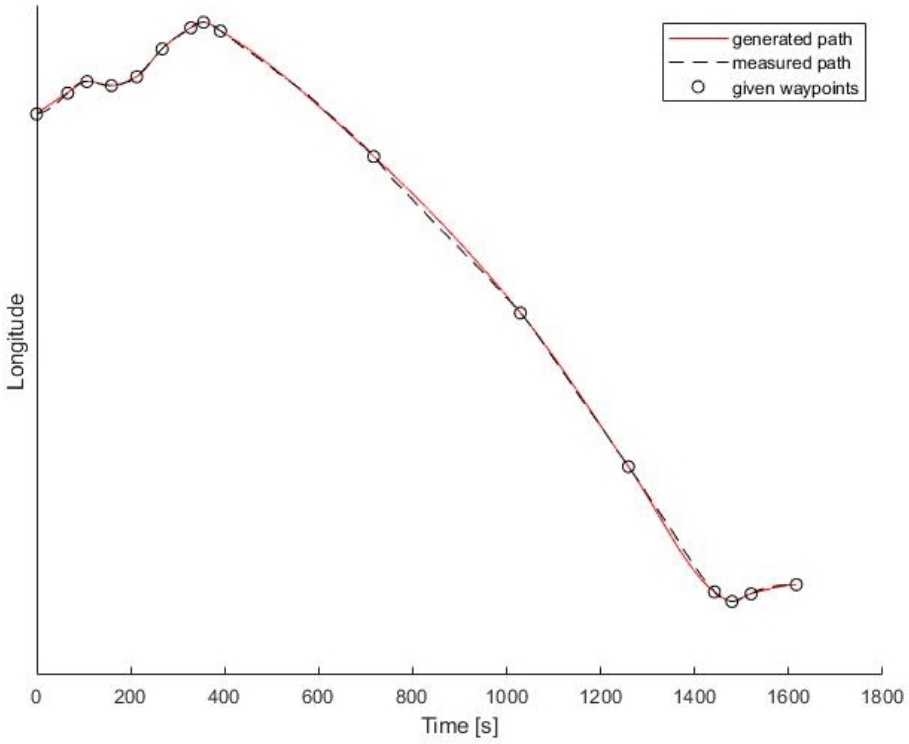

Figure 3.14: Vessel longitude vs time (case A), comparison

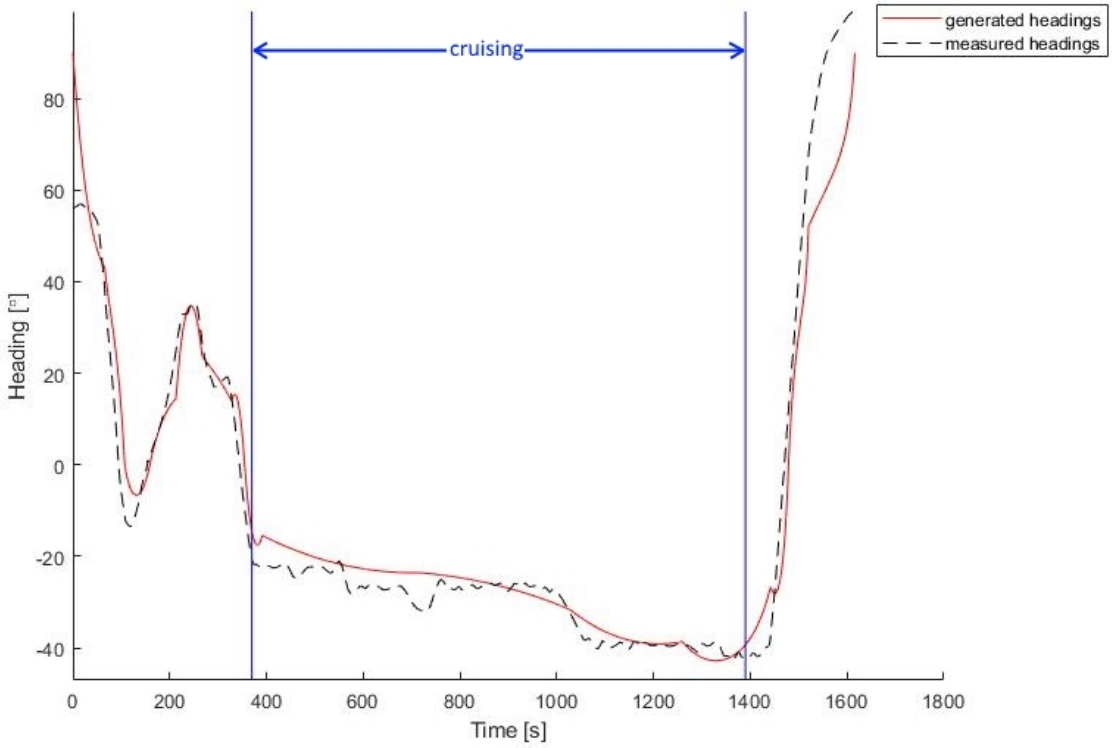

Figure 3.15: Vessel heading vs time (case A), comparison

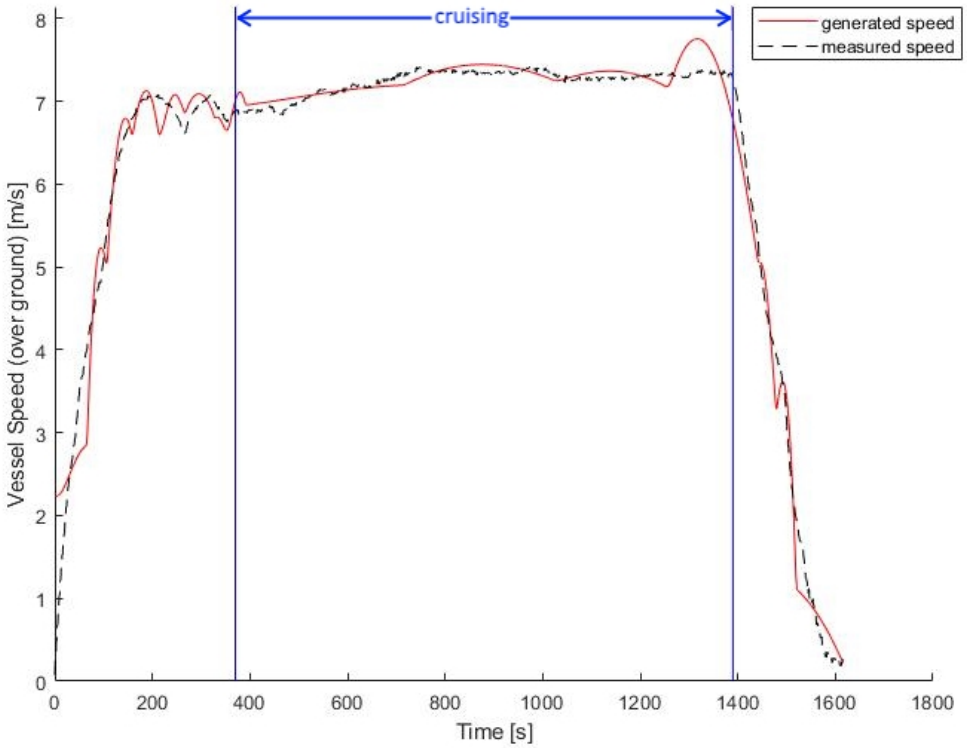

Figure 3.16: Vessel speed vs time (case A), comparison

3.3.2 Propeller Results Comparison

A comparison of the propeller results to the corresponding data is illustrated in figures 3.17, 3.18, and 3.19, which all show reasonably good agreement between the generated and recorded values for propeller dynamics. With respect to propeller speeds, the generated values are within about ±3% of the true values while cruising, and within about ±14% of the true values while maneuvering. With respect to propeller torques, the generated values are within about ±7% of the true values while cruising, and within about ±36% of the true values while maneuvering. Finally, with respect to propeller power, the generated values are within about ±10% of the true values while cruising, and within about ±42% of the true values while maneuvering. Of note, however, is that both the generated and recorded propeller powers are less than half of the propeller design power; this would indicate that a good deal of redundant power is installed in case A. This, fortunately, is normal and is due to a design practice following from the legal obligation to respond, with all haste, to marine emergencies when one is nearest and able [CSA, 2001].

Once again, the generated results are quite good while cruising, but not as good while maneuvering. The larger errors while maneuvering can, as before, likely be attributed to differences in how the actual vessel is controlled versus how the simulated vessel is controlled. For example, consider figure 3.17. The recorded propeller speeds show the propellers mostly operating at a few discrete speeds, with changes occurring only to move from one discrete speed to another.[3] In contrast, the generated propeller speeds show the propellers changing speed smoothly and continuously throughout the mission cycle. The same control differences present in figures 3.18 and 3.19 as well. It is therefore important to distinguish between the recorded values, which represent how the vessel is actually controlled, and the generated values, which represent how the vessel should be controlled according to the linear thrust problem.

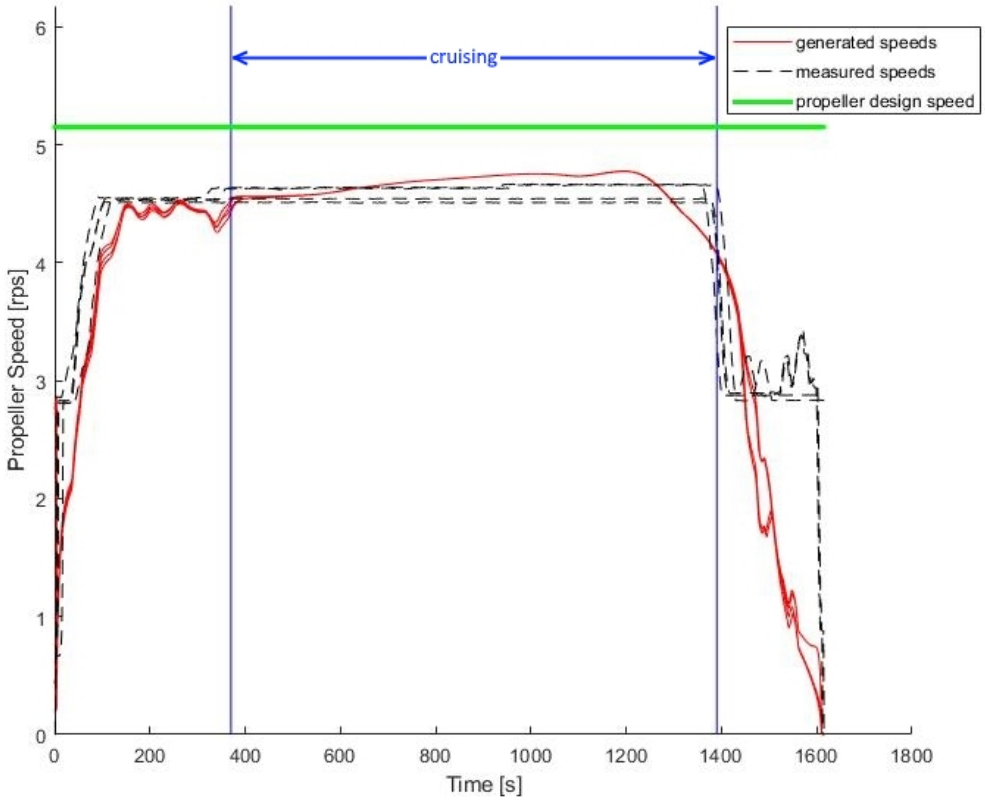

Figure 3.17: Propeller speeds vs time (case A), comparison

[3]The only exception to this behaviour is toward the end of the mission cycle, where the propellers are more finely controlled during docking.

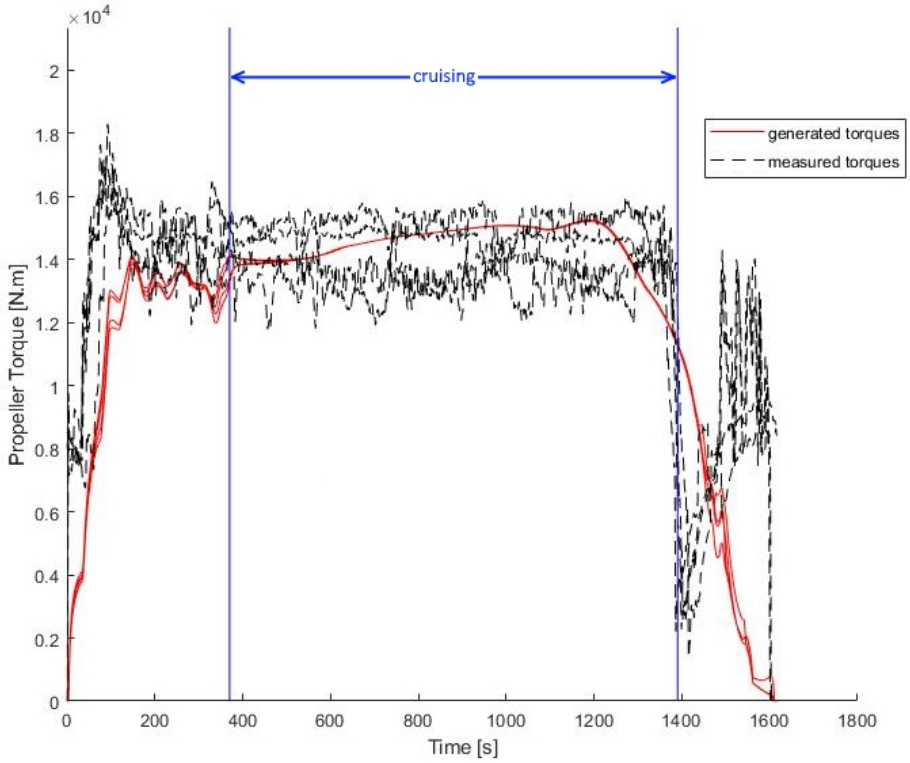

Figure 3.18: Propeller torques vs time (case A), comparison

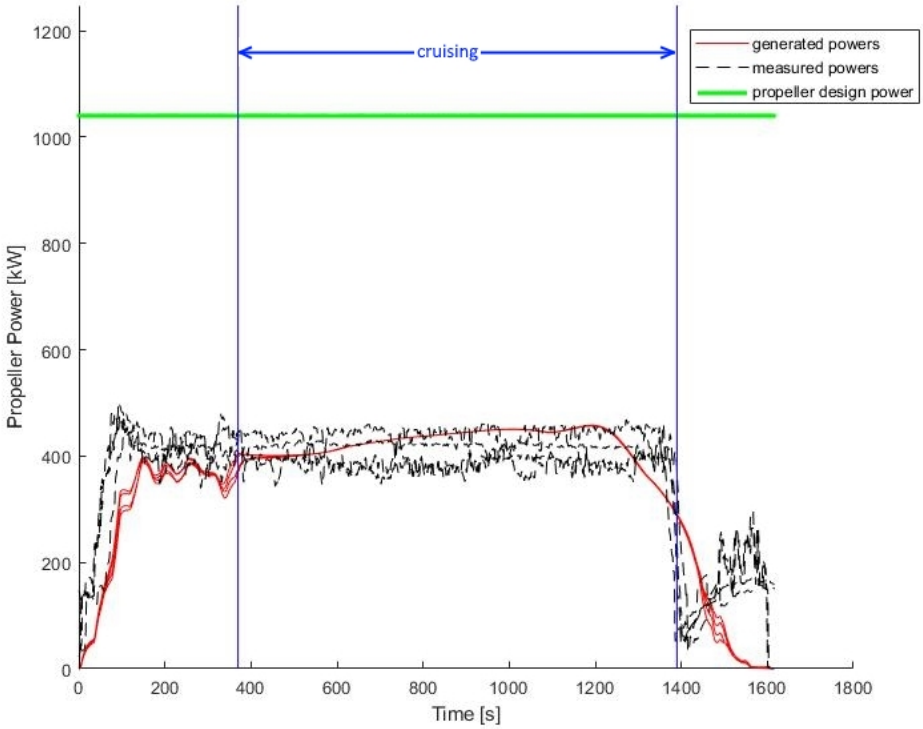

Figure 3.19: Propeller power vs time (case A), comparison

3.4 Case Study B - Set-up

For this case study, a car-deck ferry having the following hull geometry and thruster arrangement was considered

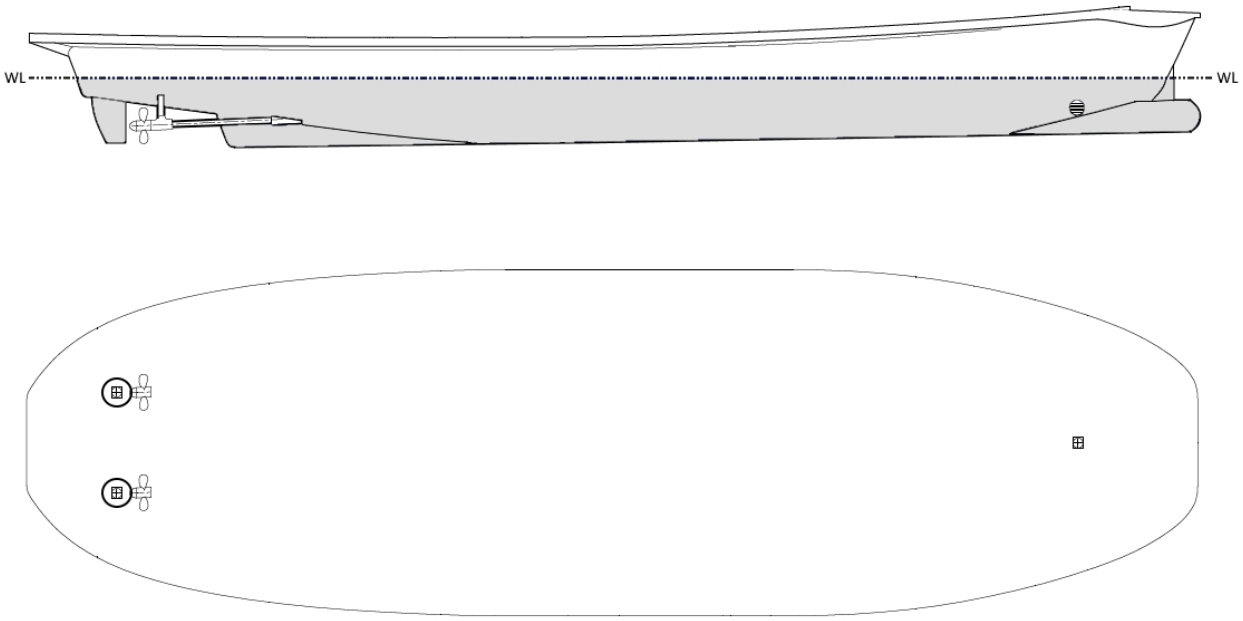

Figure 3.20: Car-deck ferry B - transverse and waterplane view

Of note in figure 3.20 is the fact that this case does not exhibit forward-aft symmetry and is fitted with a bulbous bow. In addition, the vessel is propelled by two fixed propellers (no nozzles fitted), with steering achieved by way of rudders and a bow-thruster (or tunnel thruster). Therefore, this particular case is not as well suited to the methodology presented in this thesis as is case A. Still, this case is of interest as it more closely resembles the general architecture of large merchant vessels, such as tankers and carriers, than does case A. The basic measures of this hull are, roughly, length 45 m, beam 15 m, and draft 2.6 m. Displacement is on the order of 750 tonnes given the loading condition considered.

As an experiment, it was decided to modify the vessel under consideration from that illustrated in figure 3.20 to the following

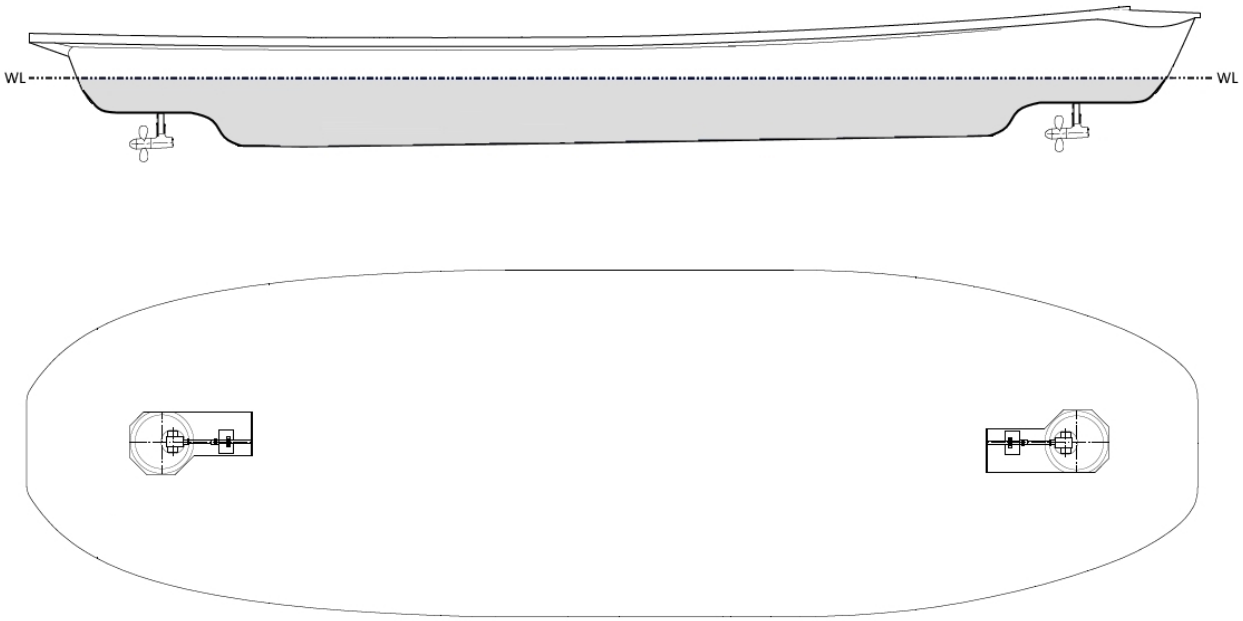

Figure 3.21: Car-deck ferry B, modified - transverse and waterplane view

That is, replace the propulsion and steering equipment with two, centreline, azimuthing thrusters (each fitted with the same propeller as in figure 3.20), and then modify the submerged hull geometry so as to eliminate the bulbous bow and accommodate the thrusters such that they are placed in the vicinity of the true propeller and bow-thruster positions. Figure 3.21 thus illustrates a vessel better suited to the methodology presented in this thesis. The question, then, is how well will this modified vessel represent the true vessel when simulated?

A waypoint set, consisting of 14 waypoints, was generated from data collected at sea. The mission cycle considered spans 6.2 nautical miles in 45 minutes. Weather data was also collected from local stations in order to model currents and winds over the mission cycle. Waves were neglected, however, since this vessel operates in sheltered waters. Hull and propeller conditions were both assumed to be "deteriorated coating or light slime". Finally, vessel specific hull and propeller parameters, derived from the vessel's drawings and manual of trim and stability, where used in all cases for which they were available.

3.5 Case Study B - Results

The process illustrated in figure 2 was executed given the case of car-deck ferry B (modified). Total runtime was 3 minutes 30 seconds on a 3.40 GHz quad-core processor, and thus the proposed methodology achieved a time ratio of about 12.8:1 in this case.

3.5.1 Kinematics Results

A selection of the kinematics generated in this case can be plotted as per figures 3.22 - 3.26. These kinematics were selected for presentation here because data collected at sea is available for each of them, and thus individual comparisons can be made. Again, the latitude and longitude values are suppressed for privacy reasons.

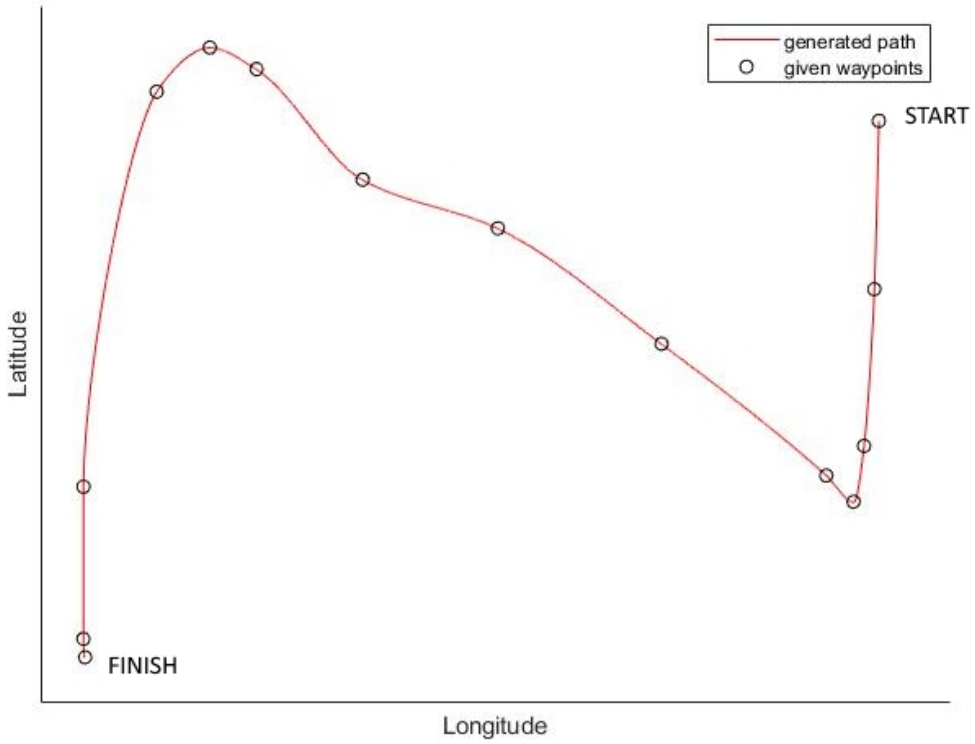

Figure 3.22: Vessel path (case B)

Figure 3.22 illustrates the mission cycle, as defined for this case (i.e., the waypoints), along with the path interpolated through the waypoints. The start and end points of the mission are defined so as to illustrate the directionality of this mission. One feature of this case that makes it different from case A is that, instead of being partitioned into one cruising interval and two maneuvering intervals, this case can be partitioned into two cruising intervals separated by maneuvering intervals.

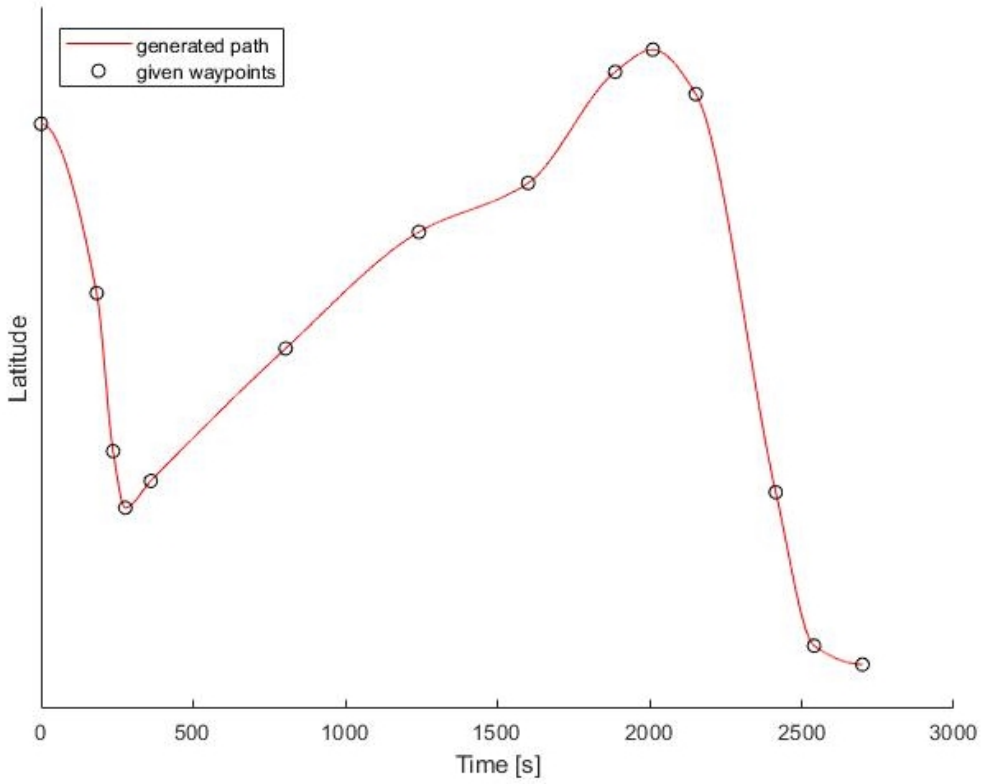

Figure 3.23: Vessel latitude vs time (case B)

Figure 3.23 also illustrates the given mission cycle and interpolated path, but instead shows vessel latitude versus time.

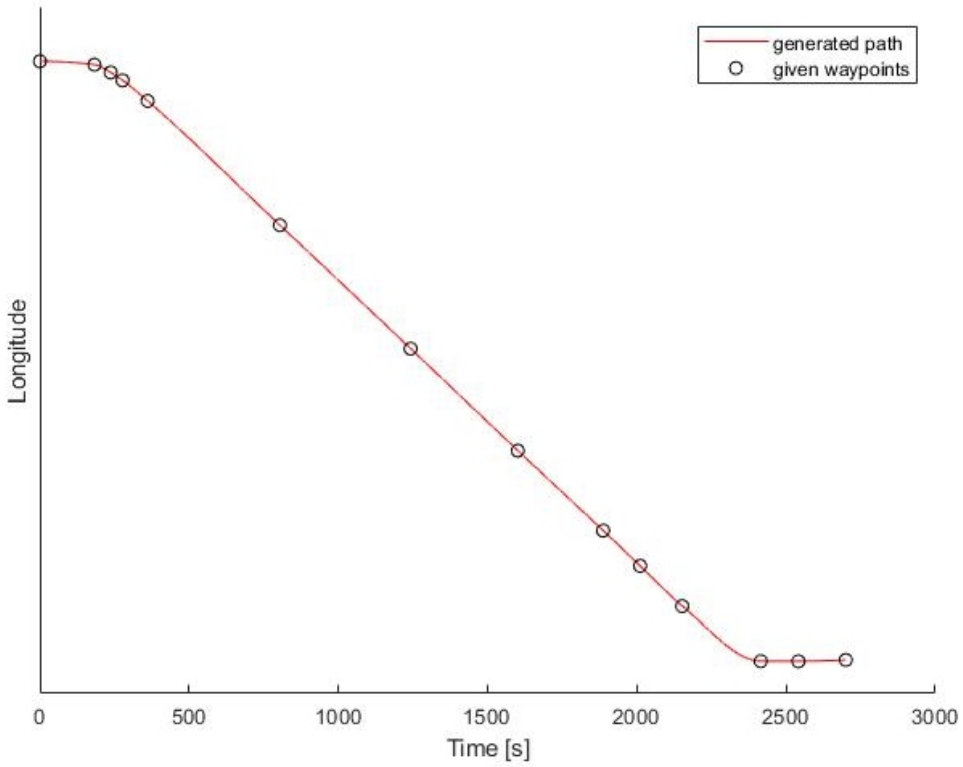

Figure 3.24: Vessel longitude vs time (case B)

Figure 3.24 also illustrates the given mission cycle and interpolated path, but instead shows vessel longitude versus time. Figures 3.23 and 3.24 together also illustrate the maneuvering-cruising-maneuvering-cruising-maneuvering structure present in the mission cycle for this case. Like case A, however, the vessel spends most of the mission in a cruising state, so case B is also fairly static.

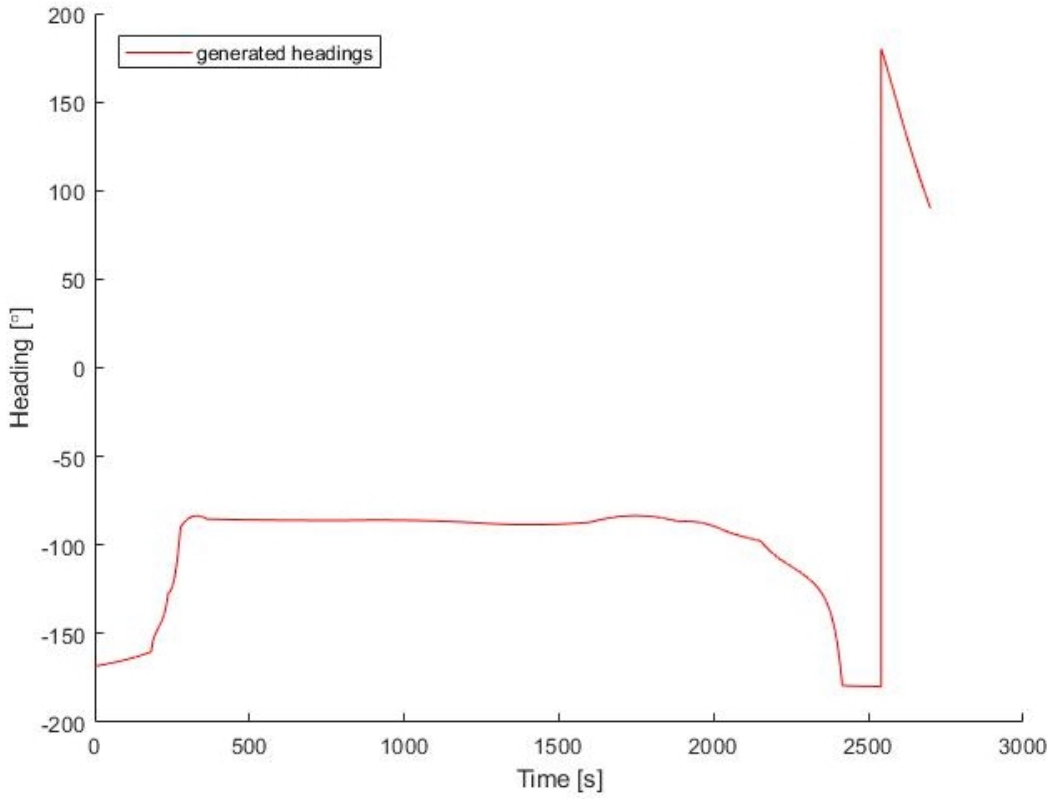

Figure 3.25: Vessel heading vs time (case B)

Figure 3.25 illustrates vessel heading versus time as generated by equation 2.2. Note that the interval over which the vessel heading is roughly constant is the interval over which the vessel is cruising.

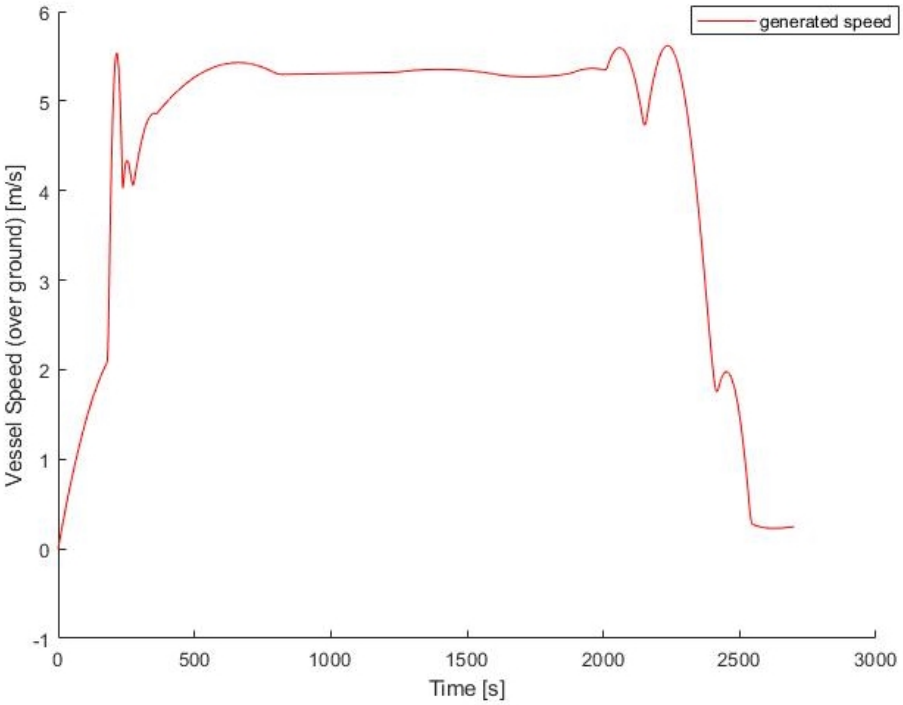

Figure 3.26: Vessel speed vs time (case B)

Figure 3.26 illustrates the vessel's speed over ground throughout the mission. For this mission, the vessel accelerates out of dock, cruises from the start point to the finish point, and then decelerates into dock. Speedwise, case B exhibits the same structure as case A.

3.5.2 Propeller Results

The propeller states generated in this case can be plotted as per figures 3.27, 3.28, and 3.29. The results, so far, look about the same as they did for case A.

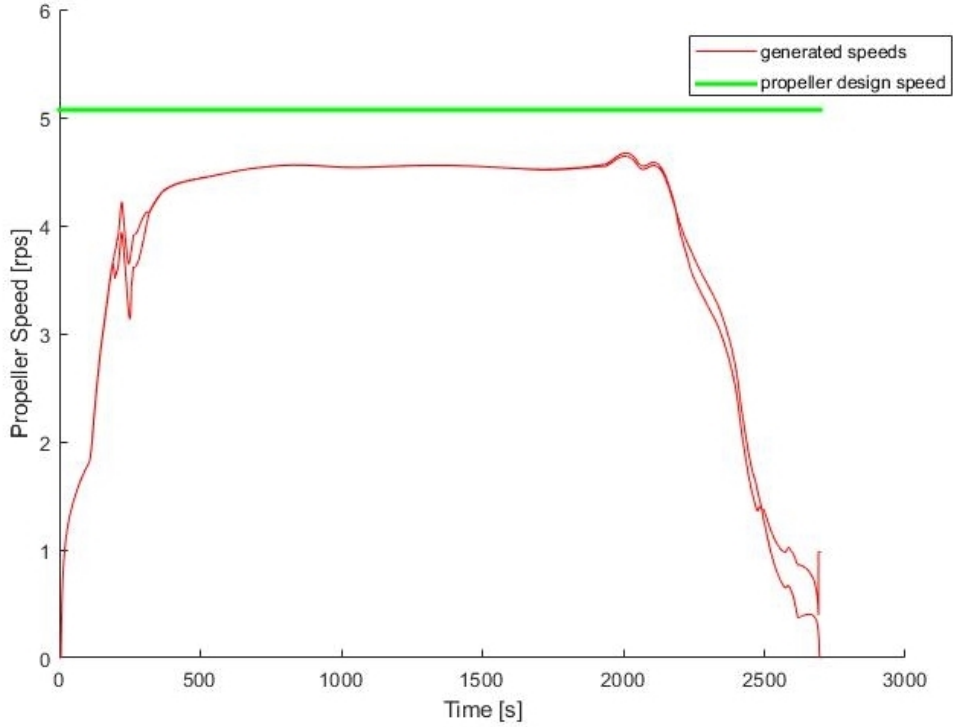

Figure 3.27: Propeller speeds vs time (case B)

Figure 3.27 illustrates propeller speeds vs time, and shows good agreement with the propeller design speed (generated by way of section 2.3.6) while the vessel is cruising.

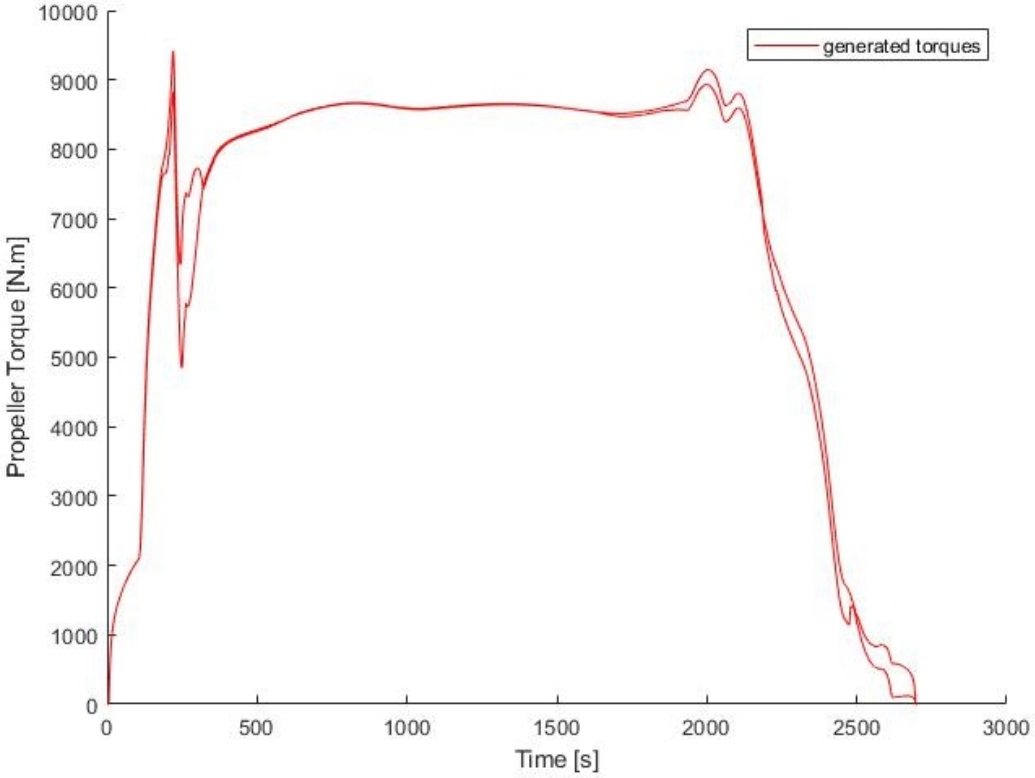

Figure 3.28: Propeller torques vs time (case B)

Figure 3.28 looks similar to figure 3.8, with a fairly steady increase in propeller torques until cruising, then constant, then steady decrease into dock.

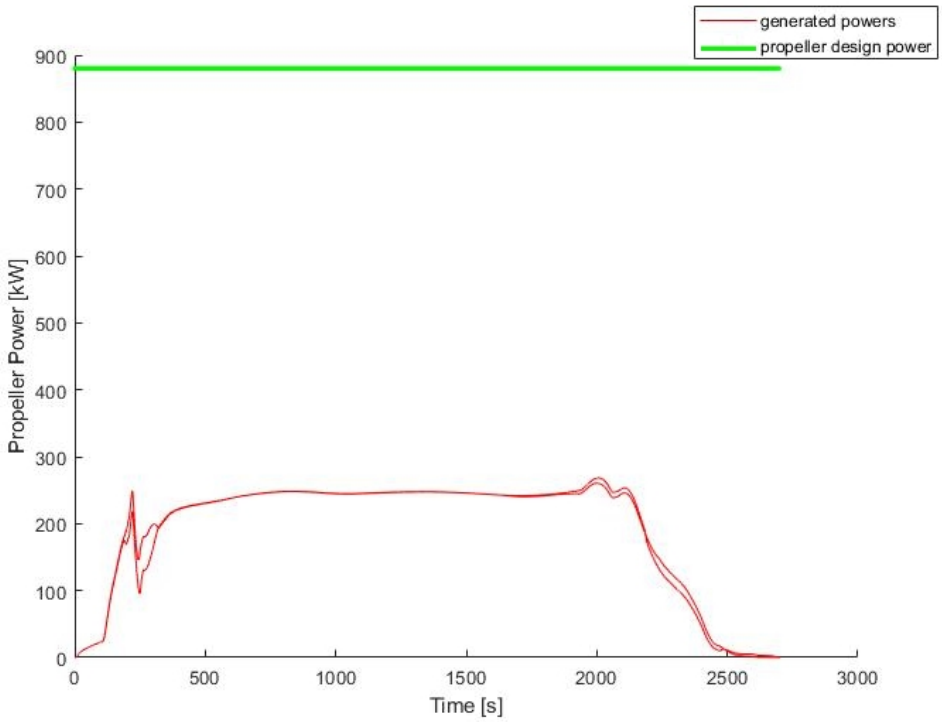

Figure 3.29: Propeller power vs time (case B)

Figure 3.29, like figure 3.9, shows propeller powers that are rather less than the propeller design power. Nonetheless, this will also be shown to be accurate.

3.5.3 Steering Gear Results

The steering gear states generated in this case can be plotted as per figures 3.30 and 3.31. Note that figure 3.31 indicates that the steering gear powers are bounded by about 850 kW everywhere over the mission cycle. This, however, is excessive since the steering gear actually fitted on board in case B is driven by a pair of 3.75 kW hydraulic pumps, according to the vessel's equipment list.

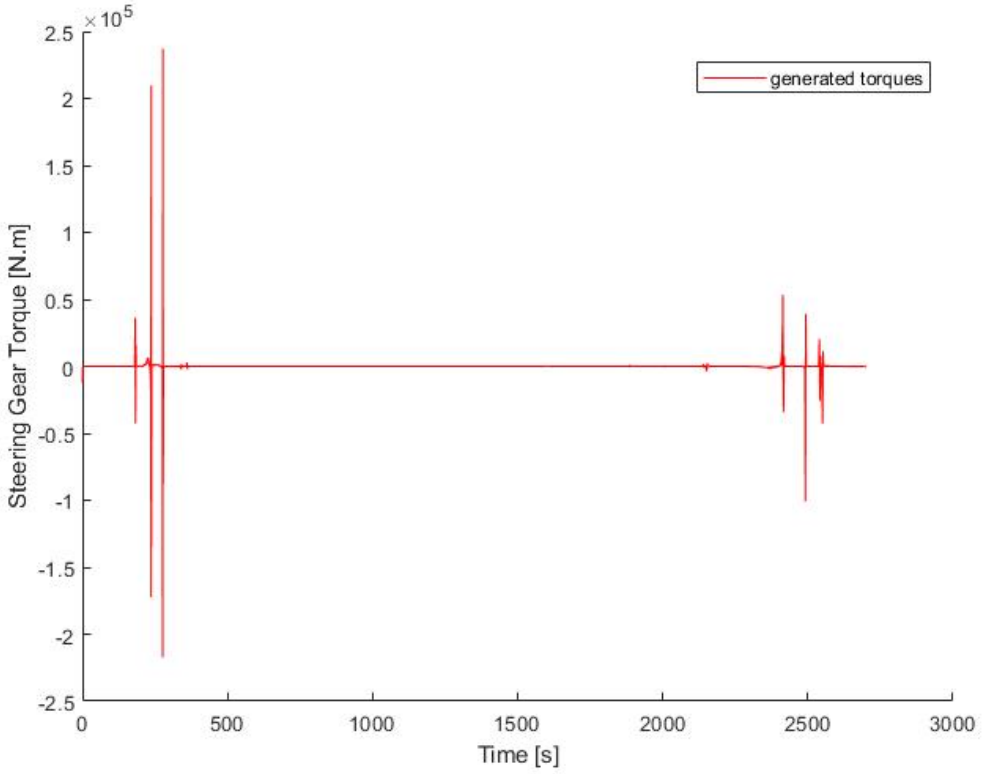

Figure 3.30: Steering gear torques vs time (case B)

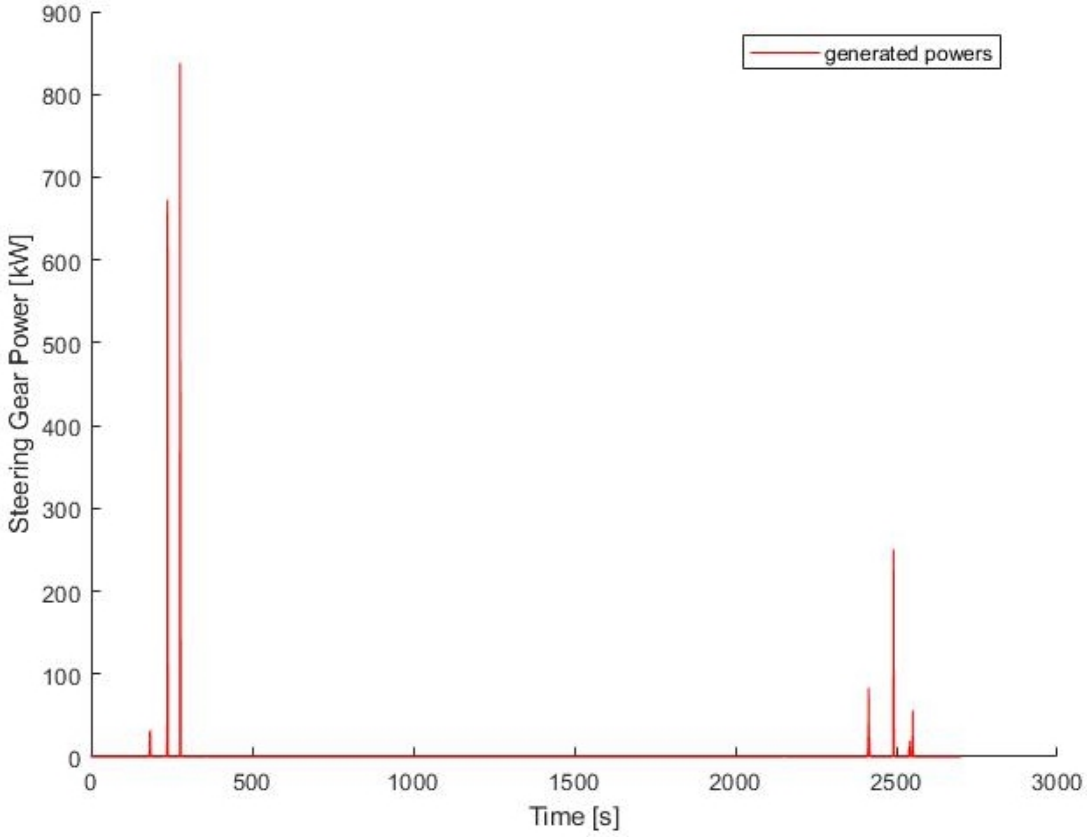

Figure 3.31: Steering gear power vs time (case B)

3.5.4 Work Done and Fuel Required

The work done by the vessel's propellers, in order to accomplish the given mission, can be determined by integrating the results of figure 3.29 over the mission cycle; this yields a result of 1025 MJ. From this, one can estimate a lower bound on the fuel required to accomplish the given mission. Assuming, once again, an energy density of about 38.5 MJ/L, 1025 MJ of energy is equivalent to about 28 litres of fuel. Assuming a transmission efficiency of 95% and an average engine thermal efficiency of, say, 30% over the mission cycle[4], the estimated lower bound on fuel consumption can be adjusted to about 100 litres. This is roughly comparable to the fuel consumption recorded at sea, which for case B was about 105 litres per mission cycle. Once again, more accurate results could be obtained by mapping the propeller states to corresponding engine states and then referring to the engine's specific fuel consumption map. One could also approximate emissions over the mission using this approach, if one has access to the engine's specific emissions map.

[4]This vessel is propelled by a mild hybrid plant.

3.6 Case Study B - Comparison

For this case, data was collected at sea for each of the kinematics and propeller results presented above [Grant and Zhu, 2017b]. A comparison between the generated results and the collected data follows.

3.6.1 Kinematics Results Comparison

A comparison of the kinematics results to the corresponding data is illustrated in figures 3.32 - 3.36, with the "cruising" partition being defined, once again, by those times for which vessel speed and heading are both relatively constant; all other times are considered "maneuvering".

As illustrated in figures 3.32, 3.33, and 3.34, the vessel path generated from the given waypoint set is in good agreement with the actual path traversed by the vessel. Figure 3.35 shows reasonably good agreement between generated vessel headings and recorded headings while cruising, with errors in this state of about $\pm 1.7°$. Heading errors while maneuvering, however, are quite large; about $\pm 66°$ on average (at times, even worse). In this case, this is due to the lack of forward-aft symmetry, which, in turn, means that this vessel is not bi-directional as in case A. At the beginning of its mission, the vessel is in dock, bow towards the shore, and thus needs to back out and turn around before commencing its transit. In addition, the vessel performs a somewhat aggressive maneuver in order to dock at the end of its mission (this maneuver is not visible at the scale of figure 3.32); this maneuver is illustrated in figure 3.37. That is, the vessel slows, and then backs into the dock at the end of its mission cycle. The heading errors at the beginning and end of the mission cycle, therefore, can only be alleviated by fully defining the mission cycle (i.e., latitude, longitude, and heading) ahead of time. This, however, was not attempted as part of this thesis.

Figure 3.36 shows good agreement between the generated and recorded speeds of the vessel, with errors while cruising of about $\pm 1\%$ of the true speed, and errors while maneuvering of about $\pm 6\%$ of the true speed. The larger errors in maneuvering are again likely due to differences in how the actual vessel is controlled versus how the simulated vessel is controlled (compounded further by the modification made).

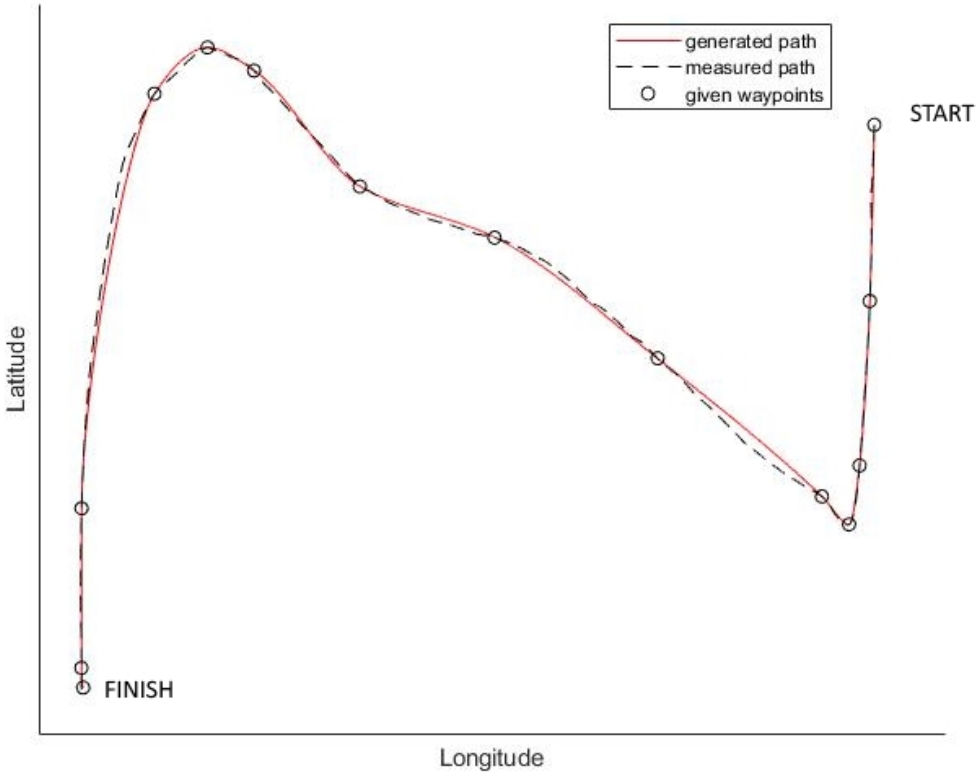

Figure 3.32: Vessel path (case B), comparison

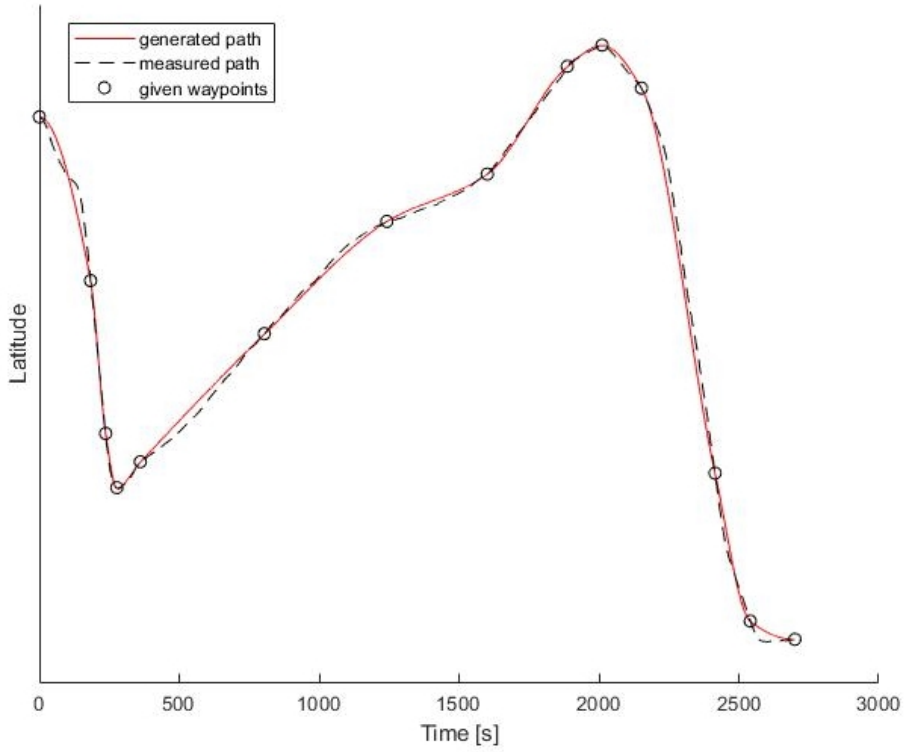

Figure 3.33: Vessel latitude vs time (case B), comparison

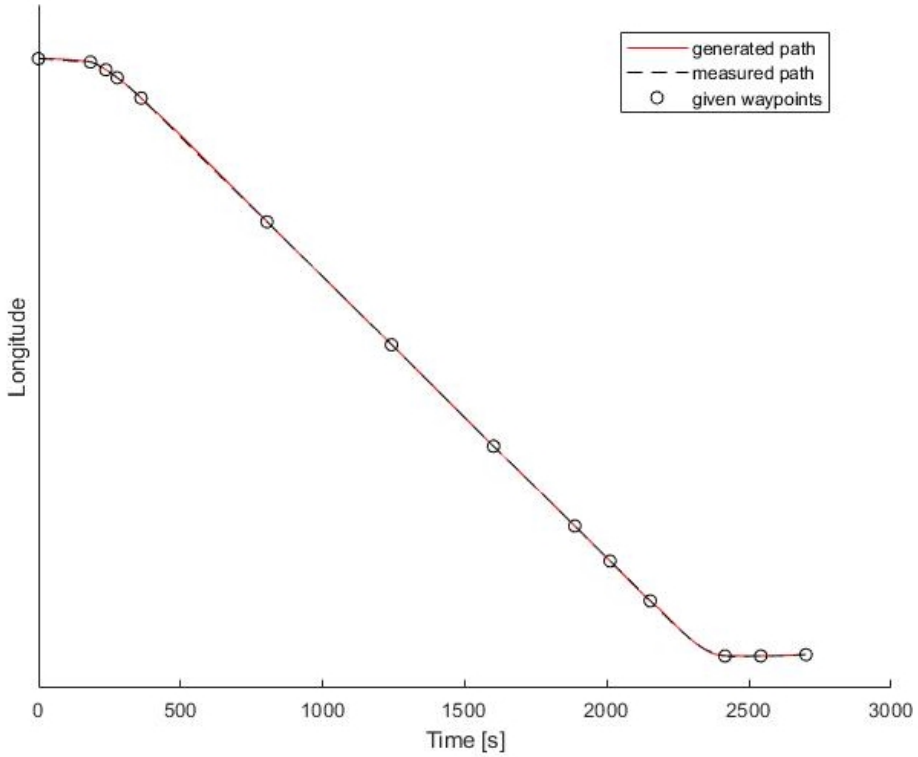

Figure 3.34: Vessel longitude vs time (case B), comparison

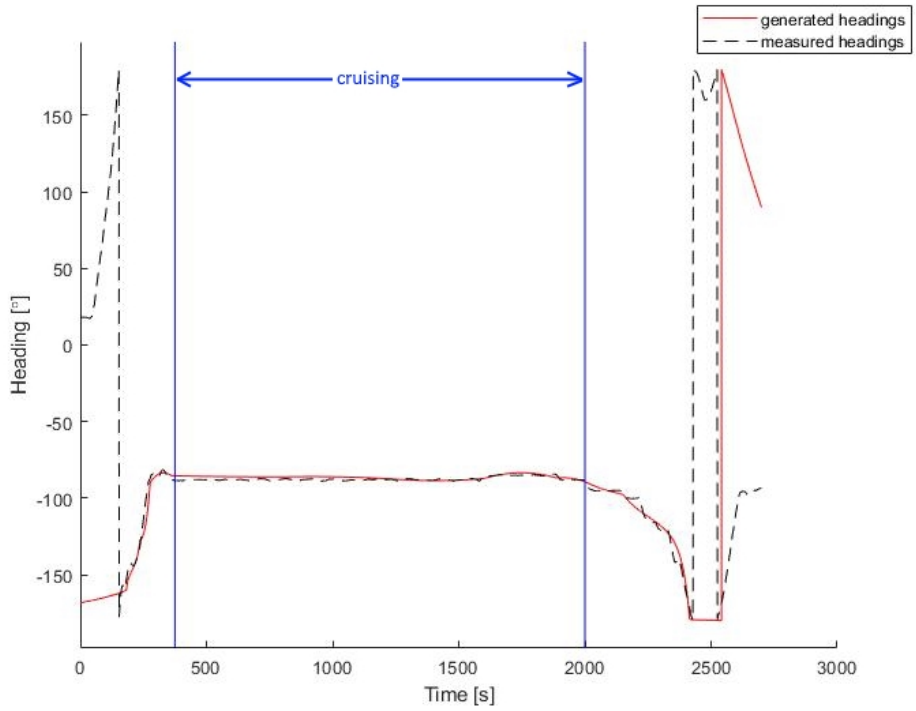

Figure 3.35: Vessel heading vs time (case B), comparison

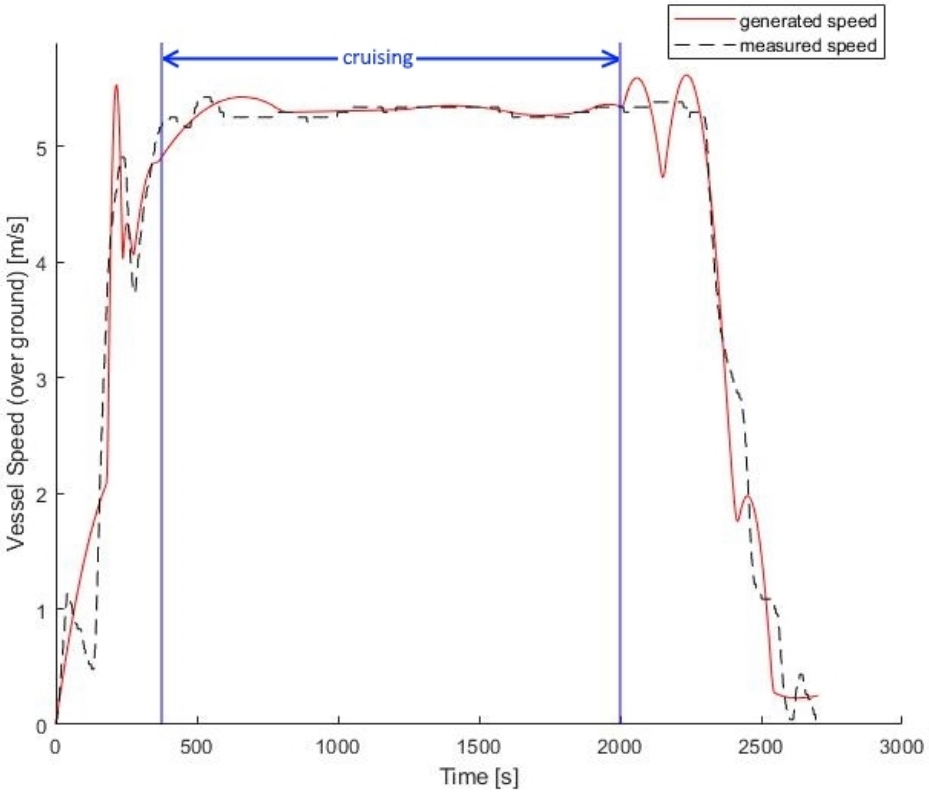

Figure 3.36: Vessel speed vs time (case B), comparison

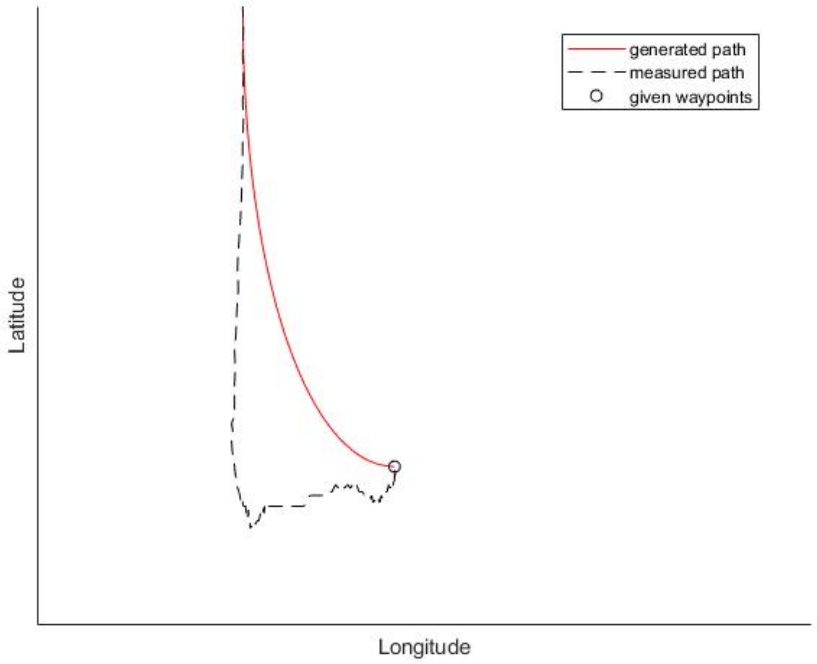

Figure 3.37: End of mission docking maneuver (case B)

3.6.2 Propeller Results Comparison

A comparison of the propeller results to the corresponding data can is illustrated in figures 3.38, 3.39, and 3.40. Figures 3.38, 3.39, and 3.40 all show reasonably good agreement between the generated and recorded values for propeller dynamics. With respect to propeller speeds, the generated values are within about ±2% of the true values while cruising, and within about ±28% of the true values while maneuvering. With respect to propeller torques, the generated values are within about ±8% of the true values while cruising, and within about ±45% of the true values while maneuvering. Finally, with respect to propeller power, the generated values are within about ±9% of the true values while cruising, and within about ±66% of the true values while maneuvering.

It is pleasing to see that, given the modified vessel, the process illustrated in figure 2 was still able to generate results comparable to those measured on the actual vessel, although the maneuvering errors in this case are rather larger than in case A. Still, these results indicate that if the vessel in question spends most of its mission cycle in a cruising state, then one can generate meaningful results even if one modifies the vessel architecture from its original state to an equivalent state composed strictly of azimuthing thrusters.

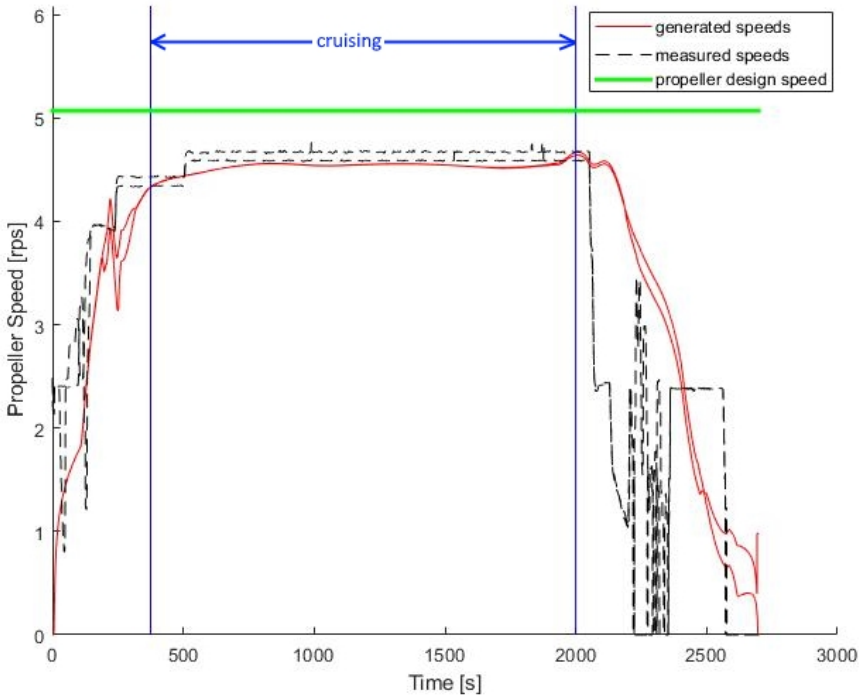

Figure 3.38: Propeller speeds vs time (case B), comparison

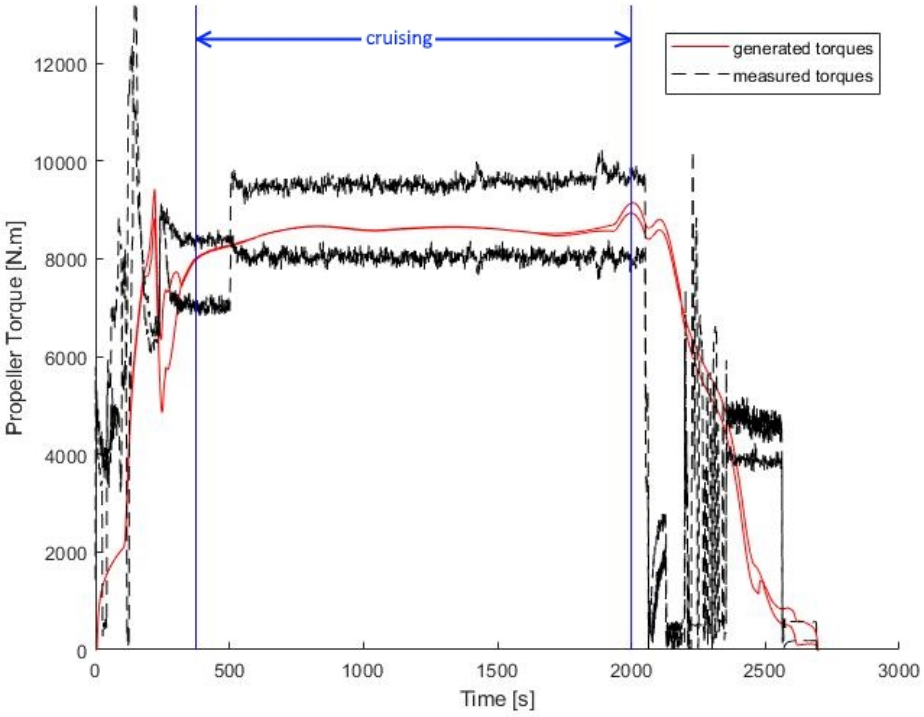

Figure 3.39: Propeller torques vs time (case B), comparison

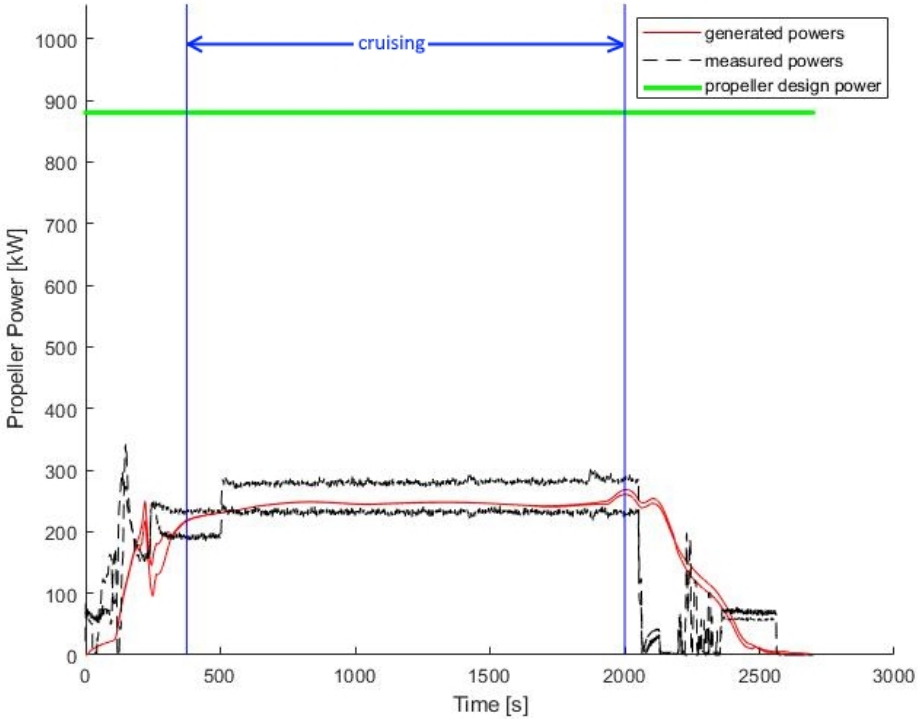

Figure 3.40: Propeller power vs time (case B), comparison

3.7 Discussion

The results generated for cases A and B show that, for a vessel having a ramp up, cruise, ramp down type mission, which can be illustrated, in general, as follows

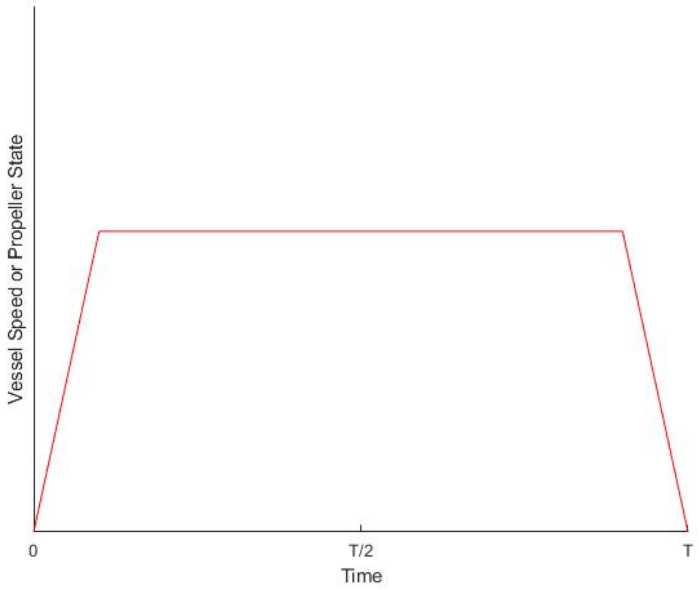

Figure 3.41: Ramp up, cruise, ramp down type mission

the process illustrated in figure 2 works well in terms of predicting propeller states and can also work well in terms of predicting steering states. Since this type of mission is typical for many vessel types (ferries, tankers, carriers, etc.), it follows that the process illustrated in figure 2 covers, in terms of applicability, a large subset of all possible monohull surface vessel designs. Still, the errors between the generated and recorded values were noticeably higher while maneuvering than they were while cruising; this implies that the process, as implemented in this thesis, may not yet be able to handle more dynamic mission types in a satisfactory manner.

The achieved runtimes for each case study are encouraging, with time ratios of about 3.3:1 and 12.8:1 for cases A and B respectively. It is interesting to note, however, that despite the fact that the mission in case B was significantly longer than the mission in case A (45 minutes compared to 27 minutes), the simulation of case B finished in less than half the time it took to simulate case A. Since case A and case B both exhibit about the same ratio in cruising time to maneuvering time, it cannot be a matter of one case having a more dynamic mission than the other. One might conclude instead that runtime is strongly influenced by the number of propellers being modelled. Recall the iterative process for generating appropriate propeller speeds (see, for instance, the algorithm following equation 2.37). Clearly, the generation of propeller states is the most computationally expensive part of the process illustrated in figure 2, so increasing the number of propellers being modelled causes the number of required operations to grow rapidly. Given this, it follows that one can expect simulations involving fewer propellers to run much faster than those involving more propellers, and this is precisely what was observed in the case studies.

Conclusion

Research Contributions

The research contributions of this work can be separated into two distinct categories: global (that is, contributions to the related global research in marine engineering) and local (that is, contributions to the related research in marine engineering being undertaken at the University of Victoria in particular). These contribution categories will be discussed individually in the following sub-sections.

Global Contributions

A survey of the related, global research into marine engineering reveals no work having a comparable mission $\rightarrow$ drive $\rightarrow$ load approach (see figure 2) as is employed in this work. The majority of related, published works focus on one particular aspect of mission, drive, load, or controls assuming that all other information is given (see, for instance, [Caccia et al., 2008, Breivik and Fossen, 2004, Perez and Blanke, 2002, Taghipour et al., 2008, Phillips et al., 2009]). The most similar published work that could be found was [Theotokatos, 2007], which focuses on the coupled propeller-engine dynamics (and so has more of a drive $\leftrightarrow$ load structure, although steering dynamics is not captured). In addition, [Theotokatos, 2007] also uses a surrogate propeller geometry, namely the Wageningen B-series, to facilitate analysis. The work of [Theotokatos, 2007], however, defines the propeller state (ordered speed) ahead of time and it considers only a one-dimensional surge model in calm seas, so while it is comparable to this thesis, it does not offer the same level of generality.

Local Contributions

Vessel modelling work carried out at the University of Victoria has led to the development of a number of distinct vessel modelling approaches, namely

1) general empirical model (based on classical textbook methods; see [Jaster, 2013]);

2) reduced-order hydrodynamics model (see [Andersen, 2016]); and,

3) low-order regression model (see [Rahimpour, 2017])

These modelling approaches each have individual strengths and weaknesses. First, the general empirical model uses empirical equations for all elements of the hull and propeller dynamics, and so it avoids the need for computationally expensive fluid dynamics and/or potential flow modelling. However, setting up the empirical model means providing a large number of coefficients, each of which are contained within a typical range of values. This means that the general empirical model requires a large input set and is exposed to a good deal of subjectivity in that the user needs to choose coefficient values. As a result, the general empirical model can lead to modelling errors on the order of $\pm 20\%$ - $\pm 40\%$, even during cruising.

By comparison, the reduced-order hydrodynamics model is significantly more accurate than the general empirical model (errors of less than $\pm 20\%$). It requires, however, a good deal of pre-computation in order to quantify the hydrodynamics of the vessel being modelled. This means potentially time-consuming fluid dynamics and/or potential flow modelling needs to be undertaken before the model can even be run. In addition, the reduced-order hydrodynamics model, as presently implemented, is only a one-dimensional surge model which requires the driver input to be fully defined ahead of time.

The low-order regression model seeks to achieve the accuracy of the reduced-order hydrodynamics model without having to first perform expensive pre-computation every time it is employed. This is achieved by summarizing a broad set of fluid dynamics and potential flow results, together with vessel-specific results detailed in the vessel's manual of trim and stability, by way of best-fit equations which, in turn, can be used to quickly generate the hydrodynamical properties of the vessel of interest. What results is a model that is less time consuming to employ than the reduced-order hydrodynamics model, and more accurate than the general empirical model.

The methodology presented in this thesis differs from all three of the methods discussed above, and might be classified as a generic mathematical model. First, expensive pre-computation is avoided entirely by way of using a surrogate geometry for the hull. The existence of a closed-form expression for the surrogate hull geometry then allows one to determine the hull hydrodynamics analytically, as per the hull surrogate geometry section presented previously. In addition, a surrogate propeller geometry is also used, namely the Wageningen B-series, for which the general dynamics have already been expressed empirically [Bernitsas et al., 1981]. The results achieved in this thesis, therefore, demonstrate the credibility of using surrogate geometries to facilitate an analytical approach to vessel modelling. Furthermore, this method takes in a mission, select vessel properties (which can be extracted from the vessel's manual of trim and stability), and weather conditions, and generates, from that alone, both propeller and steering gear states everywhere over the mission. It is therefore more all-encompassing than the previously developed modelling methodologies, in that it considers mission, drive, and load altogether, and it generates both propeller and steering gear dynamics. This method is also fast and easy to generalize, and so it better allows one to play "what-if?" games regarding considerations such as vessel routing, choice of plant architecture, degree of hybridization, etc. than the previously developed methods; this, arguably, makes it more useful in practice.

Recommendations

If one considers the case studies performed, then the observed accuracy, together with the rapid runtimes achieved and sparse inputs given, leads one to conclude that the methodology presented in this thesis shows promise in terms of being able to generate representative load cycles for arbitrary monohull surface vessels. Therefore, from its current state, the methodology presented in this thesis should be extended to handle both more dynamic mission types and non-monohull vessels (catamarans, trimarans, etc.). In terms of handling more dynamic mission types, this might be achieved by implementing some kind of driver model. Indeed, good results (prediction errors of less than $\pm 20\%$) were achieved in [Andersen, 2016], where a driver model based on control input data collected at sea was implemented. Therefore, it stands to reason that implementing a generalized driver model, which approaches the behaviour of practical vessel control, would lead to more accurate results while the vessel is in a maneuvering state. In addition, maneuvering, even in perfectly calm seas, tends to introduce non-negligible roll motions, and so extending the surge-sway-yaw model to a surge-sway-roll-yaw model would also contribute to reducing maneuvering errors (see, for instance, [Perez and Blanke, 2002]), albeit at the expense of complicating equation 1.32 somewhat (as the simplifying assumptions $p \approx 0$ and $\phi \approx 0$ would no longer be valid).

In terms of handling non-monohull vessels, one might immediately achieve this using the same Wigley N43 surrogate geometry by simply assembling the hull of interest from a number of N43s. For example, the submerged geometry of a catamaran might be modelled as two N43s, side-by-side, separated abeam by some distance. Hull parameters (wetted area, added masses, etc.) could then be computed by only slightly modifying the theory presented in section 1.4 of this thesis. As for other non-monohull vessels lacking ship-like architecture altogether (an oil rig, for example), one could still apply the same hull modelling approach, only this time using a different, more suitable surrogate geometry (perhaps just a cylinder would suffice for the case of an oil rig).

Finally, more representative surrogate geometries than those employed in this thesis might be sought. For example, the KCS hull geometry (see, for instance, [Van et al., 1997] or [Miao et al., 2016]) exhibits a bulbous bow and no forward-aft symmetry (i.e., more similar to figure 3.20 than the Wigley N43), and so would be more applicable to vessels having this general architecture, which many vessels do. However, moving to more realistic geometries such as the KCS would also likely mean giving up a closed-form expression for $y_+(x, z)$, as such hull geometries are typically defined only by a point set or a body plan (i.e., a series of transverse cuts spanning the length of the vessel). This loss of generality would have to be mitigated somehow (perhaps

by fitting a polynomial surface to the point set). More representative propeller geometries could be sought as well, especially since the K_T and K_Q polynomials presented in [Bernitsas et al., 1981] model only propeller technology advanced to the point of 1981 at the latest. In order to compensate for advances in propeller technology since then, new K_T and K_Q models would have to be generated for a more modern propeller geometry.

References

[CSA, 2001] (2001). Canada Shipping Act. Available online: https://laws-lois.justice.gc.ca/eng/acts/C-10.15/page-16.html#h-73.

[Alvarez et al., 2010] Alvarez, R., Schlienger, P., and Weilenmann, M. (2010). Effect of hybrid system battery performance on determining CO2 emissions of hybrid electric vehicles in real-world conditions. *Energy Policy*, 38:6919 – 6925. DOI: 10.1016/j.enpol.2010.07.008.

[Andersen, 2016] Andersen, K. (2016). Development of a Time-Domain Modeling Platform for Hybrid Marine Propulsion Systems. Master's thesis, University of Victoria.

[Avallone et al., 2017] Avallone, E., III, T. B., and Sadegh, A., editors (2017). *Marks' Standard Handbook for Mechanical Engineers*. McGraw-Hill, 11th edition. ISBN: 978-0-07-142867-5.

[Aveek, 2009] Aveek (2009). Multihull.svg. Wikimedia Commons. Image in the public domain. Available online: https://commons.wikimedia.org/wiki/File:Multihull.svg.

[Bandyk, 2009] Bandyk, P. (2009). *A Body-Exact Strip Theory Approach to Ship Motion Computations*. PhD thesis, University of Michigan. Available online: https://deepblue.lib.umich.edu/bitstream/handle/2027.42/64799/pbandyk_1.pdf?sequence=1&isAllowed=y.

[Bernitsas et al., 1981] Bernitsas, M. M., Ray, D., and Kinley, P. (1981). K_T, K_Q, and Efficiency Curves for the Wageningen B-Series Propellers. Technical Report 237, University of Michigan: Department of Naval Architecture and Marine Engineering. Available online: https://deepblue.lib.umich.edu/bitstream/handle/2027.42/3557/bab2786.0001.001.pdf?sequence=5&isAllowed=y.

[bin Tarafder et al., 2007] bin Tarafder, M. S., bin M Khalil, G., and bin Mahmud, S. M. I. (2007). Computation of wave-making resistance of Wigley hull form using Michell's integral. *The Institution of Engineers, Malaysia*, 68(4). Available online: http://dspace.unimap.edu.my/dspace/bitstream/123456789/13635/1/033-040_Computation%205pp.pdf.

[Blendermann, 1994] Blendermann, W. (1994). Parameter identification of wind loads on ships. *Journal of Wind Engineering and Industrial Aerodynamics*, 51:339 – 351. DOI: 10.1016/0167-6105(94)90067-1.

[Breivik and Fossen, 2004] Breivik, M. and Fossen, T. (2004). Path Following for Marine Surface Vessels. Technical report, Norwegian University of Science and Technology. Available online: https://www.researchgate.net/profile/Morten_Breivik/publication/4130073_Path_following_for_marine_surface_vessels/links/09e4150a17aaa53763000000/Path-following-for-marine-surface-vessels.pdf.

[Brosen, 2006] Brosen (2006). Brosen shipsmovemensonthewave.svg. Wikimedia Commons. Image released under a Creative Commons licence. Available online: https://fr.wikipedia.org/wiki/Fichier:Brosen_shipsmovemensonthewave.svg.

[Buckham, 2017] Buckham, B. (2017). MECH 546: Introduction to Ocean Engineering. Course Notes. University of Victoria.

[Caccia et al., 2008] Caccia, M., Bibuli, M., Bono, R., and Bruzzone, G. (2008). Basic navigation, guidance and control of an Unmanned Surface Vehicle. *Auton Robot*, 25:349 – 365. DOI: 10.1007/s10514-008-9100-0.

[Chen and Dong, 2018] Chen, L. L. and Dong, Z. (2018). Life Cycle Cost-model Based Design Optimization for Hybrid Electric Marine Propulsion System. Manuscript submitted for review.

[Chen et al., 2018] Chen, L. L., Feng, Y., Zhu, H. A., and Dong, Z. (2018). Optimal Design of Hybrid Electric Marine Propulsion System with Li-ion Battery Performance Degradation Model. Manuscript submitted for review.

[Dedes et al., 2012] Dedes, E., Hudson, D., and Turnock, S. (2012). Assessing the potential of hybrid energy technology to reduce exhaust from global shipping. *Energy Policy*, 40:204 – 218. DOI: 10.1016/j.enpol.2011.09.046.

[DNV-GL, 2015] DNV-GL (2015). IMO NOx Tier III requirements to take effect on January 1st 2016. Web article. Available online: https://www.dnvgl.com/news/imo-nox-tier-iii-requirements-to-take-effect-on-january-1st-2016-51970.

[Ellis and Garrison, 2016] Ellis, R. and Garrison, T. (2016). *Oceanography: An Invitation to Marine Science*. Cengage Learning, 9th edition. ISBN: 978-1-305-25428-2.

[FCIT, 2005] FCIT (2005). Waves. Social studies resource for students and teachers produced by the Florida Center for Instructional Technology (FCIT). Available online: https://fcit.usf.edu/florida/teacher/science/mod2/resources/waves.pdf.

[Fontaras et al., 2008] Fontaras, G., Pistikopoulos, P., and Samaras, Z. (2008). Experimental evaluation of hybrid vehicle fuel economy and pollutant emissions over real-world simulation driving cycles. *Atmospheric Environment*, 42(18):4023 – 4035. DOI: 10.1016/j.atmosenv.2008.01.053.

[Fossen, 2011] Fossen, T. (2011). *Handbook of Marine Craft Hydrodynamics and Motion Control*. John Wiley and Sons, Ltd. ISBN: 978-1-119-99149-6.

[Geertsma et al., 2017] Geertsma, R., Negenborn, R., Visser, K., and Hopman, J. (2017). Design and control of hybrid power and propulsion systems for smart ships: A review of developments. *Applied Energy*, 194:30 – 54. DOI: 10.1016/j.apenergy.2017.02.060.

[German, 2015] German, J. (2015). Hybrid vehicles: Technology development and cost reduction. *ICCT Technical Brief*, (1). Available online: https://www.theicct.org/sites/default/files/publications/ICCT_TechBriefNo1_Hybrids_July2015.pdf.

[Grant and Zhu, 2017a] Grant, M. and Zhu, H. A. (2017a). Operational data for car-deck ferry A. Data collected at sea.

[Grant and Zhu, 2017b] Grant, M. and Zhu, H. A. (2017b). Operational data for car-deck ferry B. Data collected at sea.

[Hoerner, 1965] Hoerner, S. F. (1965). *Fluid-Dynamic Drag*. Self publised. Available online: http://dl.kashti.ir/ENBOOKS/NEW/FDD.pdf.

[Hoffmann and Sirimanne, 2017] Hoffmann, J. and Sirimanne, S. (2017). *Review of Maritime Transport*. United Nations Conference on Trade and Development. ISBN: 978-92-1-362808-9.

[IMO, 2011] IMO (2011). *International convention for the prevention of pollution from ships (MARPOL) annex VI*. International Maritime Organization.

[IMO, 2018a] IMO (2018a). Emission Control Areas (ECAs) designated under MARPOL Annex VI. Webpage. Available online: http://www.imo.org/en/OurWork/Environment/PollutionPrevention/AirPollution/Pages/Emission-Control-Areas-(ECAs)-designated-under-regulation-13-of-MARPOL-Annex-VI-(NOx-emission-control).aspx.

[IMO, 2018b] IMO (2018b). Nitrogen Oxides (NOx) - Regulation 13. Webpage. Available online: http://www.imo.org/en/OurWork/Environment/PollutionPrevention/AirPollution/Pages/Nitrogen-oxides-(NOx)-%E2%80%93-Regulation-13.aspx.

[ITTC, 1957] ITTC (1957). Skin Friction and Turbulence Stimulation. In Acevedo, M. L. and Mazarredo, L., editors, *Eighth International Towing Tank Conference*, pages 71 – 85. Available online: http://mararchief.tudelft.nl/catalogue/entries/17294/.

[Janssen, 2004] Janssen, P. (2004). *The Interaction of Ocean Waves and Wind*. Cambridge University Press. ISBN: 0-521-46540-0.

[Jaster, 2013] Jaster, T. (2013). Modeling and Simulation of a Hybrid Electric Vessel. Master's thesis, University of Victoria.

[Korotkin, 2009] Korotkin, A. (2009). *Added Masses of Ship Structures*. Springer, 12th edition. ISBN: 978-1-4020-9431-6.

[Manouchehrinia et al., 2018a] Manouchehrinia, B., Gulliver, T. A., and Dong, Z. (2018a). Wells-to-Propeller Environmental Assessment of Natural Gas as a Transportation Fuel in BC Canada. Manuscript submitted for review.

[Manouchehrinia et al., 2018b] Manouchehrinia, B., Molloy, S., Dong, Z., Gulliver, T. A., and Gough, C. (2018b). Emission and life-cycle cost analysis of hybrid and pure electric propulsion systems for fishing boats. *Journal of Ocean Science*, 13(2):64 – 87. Available online: https://www.researchgate.net/publication/327541027_Emission_and_life-cycle_cost_analysis_of_hybrid_and_pure_electric_propulsion_systems_for_fishing_boats.

[Miao et al., 2016] Miao, A., Wu, J., and Wan, D. (2016). Hull form optimization based on a NM+CFD integrated method for KCS. Technical report, State Key Laboratory of Ocean Engineering. Available online: www.sci-en-tech.com/ICCM2016/PDFs/1501-5522-1-PB.pdf.

[MIT, 2004] MIT (2004). Propellers and Propulsion. MIT OpenCourseWare. Available online: https://ocw.mit.edu/courses/mechanical-engineering/2-154-maneuvering-and-control-of-surface-and-underwater-vehicles-13-49-fall-2004/lecture-notes/lec12.pdf.

[NDBC, 1996] NDBC (1996). Nondirectional and directional wave data analysis procedures. Technical report, National Data Buoy Center. Available online: http://www.ndbc.noaa.gov/wavemeas.pdf.

[Owen et al., 2018] Owen, D., Demirel, Y. K., Oguz, E., Tezdogan, T., and Incecik, A. (2018). Investigating the effect of biofouling on propeller characteristics using CFD. *Ocean Engineering*, 159:505 – 516. DOI: 10.1016/j.oceaneng.2018.01.087.

[Paykani and Shervani-Tabar, 2011] Paykani, A. and Shervani-Tabar, M. T. (2011). A comparative study of hybrid electric vehicle fuel consumption over diverse driving cycles. *Theoretical and Applied Mechanics Letters*, 1(5):052005. DOI: 10.1063/2.1105205.

[Perez and Blanke, 2002] Perez, T. and Blanke, M. (2002). Mathematical Ship Modeling for Control Applications. Technical report, Technical University of Denmark. Available online: https://core.ac.uk/download/pdf/86558528.pdf.

[Peters, 2017] Peters, G. (2017). Hybrid vessels: here to stay, or fleeting trend? *Ship Technology*. Web article. Available online: https://www.ship-technology.com/features/featurehybrid-vessels-here-to-stay-or-fleeting-trend-5769261/.

[Phillips et al., 2009] Phillips, A., Turnock, S., and Furlong, M. (2009). Evaluation of manoeuvring coefficients of a self-propelled ship using a blade element momentum propeller model coupled to a Reynolds average Navier Stokes flow solver. *Ocean Engineering*, 36(15):1217 – 1225. DOI: 10.1016/j.oceaneng.2009.07.019.

[Pinkster, 1971] Pinkster, J. (1971). *Dynamic Positioning of Vessels at Sea*. Springer. ISBN: 978-3-7091-2983-8.

[Rahimpour, 2017] Rahimpour, M. (2017). low-order regression model.

[Rahimpour, 2018] Rahimpour, M. (2018). Thrust and torque coefficient data for a 1.9 m (dia.), four-bladed propeller. Computational fluid dynamics results, StarCCM+.

[Rahimpour and McIntyre, 2018] Rahimpour, M. and McIntyre, D. (2018). Wigley N43 hull drag data for car-deck ferry A. Computational fluid dynamics results, StarCCM+.

[Sandwell, 2010] Sandwell, D. (2010). Physics of surfing waves. Technical presentation. Available online: http://topex.ucsd.edu/ps/waves.pdf.

[Schultz, 2007] Schultz, M. P. (2007). Effects of coating roughness and biofouling on ship resistance and powering. *Journal of Bioadhesion and Biofilm Research*, 23(5):331 – 341. DOI: 10.1080/08927010701461974.

[Sen and Vinh, 2016] Sen, D. T. and Vinh, T. C. (2016). Determination of added mass and inertia moment of marine ships moving in 6 degrees of freedom. *International Journal of Transportation Engineering and Technology*, 2(1):8 – 14. DOI: 10.11648/j.ijtet.20160201.12.

[Sioshansi and Denholm, 2009] Sioshansi, R. and Denholm, P. (2009). Emissions impacts and benefits of plug-in hybrid electric vehicles and vehicle-to-grid services. *Environmental Science & Technology*, 43(4):1199 – 1204. DOI: 10.1021/es802324j.

[Stokes, 1880] Stokes, G. (1880). *Mathematical and Physical Papers*, volume I. Cambridge University Press. Available online: https://archive.org/details/mathphyspapers01stokrich.

[Sun et al., 2012] Sun, J., Lv, X., Liu, W., Ning, H., and Chen, X. (2012). Research on a method of hull form design based on wave-making resistance optimization. *Polish Maritime Research*, 3(75):16 – 25. DOI: 10.2478/v10012-012-0027-1.

[Taghipour et al., 2008] Taghipour, R., Perez, T., and Moan, T. (2008). Hybrid frequency-time domain models for dynamic response analysis of marine structures. *Ocean Engineering*, 35(7):685 – 705. DOI: 10.1016/j.oceaneng.2007.11.002.

[Techet, 2005] Techet, A. H. (2005). Marine propellers. MIT OpenCourseWare. Available online: http://web.mit.edu/2.016/www/handouts/2005Reading10.pdf.

[Theotokatos, 2007] Theotokatos, G. P. (2007). A Modelling Approach for the Overall Ship Propulsion Plant Simulation. In *Proceedings of 6th WSEAS International Conference on System Science and Simulation in Engineering*, pages 21 – 23. WSEAS. Available online: http://citeseerx.ist.psu.edu/viewdoc/download?doi=10.1.1.590.3916&rep=rep1&type=pdf.

[Tupper, 2013] Tupper, E. (2013). *Introduction to Naval Architecture*. Elsevier Ltd., 5th edition. ISBN: 978-0-08-098237-3.

[USNA, 2007] USNA (2007). Chapter 7: Resistance and powering of ships. Online course notes. Available online: https://www.usna.edu/NAOE/_files/documents/Courses/EN400/02.07 Chapter 7.pdf.

[Van et al., 1997] Van, S. H., Kim, W. J., Kim, D. H., Yim, G. T., Lee, C. J., and Eom, J. Y. (1997). Measurement of Flows Around a 3600TEU Container Ship Model. In *Proceedings of the Annual Autumn Meeting*, pages 300 – 304. SNAK.

[Yeo et al., 2014] Yeo, K. B., Choong, W. H., and Hau, W. Y. (2014). Prediction of propeller blade stress distribution through FEA. *Journal of Applied Sciences*, 14:3046 – 3054. DOI: 10.3923/jas.2014.3046.3054.

Appendix A

Mass Moment of Inertia Experimentation

Car-Deck Ferry A

For car-deck ferry A, access to the vessel's manual of trim and stability was available. Therefore, $I_{zz}^{O_b}$ was calculated in the classical manner using the vessel's mass table, for deep departure condition, as follows

Table 1: Car-Deck Ferry A - Mass Table (deep departure)

Part	**Mass** [kg]	x_i [m]	y_i [m]	$\|\|\vec{r}_{dm}\|\|_2^2$ [m]	$I_{zz,i}$ [kg.m^2]
Light Ship	1927800	0.237	-0.057	0.0594	114546.020
Crew & Effects	3000	0	0	0	0
Stores	5000	0	0	0	0
Private Vehicles	180000	0	0	0	0
Passengers	44500	0	0	0	0
Day-Tank	21580	13.744	0	188.898	4076408.827
Fuel-Oil Tank	74930	16.91	-0.002	285.948	21426091.433
Potable Water Tank	31470	-17.498	6.885	353.583	11127264.217
Non-Potable Water Tank	31470	-17.498	-6.885	353.583	11127264.217
Emergency Generator Tank	5270	-3.75	9	95.063	500.979.375
				$\sum I_{zz,i}$	48372554.088

Applying equation 1.44, with $\rho = 1025$ kg/m^3, $L = 105.44$ m, $B = 19.11$ m, and $T = 2.36$ m then yielded the following

$$\widetilde{I_{zz}^{O_b}} = 1480144620.862 \text{ kg.m}^2$$

And so, the appropriate value for C_{inertia} in this case is

$$C_{\text{inertia}} = \frac{I_{zz}^{O_b}}{\widetilde{I_{zz}^{O_b}}} \cong 0.033$$

Car-Deck Ferry B

For car-deck ferry B, access to the vessel's manual of trim and stability was available. Therefore, $I_{zz}^{O_b}$ was calculated in the classical manner using the vessel's mass table, for deep departure condition, as follows

Table 2: Car-Deck Ferry B - Mass Table (deep departure)

Part	**Mass** [kg]	x_i [m]	y_i [m]	$\|\|\vec{r}_{dm}\|\|_2^2$ [m]	$I_{zz,i}$ [kg.m^2]
Light Ship	602903.7	-0.506	0.043	0.258	155647.429
Stores & Provisions	4064.2	0.763	0	0.581	2362.951
Crew & Effects	711.235	3.05	0	9.303	6616.264
Passengers	10770.13	3.05	0	9.303	100189.134
Cars	25198.04	0	0	0	0
Trucks	64011.15	-1.098	0	1.206	77172.098
Freshwater Tank	12487.25	15.503	0	240.348	3001282.398
Fuel-Oil Tank STBD	13086.72	-11.261	1.168	128.166	1677268.939
Fuel-Oil Tank PORT	13086.72	-11.261	-1.168	128.166	1677268.939
Day-Tank	2021.94	-7.976	0	63.613	128620.805
Dirty Oil Tank	0	-8.873	3.407	90.327	0
Sewage Tank	0	-16.192	-1.934	265.935	0
Dirty Water Tank	0	-8.409	-3.376	82.108	0
Lube Oil Tank	2296.273	-6.417	-4.511	61.529	141287.670
				$\sum I_{zz,i}$	6967716.687

Applying equation 1.44, with $\rho = 1025$ kg/m^3, $L = 45.87$ m, $B = 14.63$ m, and $T = 2.63$ m then yielded the following

$$\widetilde{I_{zz}^{O_b}} = 111505935.815 \text{ kg.m}^2$$

And so, the appropriate value for C_{inertia} in this case is

$$C_{\text{inertia}} = \frac{I_{zz}^{O_b}}{\widetilde{I_{zz}^{O_b}}} \cong 0.062$$

Appendix B

Validation of Hull Drag Equations

Set-up

A Wigley N43 hull having dimensions length 105 m, beam 19 m, and draft 2.4 m, (i.e., corresponding to car-deck ferry A) was simulated, using StarCCM+, in order to determine total fluid resistance at a variety of Froude numbers [Rahimpour and McIntyre, 2018]. Since the cruising speed of this particular vessel is 7.46 m/s (about 14.5 knots), which corresponds to a Froude number of 0.2324, it was decided to simulate the vessel at discrete Froude numbers spanning the interval [0.10,0.40]. The simulation results would then be compared to theoretical results obtained by way of the following

$$R_T = \frac{1}{2}\rho(C_V + C_w)A_{\text{wetted}}u^2 \tag{1a}$$

$$C_V = (1+K)C_f \tag{1b}$$

$$C_f = \frac{3}{40(\log_{10}(\text{Re}_L) - 2)^2} \tag{1c}$$

$$K \cong 19\left(\frac{C_b B}{L}\right)^2 \tag{1d}$$

with $C_w = f(\text{Fr}_L)$, as defined in [bin Tarafder et al., 2007]. This expression for theoretical drag was used, for the purpose of validation, because it represents a hydraulically smooth hull with no appendages, precisely what was simulated.

Results

Simulation Results

The results of the simulation follow

Table 3: Total fluid resistance - simulation

Fr_L	u [m/s]	R_T [N]	Re_L	$C_V + C_w$	C_f	Fr_L^4/C_f	$(C_V + C_w)/C_f$
0.10	3.216	12929	3.218E+08	0.00151	0.00177	0.05646	0.85283
0.11	3.538	15678	3.540E+08	0.00151	0.00175	0.08372	0.86557
0.12	3.859	19835	3.861E+08	0.00161	0.00173	0.11995	0.93079
0.13	4.181	24879	4.183E+08	0.00172	0.00171	0.16697	1.00530
0.14	4.503	31648	4.505E+08	0.00189	0.00169	0.22677	1.11342
0.15	4.824	39860	4.827E+08	0.00207	0.00168	0.30153	1.23262
0.20	6.432	87207	6.436E+08	0.00255	0.00162	0.98895	1.57416
0.23	7.397	131538	7.401E+08	0.00290	0.00159	1.76065	1.82752
0.25	8.040	168916	8.045E+08	0.00316	0.00157	2.48364	2.00736
0.30	9.648	288980	9.653E+08	0.00375	0.00154	5.26887	2.43985
0.35	11.257	474973	1.126E+09	0.00453	0.00151	9.94924	3.00301
0.40	12.865	732862	1.287E+09	0.00535	0.00148	17.25328	3.60612

The last two columns of table 3 allow one to extract a value for the form factor, K, as per [ITTC, 1957], in the following manner. First, plot C_T/C_f vs Fr_L^4/C_f, and then construct a line of best fit

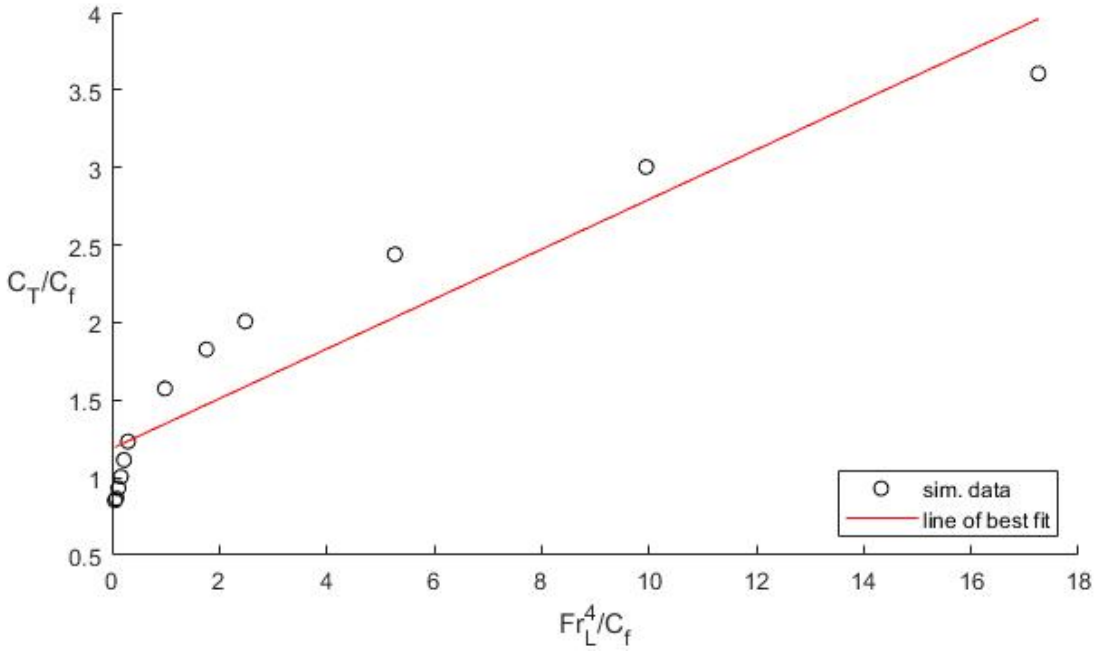

Figure 42: Form factor plot

The line of best fit for figure 42 is given by

$$\frac{C_T}{C_f} = 0.1606\frac{\mathrm{Fr}_L^4}{C_f} + 1.1876 \tag{2}$$

from which one can conclude that $1 + K = 1.1876$. Therefore, the results in table 3 can be separated into viscous and wave-making components, R_V and R_w (with $R_T = R_V + R_w$), as follows

Table 4: Viscous and wave-making resistance - simulation

Fr_L	u [m/s]	R_T [N]	Re_L	C_f	C_V	R_V [N]	R_w [N]
0.10	3.216	12929	3.218E+08	0.00177	0.00210	18005	-5075
0.11	3.538	15678	3.540E+08	0.00175	0.00208	21511	-5833
0.12	3.859	19835	3.861E+08	0.00173	0.00205	25307	-5472
0.13	4.181	24879	4.183E+08	0.00171	0.00203	29390	-4511
0.14	4.503	31648	4.505E+08	0.00169	0.00201	33756	-2108
0.15	4.824	39860	4.827E+08	0.00168	0.00199	38404	1456
0.20	6.432	87207	6.436E+08	0.00162	0.00192	65792	21415
0.23	7.397	131538	7.401E+08	0.00159	0.00189	85479	46059
0.25	8.040	168916	8.045E+08	0.00157	0.00187	99935	68982
0.30	9.648	288980	9.653E+08	0.00154	0.00183	140661	148319
0.35	11.257	474973	1.126E+09	0.00151	0.00179	187838	287135
0.40	12.865	732862	1.287E+09	0.00148	0.00176	241353	491509

Of note in table 4 are the negative R_w values for the lower Froude numbers. It is not entirely clear why this is happening (perhaps an error in the simulation?), but negative wave-making resistance at any speed makes no physical sense (a moving vessel will always generate a wave, which will always cost some amount of energy). By interpolation, it was found that the simulated R_w values dropped to zero by about $\mathrm{Fr}_L = 0.146$, which is consistent with both figure 2.6 and the general results presented in [USNA, 2007]. Therefore, one might trim table 4 to the following

Table 5: Viscous and wave-making resistance - simulation (trimmed)

Fr_L	u [m/s]	R_T [N]	Re_L	C_f	C_V	R_V [N]	R_w [N]
0.146	4.696	36512	4.698E+08	0.00168	0.00200	36512	0
0.150	4.824	39860	4.827E+08	0.00168	0.00199	38404	1456
0.200	6.432	87207	6.436E+08	0.00162	0.00192	65792	21415
0.230	7.397	131538	7.401E+08	0.00159	0.00189	85479	46059
0.250	8.040	168916	8.045E+08	0.00157	0.00187	99935	68982
0.300	9.648	288980	9.653E+08	0.00154	0.00183	140661	148319
0.350	11.257	474973	1.126E+09	0.00151	0.00179	187838	287135
0.400	12.865	732862	1.287E+09	0.00148	0.00176	241353	491509

From table 5, one can generate the following plot

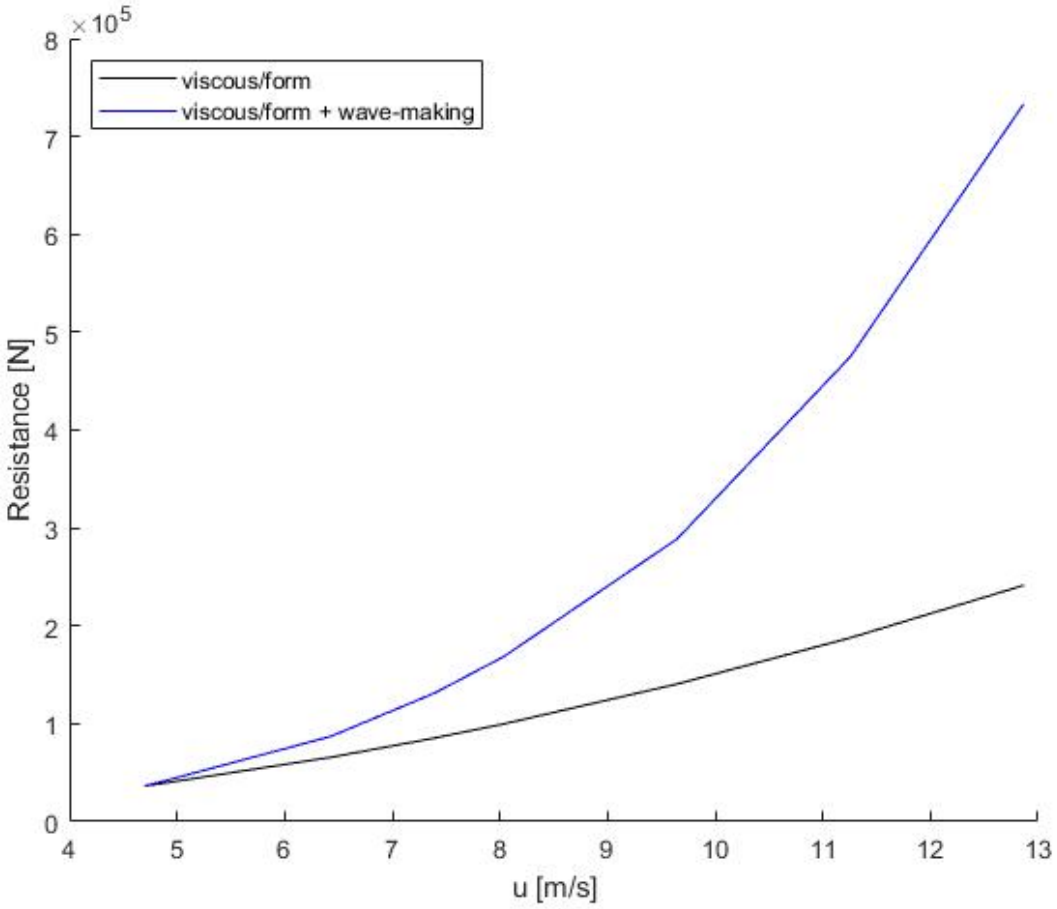

Figure 43: Simulation viscous and wave-making resistance

which is comparable to figure 2.6.

Theoretical Results

By way of equation 1d, and using the Wigley N43 block-coefficient of $C_b = 0.56073$, it was found that $(1 + K) = 1.1962$. This, together with the wave-making results in [bin Tarafder et al., 2007], allowed the following theoretical results to be generated

Table 6: Viscous and wave-making resistance - theoretical

Fr_L	u [m/s]	Re_L	R_V [N]	R_w [N]	R_T [N]
0.146	4.696	4.698E+08	36774	3889	40663
0.150	4.824	4.827E+08	38680	4333	43014
0.200	6.432	6.436E+08	66265	13696	79960
0.230	7.397	7.401E+08	86093	28882	114976
0.250	8.040	8.045E+08	100653	48149	148802
0.300	9.648	9.653E+08	141673	192594	334267
0.350	11.257	1.126E+09	189188	125828	315016
0.400	12.865	1.287E+09	243088	438258	681347

From table 6, one can generate the following plot

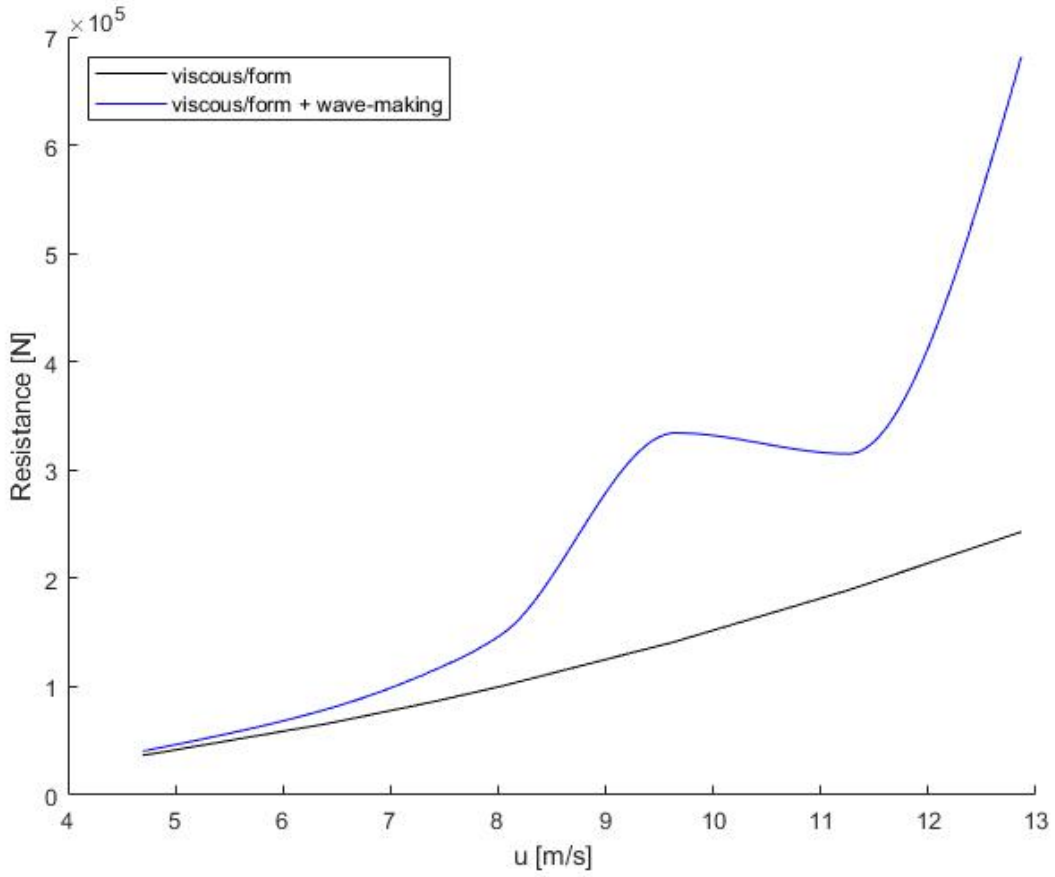

Figure 44: Theoretical viscous and wave-making resistance

which is comparable to figure 2.6.

Comparison

From the simulation and theoretical results for R_V, one can conclude that the theoretical results match the simulation results very well. This follows from the fact that there is only about a 5% error in applying equation 1d in this case, which results in errors in the theoretical R_V values of less than 1%. The simulation and theoretical results for R_w, however, show rather more discrepancy

Table 7: Wave-making resistance - comparison

Fr_L	u [m/s]	Re_L	R_w (sim.) [N]	R_w (theory) [N]	Error [N]	% Error
0.146	4.696	4.698E+08	0	3889	3889	-
0.150	4.824	4.827E+08	1456	4333	2878	198%
0.200	6.432	6.436E+08	21415	13696	-7720	-36%
0.230	7.397	7.401E+08	46059	28882	-17176	-37%
0.250	8.040	8.045E+08	68982	48149	-20833	-30%
0.300	9.648	9.653E+08	148319	192594	44275	30%
0.350	11.257	1.126E+09	287135	125828	-161307	-56%
0.400	12.865	1.287E+09	491509	438258	-53251	-11%

Table 7 suggests that, for $\mathrm{Fr}_L \geq 0.20$, the theoretical R_w values tend to under-predict the simulation values by about 35%. This then contributes to the following errors in R_T

Table 8: Total fluid resistance - comparison

Fr_L	u [m/s]	Re_L	R_T (sim.) [N]	R_T (theory) [N]	Error [N]	% Error
0.146	4.696	4.698E+08	36512	40663	4151	11%
0.150	4.824	4.827E+08	39860	43014	3154	8%
0.200	6.432	6.436E+08	87207	79960	-7247	-8%
0.230	7.397	7.401E+08	131538	114976	-16562	-13%
0.250	8.040	8.045E+08	168916	148802	-20115	-12%
0.300	9.648	9.653E+08	288980	334267	45287	16%
0.350	11.257	1.126E+09	474973	315016	-159957	-34%
0.400	12.865	1.287E+09	732862	681347	-51516	-7%

Table 8 then suggests that the theoretical R_T values tend to be within about +/- 15% of the simulation values. In addition, the theoretical R_T values tend to over-predict for $\mathrm{Fr}_L < 0.20$, and under-predict for $\mathrm{Fr}_L \geq 0.20$.

Conclusion

Given how rapidly one can generate, R_V, R_w, and R_T values using equations 1, it is concluded that a +/- 15% error in R_T is acceptable for the purpose of general vessel modelling. Therefore, for the case of car-deck ferry A, the proposed drag equations are valid.